

Characterisation of Polycrystal Deformation

by

Numerical Modelling and
Neutron Diffraction Measurements

Bjørn Clausen

Risø National Laboratory, Roskilde, Denmark
September 1997

Abstract The uniaxial deformation of polycrystals are modelled using three incremental rate-insensitive micro-mechanic models; the Taylor model, the Sachs model and Hutchinson's self-consistent model. The predictions of the two rigid plastic upper- and lower-bound models (Taylor and Sachs) are compared with the predictions of the elastic-plastic self-consistent model. As expected, the results of the self-consistent model is about half-way between the upper- and lower-bound models. The average number of active slip systems is about 3.6 compared to the five active slip systems in the Taylor model and the one active slip system in the Sachs model. The average m-factor is about 2.6 compared to the 3.06 in the Taylor model and the 2.23 in the Sachs model. The predicted rotation pattern of the self-consistent model is closest to the Taylor model, but the orientation distribution of the m-factor is closest to the Sachs model. The influence of the elastic anisotropy is investigated by comparing the self-consistent predictions for aluminium, copper and a hypothetical material (hybrid) with the elastic anisotropy of copper and the Young's modulus and work hardening behaviour of aluminium. It is concluded, that the effect of the elastic anisotropy is limited to the very early stages of plasticity ($\epsilon^P < \sim 0.1\%$), as the deformation pattern is almost identical for the three materials at higher strains.

The predictions of the three models are evaluated by neutron diffraction measurements of elastic lattice strains in grain sub-sets within the polycrystal. In the evaluation of the rigid plastic Taylor and Sachs models, the 'elastic' strain is determined as the calculated stress divided by the diffraction elastic constants (calculated as the Kröner elastic stiffnesses for the grain sub-sets). The comparison of calculated and measured lattice strains are made for three different materials; aluminium, copper and austenitic stainless steel. The predictions of the self-consistent model is more accurate and detailed than the predictions of the Taylor and Sachs models, though some discrepancies are noted for some reflections.

The self-consistent model is used to determine the most suitable reflection for technological applications of neutron diffraction, where focus is on the volume average stress state in engineering components. To be able to successfully convert the measured elastic lattice strains for a specific reflection into overall volume average stresses, there must be a linear relation between the lattice strain of the reflection and the overall stress. According to the model predictions the 311-reflection is the most suitable reflection, as it shows the smallest deviations from linearity and thereby also the smallest build-up of residual lattice strains. Below 5% deformation the deviations from linearity and the residual strains are below the normal strain resolution of a neutron diffraction measurement.

The model predictions have pinpointed, that the selection of the reflection is crucial for the validity of stresses calculated from the measured elastic lattice strains. The calculations are limited to uniaxial tension with an initially random texture, and in normal measurements with unknown stress state and texture, the complexity of the measurements increases. If the stress state is unknown, there will not be a unique solution to the macroscopic stress state, and the introduction of texture will inherently change the intergranular stresses and strains within the material, and therefore it might not be the 311-reflections, that is the most suitable reflection under all conditions.

ISBN 87-550-2304-5
ISSN 0106-2840

Information Service Department · Risø · 1997

Preface

The research described in this thesis was carried out while registered as a Ph.D. student at the Technical University of Denmark under supervision of associate professor Jes Christoffersen, Department of Solid Mechanics at the Technical University of Denmark, and Senior Scientist Dr. Torben Lorentzen, Materials Research Department at Risø National Laboratory. I wish to thank both my supervisors for many inspiring discussions and support throughout the project.

Most of the work was carried out at the Materials Research Department at Risø National Laboratory and I acknowledge Dr.techn. Torben Leffers for his assistance and fruitful discussions. Thanks are also due to Dr. Mark A. M. Bourke and Dr. Mark R. Daymond at Los Alamos National Laboratory for their assistance with the *time-of-flight* measurements at the Manuel Lujan Neutron Scattering Center.

This thesis is submitted to the Technical University of Denmark in partial fulfillment of the requirements for obtaining the Ph.D. degree.

Risø, September 1997

Bjørn Clausen

Contents

Preface *iii*

1 **Introduction** *1*

2 **Modelling** *5*

2.1 Taylor Model *5*

2.1.1 Grain Rotations *7*

2.1.2 Model Predictions *9*

2.2 Sachs Model *11*

2.2.1 Model Predictions *12*

2.3 Self-consistent Model *14*

2.3.1 Model Predictions *17*

2.3.1.1 Elastic Moduli *17*

2.3.1.2 Number of Active Slip Systems *18*

2.3.1.3 The m-factor *22*

2.3.1.4 Lattice Rotations *22*

2.4 Summary *26*

3 **Implications for Diffraction Measurements** *27*

3.1 Calculations *28*

3.2 Results *28*

3.2.1 Diffraction Elastic Constants *29*

3.2.2 Elastic Lattice Strains *29*

3.2.3 Elastic Lattice Strain Variations *31*

3.2.4 Deviation from Linearity *34*

3.2.5 Normalised Stresses *36*

3.2.6 Residual Strain *36*

3.3 Discussion *38*

4 **Neutron Diffraction** *41*

4.1 Lattice Strain Determination *41*

4.1.1 Fixed Wavelength Method *41*

4.1.1.1 Measurements *42*

4.1.2 *Time-of-flight* Method *43*

4.1.2.1 Measurements *44*

4.2 Texture Measurement *48*

5 **Model Evaluation** *51*

5.1 Taylor and Sachs Models *51*

5.2 Self-consistent Model *53*

5.2.1 Aluminium *54*

5.2.2 Stainless Steel *57*

5.2.3 Copper *59*

5.3 Summary *61*



6	Conclusion	<i>63</i>
6.1	Modelling	<i>63</i>
6.1.1	Taylor and Sachs Models	<i>63</i>
6.1.2	Self-consistent Model	<i>64</i>
6.2	Implications for Diffraction Measurements	<i>64</i>
6.3	Model Evaluation	<i>65</i>
6.4	General Conclusions	<i>67</i>

References	<i>69</i>
-------------------	-----------

Appendix

A	Appropriate Gauge Volume	<i>73</i>
A.1	Diffraction Grains Within the Gauge Volume	<i>77</i>
A.2	Standard Deviation of a Strain Measurement	<i>78</i>
B	Calculated Residual Strains	<i>79</i>

1 Introduction

When designing components engineers optimize the structure of the components for strength and weight. An optimized component can reduce both economical and environmental costs especially if it is utilised in transportation applications, where the fuel efficiency is highly dependent of the total mass of the construction.

To be able to optimize the component, the engineer must know the internal stress and strain state in the component. From the stress state it is possible to determine where in the construction, the material is loaded close to the design limit and where the material load is relatively low. Then the component can be redesigned reducing cross sections with relatively low internal stresses and increasing cross section or using other forms of local reinforcement in areas of relatively high internal stress.

Using finite element model calculations (Zienkiewicz and Taylor 1988) it is possible to determine the stress and strain concentrations under load within a component, with the assumption, that the material is stress-free, after production. However, if the material have been plastically deformed during production, residual stresses and strains have been built up in the component. To get the correct answer, these residual stresses and strains must be incorporated in the calculations. Residual stresses are self-equilibrating stresses existing within materials without external loading. The residual stresses are produced by loading a elastically and/or plastically anisotropic material to a permanent deformation. Even if the overall plastic deformation is homogeneous, there will be induced misfit strains in the material, as the grains do not undergo the same plastic deformation due to the crystallographic orientation. Residual stress are also induced in the material, if it is subjected to inhomogeneous overall plastic deformation.

The residual stresses can be either beneficial or detrimental for a component depending on the combination of the sign of the residual stress and the type of loading. As an example the introduction of compressive residual stresses by shot peening can increase the fracture load for a component loaded in tension.

If the designer wants to use the full capability of a material and still make a safe component, the residual stresses in the component must be considered. The residual stresses can be determined non-destructively using diffraction techniques. In these techniques, the Bragg scattering of X-rays and neutrons in the crystal structure of materials is utilised to measure the lattice spacing in grains within the material (Noyan and Cohen 1987). The penetration depth of X-rays is in the order of μm in normal structure materials limiting the measurements to the surface of the materials, but the penetration depth of neutrons is in the order of cm in the

same materials making it possible to measure a bulk average of the elastic strains within sub-sets of grains in a component.

In a diffraction measurement one elastic lattice strain component in one direction is determined for a specific grain sub-set. The grains, that participate in the measurement, are the ones, that have a specific lattice plane normal in a given direction. This selective nature of the diffraction techniques introduces difficulties in the interpretation of the measurements. In technological applications the overall stress state in the sample is of interest, and the conversion of the specific elastic lattice strain components within the grain sub-sets to an overall stress state is not trivial.

The simplest way to estimate the stress state is to multiply the determined elastic lattice strain component with the Young's modulus for the used reflection (grain sub-set). The moduli for the specific reflections are known as the diffraction elastic constants. By using this simple calculation, it is assumed, that the stress state in the sample is one-dimensional. If elastic strain components are determined in multiple directions, it is possible to use the generalised Hooke's law in the calculations of the stress state, and thereby compensating for a three-dimensional stress state. But still this assumes isotropic material, and furthermore, the lattice strains, that are determined in such measurements of a full strain tensor, are not originating from the same set of grains, and therefore intergranular strains will influence the results.

Another way to determine the overall stress state is available by numerical modelling of polycrystal deformation. Using micro-mechanical polycrystal deformation models, which are based on the deformation of the constituents (grains) of the polycrystal, it is possible to predict the elastic and plastic deformation of a polycrystal and thereby of specific grain sub-sets within the polycrystal. The polycrystal deformation models can be used to determine the relation between the elastic strain in given grain sub-sets and the overall stress, and the intergranular stresses and strains between the grain sub-sets, as functions of the deformation. The use of the model predictions of residual strains in technological applications of neutron diffraction is illustrated in (Lorentzen *et al.* 1996), where the predicted intergranular residual strains in a plastically deformed copper sample is used to correlate neutron diffraction measurements and FEM calculations.

In the last seventy years several theories predicting the flow-stress and texture development in polycrystals during plastic deformation have been proposed. The models utilise different simplifications to describe the coupling between the grains in the polycrystal. In the upper-bound models, *e.g.* Taylor and Bishop-Hill (Taylor 1938, Bishop and Hill 1951a, Bishop and Hill 1951b, Bishop 1953), all the grains are subjected to the same strain and in the lower-bound models, *e.g.* Sachs and Leffers (Sachs 1928, Leffers 1995), the grains are subjected to the same stress. The coupling between the grains is very stiff in these rather simple models, and they are the upper- and lower-bound polycrystal plasticity models as the Voigt and Reuss (Voigt 1928, Reuss 1929) models are for the elastic stiffness of a polycrystal.

Based on Eshelby's inclusion theory (Eshelby 1957) the self-consistent scheme was introduced in the Kröner and Budiansky-Wu models (Kröner 1961, Budiansky and Wu 1962). In the self-consistent models, the grains are regarded as inclusions in an infinite homogeneous matrix. Eshelby has shown, that the stress and strain state is uniform within the inclusion if, it has an ellipsoidal shape. The properties of the matrix are determined as the overall average properties of the single crystal agglomerate. In the Kröner and Budiansky-Wu models the coupling between a grain and the polycrystal (matrix) is determined by the elastic stiffness of the matrix and the constituents, which is a relatively stiff coupling in the plastic regime. In the self-consistent models the interaction between the grains and the

pseudo polycrystal is incorporated in the model, but the direct grain-to-grain interaction is not taken into account. The elastic anisotropy of the model material is inherently included in the self-consistent modelling schemes as opposed to the Sachs and Taylor models, which do not include any material characteristics.

The Kröner and Budiansky-Wu self-consistent schemes uses a fully elastic coupling between the grains and the matrix, and therefore it predicts a very low deformation heterogeneity in the polycrystal. The self-consistent modelling scheme of Hill/Hutchinson (Hill 1965a, Hill 1965b, Hill 1966, Hutchinson 1970) introduces the elastic-plastic coupling between the grains and the matrix, which predicts a more realistic deformation heterogeneity in the polycrystal. In these models the interaction between the grain and the matrix is determined by the instantaneous grain- and matrix moduli.

In the present work, the Taylor model, the Sachs model and mainly the self-consistent model of Hutchinson are investigated. The focus of the investigations are on the different basic assumptions in the models and the implications on the deformation properties in the constituents. Furthermore the development of strains and stresses within grain sub-sets are of interest as a means of evaluating the model predictions by neutron diffraction measurements.

The simple Taylor and Sachs models are rigid plastic models, which makes the comparison with the measured elastic lattice strain components rather artificial, as the calculated stress in the grain sub-sets must be converted into 'elastic' strains by division by the diffraction elastic constants. The diffraction elastic constants are determined as the Kröner elastic stiffnesses of the grain sub-sets (Kröner 1958). In the more sophisticated elastic-plastic self-consistent model, the specific elastic properties of a given material is taken into account, and it is straight forward to determine elastic strain components for specific grain sub-sets.

The predictions of the models are correlated with the results of neutron diffraction measurements. In the diffraction measurements elastic lattice strains are measured in specific grain sub-sets determined by Bragg's law as described in section 4. This correlation of calculated and measured elastic lattice strain serve as an evaluation of the modelling schemes on a grain size scale. This form of evaluation is more specific than the normal evaluation of polycrystal deformation model, where the predicted textures for large deformations are correlated with measured textures. Neutron diffraction measurements of residual and *in-situ* lattice strains in aluminium, copper and austenitic stainless steel samples loaded in uniaxial tension are used in the investigations.

2 Modelling

The nomenclature used in the present work is mainly the one used in (Hutchinson 1970). Boldface lower case letters are used as symbols for second-order Cartesian tensors and fourth-order Cartesian tensors are represented by boldface upper case letters. The contracted product of two second-order tensors, $a_{ij}b_{ij}$, is written as \mathbf{ab} , and the inner product of two fourth-order tensors, $A_{ijmn}B_{mnlk}$, is written as \mathbf{AB} .

The tensors are represented in an orthonormal dyadic base as described in (Pedersen 1995): The symmetric second-order tensors are represented by an vector, where the original off-diagonal components are multiplied with $\sqrt{2}$, as shown in equation 2.1.

$$\mathbf{a} = [a_{11} \quad a_{22} \quad a_{33} \quad \sqrt{2}a_{23} \quad \sqrt{2}a_{31} \quad \sqrt{2}a_{12}] \quad (2.1)$$

The symmetric fourth-order tensors are represented by a matrix, where the components in the upper right quadrant and in the lower left quadrant are multiplied with $\sqrt{2}$, and the components in the lower right quadrant is multiplied with 2, as shown in equation 2.2.

$$\mathbf{A} = \begin{bmatrix} A_{1111} & A_{1122} & A_{1133} & \sqrt{2}A_{1123} & \sqrt{2}A_{1131} & \sqrt{2}A_{1112} \\ A_{2211} & A_{2222} & A_{2233} & \sqrt{2}A_{2223} & \sqrt{2}A_{2231} & \sqrt{2}A_{2212} \\ A_{3311} & A_{3322} & A_{3333} & \sqrt{2}A_{3323} & \sqrt{2}A_{3331} & \sqrt{2}A_{3312} \\ \sqrt{2}A_{2311} & \sqrt{2}A_{2322} & \sqrt{2}A_{2333} & 2A_{2323} & 2A_{2331} & 2A_{2312} \\ \sqrt{2}A_{3111} & \sqrt{2}A_{3122} & \sqrt{2}A_{3133} & 2A_{3123} & 2A_{3131} & 2A_{3112} \\ \sqrt{2}A_{1211} & \sqrt{2}A_{1222} & \sqrt{2}A_{1233} & 2A_{1223} & 2A_{1231} & 2A_{1212} \end{bmatrix} \quad (2.2)$$

This definition implies that the unity tensor satisfying $\mathbf{I} = \mathbf{A}^{-1}\mathbf{A}$, defined as $I_{ijkl} = 1/2(\delta_{ik}\delta_{jl} + \delta_{il}\delta_{jk})$, renders a matrix with one's in all the diagonal elements.

2.1 Taylor Model

Taylor (Taylor 1938) proposed a model for calculating the uniaxial stress-strain relation for a polycrystal in which, the polycrystal is regarded as an agglomerate of randomly oriented *fcc* single crystals, which are assumed to be rigid-plastic.

In a uniaxial tension test of a single crystal, the lateral dimensions can change relatively freely, and the glide shear produced by slip on a single slip system is sufficient to accommodate the tensile deformation. The active slip system is the

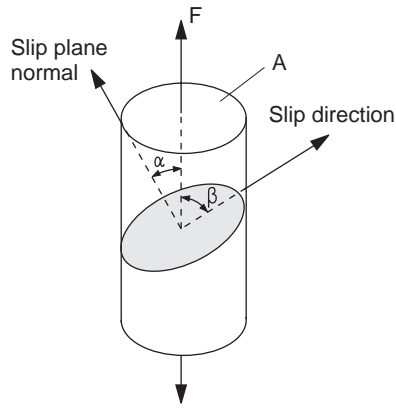


Figure 2.1. The geometry of slip in crystalline materials.

one with the highest resolved shear stress according to the Schmid law (Hull and Bacon 1984), see figure 2.1.

The tensile stress is $\sigma = F/A$, the force perpendicular to the slip plane is $F \cos \alpha$, and the area of the slip plane is $A/\cos \beta$. The resolved shear stress is found as $\tau = \sigma \cos \alpha \cos \beta$, where the quantity $\cos \alpha \cos \beta$ is known as the Schmid factor. The same criteria for the active slip system can be expressed by the m-factor (or Taylor factor: $m = \sigma/\tau = \gamma/\epsilon$). This means, that the active slip system is the one with the minimum m-factor.

If the crystal is embedded in a polycrystalline aggregate, it can not change its shape freely due to constraints from the surrounding polycrystal. In this case, slip from five independent slip systems is generally required to accommodate the five independent strain components for plastic deformation (Von Mises 1928). Based on the principle of virtual work, Taylor hypothesized that, among all combination of five slip systems which are capable of accommodating the imposed strain, the active combination is the one with the minimum accumulated slip. In analogy to the single slip case, this is equivalent to the combination of slip with the minimum m-factor value, where

$$m = \frac{\sum_i \dot{\gamma}^i}{\dot{\epsilon}_{11}^p} \quad (2.3)$$

and i identifies the active slip systems. Based on visual observations of grains in a drawn wire, Taylor assumed, that the plastic strain is homogeneous and independent of the orientation of the grain, that is the strain in any grain equals the average strain. The same assumption is made for the strain rate in the grains; $\dot{\epsilon}_{ij}^p = \dot{\epsilon}_{ij}^p$. This assumption of uniform strain in all the grains implies stress discontinuities at the grain boundaries. However, the Taylor model have been used with success for prediction of textures for large deformations.

In a *fcc* single crystal all slip occurs on one of the four close packed $\{111\}$ planes in one of the three $\langle 110 \rangle$ directions. In each grain these twelve slip systems are specified relative to an arbitrary set of cartesian axes by the unit vector \mathbf{n}^i normal to the slip plane, and the unit vector \mathbf{m}^i in the slip direction ($i = 1, 2, \dots, 12$). Furthermore Taylor assumed a uniform stress state σ_{ij} and thereby stress rate $\dot{\sigma}_{ij}$ within each grain. The resolved shear stress rate on the i th slip system is (the Schmid law)

$$\dot{\tau}^i = \dot{\sigma}_{kl} n_k^i m_l^i = \dot{\sigma}_{kl} \mu_{kl}^i \quad (2.4)$$

where

$$\mu_{kl}^i = \frac{1}{2} (m_k^i n_l^i + m_l^i n_k^i) \quad (2.5)$$

The plastic strain rate in the grain due to the slip that have occurred along all the slip systems, is

$$\dot{\varepsilon}_{kl}^P = \sum_i \dot{\gamma}^i \mu_{kl}^i \quad (2.6)$$

where the summation is taken over all active slip systems. Choosing the sign of \mathbf{m}^i so that $\dot{\gamma}^i$ is never negative the number of possible slip systems increases to 24. Finding the minimum virtual work for a given strain rate leads to the minimization of the linear cost function, $\dot{W} = \dot{\sigma}\dot{\varepsilon} = \sum_i \dot{\tau}^i \dot{\gamma}^i$, with the criterion that all variables, $\dot{\gamma}^i$, are non-negative.

This type of problem is easily solved with linear programming, *e.g.* the simplex method (Arora 1989). Depending on the orientation of the grain, the number of possible active slip systems with minimum work done reduces to six or eight (Chin and Mammel 1967). Of all the combinations of choosing five slip systems out of six or eight, there are only few, but more than one, solutions with the same minimum m-factor. This leads to an ambiguity in choosing the active slip systems. Many criteria have been suggested for the selection among the solutions with minimum m-factor, all with a heuristic basis.

Taylor assumed, that the critical resolved shear stress rate is related to the slip rates by

$$\dot{\tau}^i = \sum_j h_{ij} \dot{\gamma}^j \quad (2.7)$$

where all components of the hardening matrix, h_{ij} , are identical (h). If Taylor hardening (isotropic hardening) is used, the critical resolved shear stress rate is the same for all slip systems, and the ambiguity will arise for every strain increment. If Hill's more general hardening law, where it is assumed that the self-hardening and latent-hardening have different properties ($h_{ii} = h_1$ and other $h_{ij} = h_2$), is used, the ambiguity only arises in the first iteration, where the initial critical resolved shear stress, τ_0 , is assumed equal on all the slip systems.

In the present Taylor model, the active combination of slip systems is intuitively chosen to the one, that has a maximum amount of slip on one slip system and then the four other slip systems have a relative small amount of slip in order to accommodate the prescribed deformation. In (Leffers *et al.* 1988) a series of selection criteria for the active set of slip systems are discussed.

The stress rate in the grains can be determined using equation 2.4 for the active slip systems

$$\dot{\sigma}_{kl} \mu_{kl}^i = \dot{\tau}^i \quad (2.8)$$

Splitting the stress rate tensor in its deviatoric and spherical parts, it is found that

$$\dot{\sigma}_{ij} = \dot{s}_{ij} + \frac{1}{3} \delta_{ij} \dot{\sigma}_{kk} \quad (2.9)$$

where δ is Kronecker's delta, and since $\mu_{kk}^i \equiv 0$ we get for the five active slip systems

$$\dot{s}_{kl} \mu_{kl}^i = \dot{\tau}^i \quad (2.10)$$

This provides five equations to find the five deviatoric stress rate components from the hardening parameters. However, in terms of absolute stress rate values the possible hydrostatic stress rate component $\dot{\sigma}_{kk}$ is still undetermined.

2.1.1 Grain Rotations

Once the slip rates have been identified, it is possible to determine the lattice rotation of the grains, and hence the model provides a means of following the

generation of texture by plastic deformation. The lattice rotation increment, $\dot{\Omega}^L$, is expressed in terms of the specific $\dot{\gamma}^i$, \mathbf{n}^i and \mathbf{m}^i values by

$$\dot{\Omega}_{kl}^L = - \sum_i \left\{ \frac{1}{2} (m_k^i n_l^i - m_l^i n_k^i) \dot{\gamma}^i \right\} \quad (2.11)$$

The Euler angles, φ_1 , Φ and φ_2 (Bunge 1982), are the mostly used orientation parameters for quantitative texture analysis but in the following calculations of the lattice rotations in the grains the definition of the Euler angles with two rotations around the same axis will lead to, that some of the following equations will be under determined. Instead it is chosen to use the Cardanic angles for calculation of the lattice rotation increments, but still use the Euler angles to describe the grain orientation for all external parameters.

The Cardanic angles θ_1 , θ_2 and θ_3 describe a rotation around the three Cartesian axes respectively and do not have the singularities in the orientation space as the Euler angles. The relations between the Euler angles and the Cardanic angles are as follows

$$\begin{aligned} \varphi_1 &= \theta_3 - \text{atan} \frac{\tan \varphi_2}{\cos \Phi} & \theta_1 &= \text{atan} (\cos \varphi_2 \tan \Phi) \\ \Phi &= \text{atan} \frac{\tan \theta_1}{\cos \varphi_2} & \theta_2 &= -\text{atan} (\tan \varphi_2 \sin \varphi_1) \\ \varphi_2 &= -\text{atan} \frac{\tan \theta_2}{\sin \theta_1} & \theta_3 &= \varphi_1 + \text{atan} (\tan \varphi_2 \cos \Phi) \end{aligned} \quad (2.12)$$

Using the Cardanic angles the total rotation of the grain coordinate system related to the specimen coordinate system is

$$\mathbf{Q} = \mathbf{Q}_1 \mathbf{Q}_2 \mathbf{Q}_3 \quad (2.13)$$

where

$$\begin{aligned} \mathbf{Q}_1 &= \begin{bmatrix} 1 & 0 & 0 \\ 0 & \cos \theta_1 & \sin \theta_1 \\ 0 & -\sin \theta_1 & \cos \theta_1 \end{bmatrix}, \quad \mathbf{Q}_2 = \begin{bmatrix} \cos \theta_2 & 0 & -\sin \theta_2 \\ 0 & 1 & 0 \\ \sin \theta_2 & 0 & \cos \theta_2 \end{bmatrix} \text{ and} \\ \mathbf{Q}_3 &= \begin{bmatrix} \cos \theta_3 & \sin \theta_3 & 0 \\ -\sin \theta_3 & \cos \theta_3 & 0 \\ 0 & 0 & 1 \end{bmatrix} \end{aligned} \quad (2.14)$$

are a rotation around the 1st axis, around the rotated 2nd axis and around the rotated 3rd axis respectively. Using only first order elements, a small increment in the rotation is given by

$$\dot{\mathbf{Q}} = \dot{\mathbf{Q}}_1 \mathbf{Q}_2 \mathbf{Q}_3 + \mathbf{Q}_1 \dot{\mathbf{Q}}_2 \mathbf{Q}_3 + \mathbf{Q}_1 \mathbf{Q}_2 \dot{\mathbf{Q}}_3 \quad (2.15)$$

where

$$\begin{aligned} \dot{\mathbf{Q}}_1 &= \begin{bmatrix} 0 & 0 & 0 \\ 0 & -\sin \theta_1 & \cos \theta_1 \\ 0 & -\cos \theta_1 & -\sin \theta_1 \end{bmatrix} \dot{\theta}_1, \quad \dot{\mathbf{Q}}_2 = \begin{bmatrix} -\sin \theta_2 & 0 & -\cos \theta_2 \\ 0 & 0 & 0 \\ \cos \theta_2 & 0 & -\sin \theta_2 \end{bmatrix} \dot{\theta}_2 \text{ and} \\ \dot{\mathbf{Q}}_3 &= \begin{bmatrix} -\sin \theta_3 & \cos \theta_3 & 0 \\ -\cos \theta_3 & -\sin \theta_3 & 0 \\ 0 & 0 & 0 \end{bmatrix} \dot{\theta}_3 \end{aligned} \quad (2.16)$$

To simplify the calculations we define the three rotation matrices

$$\begin{aligned} \dot{\Omega}_1 &= \dot{\mathbf{Q}}_1 \mathbf{Q}_1^T = \begin{bmatrix} 0 & 0 & 0 \\ 0 & 0 & \dot{\theta}_1 \\ 0 & -\dot{\theta}_1 & 0 \end{bmatrix}, \quad \dot{\Omega}_2 = \dot{\mathbf{Q}}_2 \mathbf{Q}_2^T = \begin{bmatrix} 0 & 0 & -\dot{\theta}_2 \\ 0 & 0 & 0 \\ \dot{\theta}_2 & 0 & 0 \end{bmatrix} \text{ and} \\ \dot{\Omega}_3 &= \dot{\mathbf{Q}}_3 \mathbf{Q}_3^T = \begin{bmatrix} 0 & \dot{\theta}_3 & 0 \\ -\dot{\theta}_3 & 0 & 0 \\ 0 & 0 & 0 \end{bmatrix} \end{aligned} \quad (2.17)$$

Now we can rewrite 2.15 into

$$\dot{Q} = Q\dot{\Omega}_1 + Q_1\dot{\Omega}_2Q_1^TQ + Q_1Q_2\dot{\Omega}_3Q_1^TQ_2^TQ \quad (2.18)$$

The lattice rotation increment in the grain $\dot{\Omega}^L$ is found as

$$\dot{\Omega}^L = \dot{Q}Q^T = \dot{\Omega}_1 + Q_1\dot{\Omega}_2Q_1^T + Q_1Q_2\dot{\Omega}_3Q_1^TQ_2^T \quad (2.19)$$

and denoting the three rotation matrices $\dot{\Omega}_1$, $\dot{\Omega}_2$ and $\dot{\Omega}_3$ by their rotation vectors $\dot{\omega}_1$, $\dot{\omega}_2$ and $\dot{\omega}_3$

$$\dot{\omega}_1 = \begin{bmatrix} -\dot{\theta}_1 \\ 0 \\ 0 \end{bmatrix}, \quad \dot{\omega}_2 = \begin{bmatrix} 0 \\ -\dot{\theta}_2 \\ 0 \end{bmatrix} \quad \text{and} \quad \dot{\omega}_3 = \begin{bmatrix} 0 \\ 0 \\ -\dot{\theta}_3 \end{bmatrix} \quad (2.20)$$

equation 2.19 simplifies to

$$\dot{\omega}^L = \dot{\omega}_1 + Q_1\dot{\omega}_2 + Q_1Q_2\dot{\omega}_3 \quad (2.21)$$

or written out in components

$$\dot{\omega}^L = \begin{bmatrix} \dot{\omega}_1^L \\ \dot{\omega}_2^L \\ \dot{\omega}_3^L \end{bmatrix} = \begin{bmatrix} -\dot{\theta}_1 + \sin \theta_2 \dot{\theta}_3 \\ -\cos \theta_1 \dot{\theta}_2 - \sin \theta_1 \cos \theta_2 \dot{\theta}_3 \\ \sin \theta_1 \dot{\theta}_2 - \cos \theta_1 \cos \theta_2 \dot{\theta}_3 \end{bmatrix} \quad (2.22)$$

where $\dot{\omega}^L$ is the lattice rotation increment vector. This renders three equations for the calculation of the angle increments

$$\begin{aligned} \dot{\theta}_1 &= -\dot{\omega}_1^L - \tan \theta_2 \sin \theta_1 \dot{\omega}_2^L - \tan \theta_2 \cos \theta_1 \dot{\omega}_3^L \\ \dot{\theta}_2 &= -\cos \theta_1 \dot{\omega}_2^L + \sin \theta_1 \dot{\omega}_3^L \\ \dot{\theta}_3 &= -\frac{\sin \theta_1}{\cos \theta_2} \dot{\omega}_2^L - \frac{\cos \theta_1}{\cos \theta_2} \dot{\omega}_3^L \end{aligned} \quad (2.23)$$

and it is now possible to determine the rotation increment of the grain for a given strain rate by solving the equations 2.11 and 2.23.

2.1.2 Model Predictions

The present Taylor model is implemented in an ANSI C program, that can determine the deformation of a agglomerate of rigid plastic single crystals. The flow chart for `taylor.c` is shown in figure 2.2.

The initialization consists of a number of parameters defining values such as; the number of grains, the strain rate, the number of iterations, the initial critical resolved shear stress, the hardening law (Taylor or Hill) and the hardening coefficients. For every iteration, the stresses, strains and m-factors are calculated, and the output of the program is the average values of σ , ε and the m-factor for the polycrystal and for selected grain sub-sets. The orientations of all the grains are updated for each iteration, and the orientation of selected grains are determined as a function of the deformation.

In the present calculations the polycrystal is represented by a set of 5000 single crystals with initially random orientations, represented by their Euler angles (φ_1 , Φ and φ_2). As shown in Table 2.1, the average m-factor value is calculated for four grain sub-sets: grains with a $\langle 100 \rangle$, $\langle 110 \rangle$ or $\langle 111 \rangle$ lattice plane normal within 10° of the tensile direction, and grains with a $\langle 123 \rangle$ lattice plane normal within 5° of the tension direction. Additionally the m-factor is determined for three single orientations: $\langle 100 \rangle$, $\langle 110 \rangle$ and $\langle 111 \rangle$.

The results of the calculations with the present Taylor model are in agreement with previous reported calculations (Chin and Mammel 1967) as seen in table 2.1.

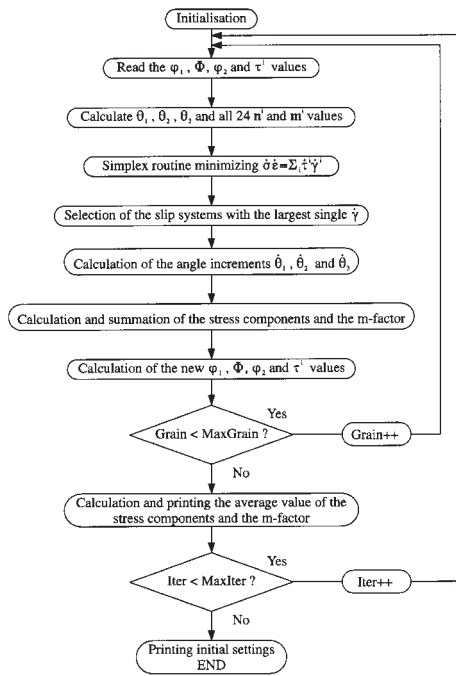


Figure 2.2. Flow chart for `taylor.c`

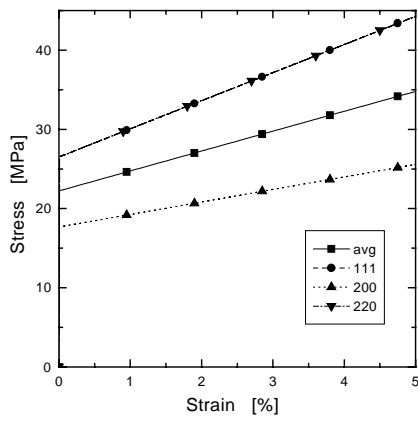
Direction	Present model	(Chin and Mammel 1967)
[100]	2.449	2.449
[100], 0 to 10°	2.392	2.394
[110]	3.674	3.674
[110], 0 to 10°	3.594	3.591
[111]	3.674	3.674
[111], 0 to 10°	3.591	3.591
[123], 0 to 5°	3.144	3.199
Average	3.063	3.067

Table 2.1. Calculated m -factors for specific orientations and as average.

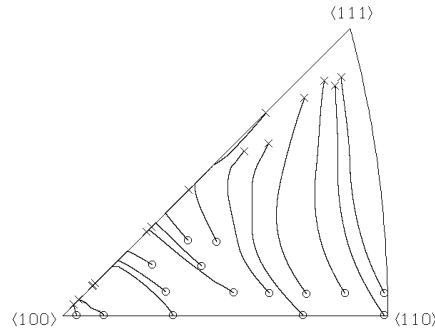
The minor differences in the results can be caused by different ways of representing the random orientations.

The predictions of the used polycrystal deformation models are compared with neutron diffraction measurements described in section 5.1. In the diffraction measurements the elastic lattice strain within specific grain sub-sets are determined as a function of the applied load in a tension test. The calculated stresses must be converted to 'elastic' strain components before a comparison with the measured elastic lattice strains is possible. The average stress within a grain sub-set, representing the reflections in the measurements, are determined as well as the overall stress-strain response of the model. The following parameters are used in the calculations: $\dot{\epsilon}_{11}^P = 0.01\%$, $\tau_0 = 10.9\text{MPa}$ and $h = 40\text{MPa}$. The result are presented in figure 2.3(a).

The grains within the sub-sets all have a specific lattice plane normal parallel to the tension axis as in a diffraction measurement. The grain sub-sets (reflections) are denoted by the hkl plane normal, that is parallel to the tensile axis; $\langle 111 \rangle$, $\langle 200 \rangle$ and $\langle 220 \rangle$. The latter two are used instead of $\langle 100 \rangle$ and $\langle 110 \rangle$, as the extinction rules for diffraction in the *fcc* lattice only allows diffraction for planes where hkl



(a) The stress strain response of the polycrystal and of the three grain sub-sets.



(b) The lattice rotations in 15 specific grains for uniaxial tension to 70% deformation.

Figure 2.3. Stress-strain response and lattice rotations in the Taylor model.

are all odd or all even (Barrett and Massalski 1980).

The Taylor model does not include any material parameters, such as the elastic anisotropy, in the calculations. Thereby the stress-strain response is practically identical for the 111- and 220-reflections, see figure 2.3(a), as the average m-factor values are practically identical for these two reflections. Likewise the m-factor is identical for the $\langle 111 \rangle$ and $\langle 220 \rangle$ directions, see table 2.1.

The lattice rotations of 15 specific grains have been calculated for uniaxial tension to a total strain of 70%. The results for the present calculation are shown in figure 2.3(b) in an inverse pole plot; the starting orientations are indicated by circles, the end orientations by crosses. The lattice rotations calculated with the present Taylor model is very similar to the lattice rotations presented in (Leffers 1988) for different polycrystal deformation models.

The model calculations show, that the present implementation of the Taylor model predicts the same m-factors and lattice rotations as reported for other implementations in the literature (Chin and Mammel 1967, Leffers 1988). With relation to the neutron diffraction measurements the rigid plastic Taylor model is rather simple as no material parameters, such as the elastic anisotropy, are included in the model. The fact, that the model is rigid plastic, makes the comparison with the determined elastic lattice strains complicated, as the calculated stresses must be converted to elastic lattice strain components before they are comparable with the experimental results (as shown in section 5).

The predictions of the present Taylor model will be compared with the predictions of the Sachs model and the self-consistent model in section 2.3.

2.2 Sachs Model

In the Sachs model (Sachs 1928) the polycrystal is regarded as an agglomerate of rigid plastic single crystals as in the Taylor model. But instead of prescribing the same strain in all the constituents, Sachs proposed to let all the grains be prescribed the same stress, which leads to the so-called *extreme* lower-bound for the polycrystal models.

The present Sachs model is an incremental rigid plastic model, where only the stress *state* is assumed to be identical in all the grains, which is the more realistic

lower-bound for the polycrystal models (this model is, in fact, a multi-slip model). In uniaxial tension the only non-zero stress component is σ_{11} . The resolved shear stress rate on the i th slip system, $\dot{\tau}^i$, and the plastic strain rate, $\dot{\epsilon}_c^P$, are determined as described in section 2.1

$$\dot{\tau}^i = \dot{\sigma} \mu^i \quad \text{and} \quad \dot{\epsilon}_c^P = \sum_i \dot{\gamma}^i \mu^i \quad (2.24)$$

The active slip system in the Sachs model is the one with the highest resolved shear stress rate. If the grain is oriented along a symmetry line, there will be two slip systems with identical resolved shear stress rate, and if the grain is oriented in a corner of the basic crystallographic triangle, there will be up to four, six or eight slip systems with the same resolved shear stress rate. In such cases, all the slip systems with the highest resolved shear stress rate is active, and it is assumed, that the amount of slip is identical on all the active slip systems.

All the grains in the agglomerate are prescribed the same strain increment in the tension direction, $\dot{\epsilon}_{11}^P$, and thereby the slip on the active slip systems in the grains can be determined from

$$\dot{\epsilon}_{11}^P = \sum_i \dot{\gamma}^i \mu_{11}^i \quad (2.25)$$

The resolved shear stress rate is assumed to be related to the shear rates by the hardening matrix, h^{ij} , using the linear isotropic hardening law described in section 2.1. Knowing that σ_{11} is the only non-zero stress component, the stress rate in the grain can be determined using the Schmid law (equation 2.24)

$$\dot{\sigma}_{11} \mu_{11}^i = \dot{\tau}^i = \sum_j h^{ij} \dot{\gamma}^j \quad (2.26)$$

As only the strain rate component in the tensile direction is the same in all the grains, the Sachs model introduces both stress and strain discontinuities at the grain boundaries. The lattice rotations in the grains are calculated from the slip in the grains as described in section 2.1.1.

2.2.1 Model Predictions

The present Sachs model has been implemented in an ANSI C program, that can calculate the overall stress-strain response of the model, and the relation between the average stress in specific grain sub-sets, representing reflections in a neutron diffraction measurement, and the overall strain. The flow chart for `sachs.c` is shown in figure 2.4.

The results of a calculation, using the same parameters as in the Taylor model calculations in section 2.1, are shown in figure 2.5(a). The m-factor ($\sum_i \dot{\gamma}^i / \dot{\epsilon}_{11}^P$) is also determined as an overall average and as average within the grain sub-sets representing the 111-, 200- and 220-reflections. The results are listed in table 2.2 together with the corresponding results for the Taylor model presented in section 2.1.

As the Taylor model, the Sachs model does not include any material parameters in the calculations, and thereby the stress-strain response is identical for the 200- and 220-reflections as seen in figure 2.5(a). The m-factor calculations also show the same value for these two orientations, and the average m-factor is very similar for the 200- and 220-reflections, see table 2.2. Notice that it is the 111- and 220-reflections, that are identical in the Taylor model.

The lattice rotations of the same 15 grains as used in the Taylor model calculations have been calculated for uniaxial tension to a total strain of 70%. As seen in figure 2.5(b), the grains oriented along symmetry lines rotate parallel to the symmetry lines, as they have two or more active slip systems, and the grains in

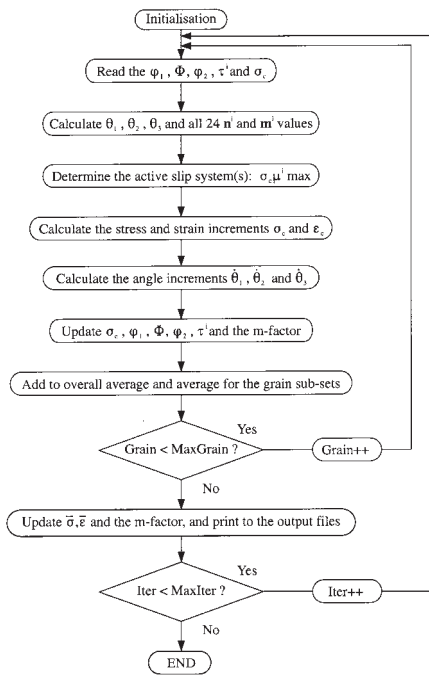
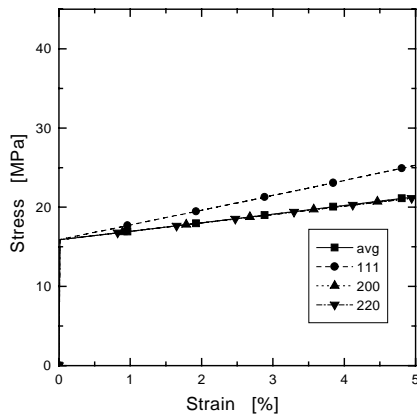
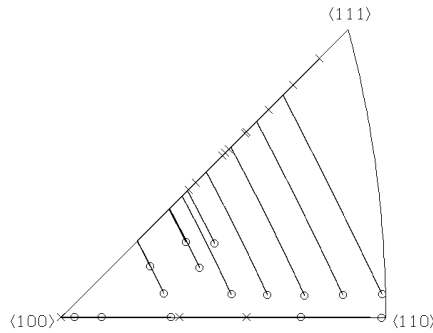


Figure 2.4. Flow chart for sach.s.c.



(a) The stress strain response of the polycrystal and of the three grain sub-sets.



(b) The lattice rotations in 15 specific grains for uniaxial tension to 70% deformation.

Figure 2.5. Stress-strain response and lattice rotations in the Sachs model.

the 'interior' of the unit triangle rotates in 'straight lines', as only one slip system is active at a time. Again the starting orientations are indicated by circles and end orientations by crosses.

As mentioned in section 2.1.2 the predictions of the present Taylor and Sachs models will be compared with the predictions of the self-consistent model in section 2.3.

Direction	Taylor model	Sachs Model
[100]	2.449	2.449
[100], 0 to 10°	2.392	2.242
[110]	3.674	2.449
[110], 0 to 10°	3.594	2.238
[111]	3.674	3.674
[111], 0 to 10°	3.591	2.944
[123], 0 to 5°	3.144	2.155
Average	3.063	2.230

Table 2.2. Calculated m -factors for specific orientations and as average.

2.3 Self-consistent Model

In the simple polycrystal models such as the Sachs and Taylor models described earlier, it is assumed, that elastic anisotropy is negligible during plastic deformation. It is obvious, however, that elastic anisotropy must play a dominant role at the very early stage of plastic deformation (in the elastic-plastic transition range). In this section, the effects of elastic anisotropy in the elastic-plastic transition range and the possible remaining effects within the fully plastic range is investigated using the more sophisticated self-consistent polycrystal deformation model. The model, presented by Hutchinson (Hutchinson 1970), is using elastic-plastic interaction between the inclusions and the continuum matrix, and it is placed somewhere between the upper-bound Taylor type models and the lower-bound Sachs-type models. The present work provides systematic comparisons between the self-consistent model and the upper/lower-bound models.

The present model calculations refer to aluminium, copper and to a hypothetical material with the high elastic anisotropy of copper, and the Young's modulus and work hardening behavior of aluminium. The later hypothetical material (called hybrid) is included in order to make a distinction between the effects of the elastic anisotropy and the work hardening.

The present model is an incremental model with $\{111\} \langle 110 \rangle$ slip as the mechanism for plastic deformation. The self-consistent scheme includes the elastic-plastic interaction between the grains, that are regarded as spherical inclusions in an infinite homogeneous matrix with the overall moduli of the polycrystal. The grains (constituents) are regarded as single crystals with specific orientations represented by the Euler angles (φ_1 , Φ and φ_2). The model is restricted to low strains, as the strain definition does not include second order terms, and the model does not include localisation, which can lead to instabilities such as necking. As a rule, a small strain model is valid as long, as the tangent modulus is much larger than any of the stress components.

The model is governed by the single crystal slip mechanisms, in which the controlling parameters are the critical resolved shear stress and the hardening law. The initial critical resolved shear stress, τ_0 , is assumed to be the same on the 12 well known slip systems in the *fcc* single crystals. The number of slip systems are in fact doubled, as the shear rates are assumed not to be negative. The constituent plastic strain rate, $\dot{\epsilon}_c^P$, is the sum of the shear rate contributions of all the active slip systems as described in section 2.1

$$\dot{\epsilon}_c^P = \sum_i \dot{\gamma}^i \boldsymbol{\mu}^i \quad (2.27)$$

The total strain rate is the sum of the elastic and plastic part as given by

$$\dot{\epsilon}_c = \mathcal{M}_c \dot{\sigma}_c + \dot{\epsilon}_c^P \quad \text{or} \quad \dot{\sigma}_c = \mathcal{L}_c (\dot{\epsilon}_c - \dot{\epsilon}_c^P) \quad (2.28)$$

where \mathcal{L}_c and \mathcal{M}_c are the elastic stiffness and compliance tensors for the single crystals.

The current critical resolved shear stress of the i th slip system is denoted τ^i , and its rate is assumed to be related to the shear rates by a hardening matrix h^{ij} (Hill 1966)

$$\dot{\tau}^i = \sum_j h^{ij} \dot{\gamma}^j \quad (2.29)$$

The components of the hardening matrix is defined as

$$h^{ij} = h_\gamma (q + (1 - q)\delta^{ij}) \quad (2.30)$$

where δ^{ij} is Kronecker's delta. The factor q determines the degree of latent hardening, *e.g.* $q = 0$ provides only self hardening, $q = 1$ provides Taylor hardening and $q > 1$ provides stronger latent hardening than self hardening. The instantaneous hardening coefficient, h_γ , depends on the previous deformation history. In the present model, the relation between the accumulated slip in the grain, γ^{acc} , and the instantaneous hardening coefficient is described by an exponentially decreasing function

$$h_\gamma = h_{final} \left(1 + (h_{ratio} - 1) e^{(-h_{exp} \gamma^{acc})} \right) \quad (2.31)$$

where h_{final} is the final hardening coefficient, h_{ratio} is the ratio between the initial and the final hardening coefficient, and h_{exp} is a parameter determining the strength of the exponential part. This formulation of the hardening law includes the simple linear hardening, that is obtained by choosing $h_{ratio} = 1$. Similar formulations of decreasing hardening using sech^2 and \tanh functions are reported in (Asaro 1983, Harren 1991a and Harren 1991b).

The active slip systems have the resolved shear stress equal to τ , and the resolved shear stress rate equal to $\dot{\tau}$

$$\sigma_c \mu^i = \tau^i \quad \text{and} \quad \dot{\sigma}_c \mu^i = \dot{\tau}^i \quad (2.32)$$

The elastic-plastic instantaneous stiffness tensor for the grain, \mathbf{L}_c , is determined by combining equations 2.27, 2.28, 2.29 and 2.32. For the N active slip systems

$$\sum_j \dot{\gamma}^j X^{ij} = \mu^i \mathcal{L}_c \dot{\epsilon}_c, \quad X^{ij} = h^{ij} + \mu^i \mathcal{L}_c \mu^j \quad (2.33)$$

where X^{ij} and its inverse (Y^{ij}) are $N \times N$ matrices. The slip on the active systems are found as

$$\dot{\gamma}^i = \mathbf{f}^i \dot{\epsilon}_c, \quad \mathbf{f}^i = \sum_k Y^{ik} \mathcal{L}_c \mu^k \quad (2.34)$$

where \mathbf{f}^i is an N vector. \mathbf{L}_c is then found as

$$\mathbf{L}_c = \mathcal{L}_c \left(\mathbf{I} - \sum_m \mu^m \mathbf{f}^m \right) \quad (2.35)$$

where the sum stems from the uncontracted products $\mu_{ij}^m f_{kl}^m$. If all slip systems are inactive, the instantaneous stiffness tensor reduces to the elastic stiffness tensor, $\mathbf{L}_c = \mathcal{L}_c$.

Selection of τ_0 and the hardening coefficients is not trivial. As a rule, τ_0 is assumed be equal to half of the largest principal stress difference at yield, where yield is defined as the point where the first grain becomes plastic; a point that is difficult to determine from a stress-strain curve. In the present calculations, τ_0 and the hardening coefficients (h_{final} , h_{ratio} and h_{exp}) are used as fitting parameters to make the macroscopic stress-strain response of the model resemble the actual

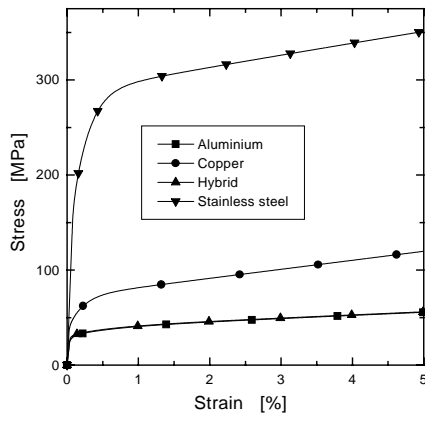


Figure 2.6. The macroscopic stress-strain curves for aluminium, copper, hybrid and stainless steel.

material behavior. The calculated macroscopic stress-strain response for aluminium, copper, hybrid and stainless steel* is shown in figure 2.6 (the stainless steel calculations are used in section 3).

The fitting parameters used in the present calculations are listed in table 2.3 (including the stainless steel parameters). Taylor hardening ($q = 1$) is avoided, as it causes numerical problems in the slip rate calculation, where the set of equations to be solved are no longer independent. It should be underlined, that the marginal latent hardening implied in the q value of 1.01 is nothing but a mathematical trick to avoid ambiguity (the well known Taylor ambiguity problem).

	C_{11} †	C_{12}	C_{44}	$\frac{2C_{44}}{C_{11}-C_{12}}$	τ_0	q	h_{final}	h_{ratio}	h_{exp}
	GPa	GPa	GPa	—	MPa	—	MPa	—	—
Aluminium	108.2	61.3	28.5	1.22	10.9	1.01	40.0	5.0	61.0
Copper	168.4	121.4	75.4	3.21	15.0	1.01	120.0	17.0	200.0
Hybrid	92.2	66.5	41.2	3.21	10.9	1.01	40.0	5.0	61.0
St. steel	204.6	137.7	126.2	3.77	65.0	1.01	140.0	50.0	205.0

Table 2.3. Single crystal stiffnesses (Dieter 1988, Ledbetter 1984) and fitting parameters for the used materials.

The constituent stress and strain rate calculations are done via fourth order concentration tensors as proposed by Hill (Hill 1965a, Hill 1965b). The grains are approximated by spherical single crystals embedded in an infinite homogeneous matrix, whose moduli are the overall instantaneous polycrystal moduli. In this way, the interaction between the grain in consideration and the matrix/polycrystal is taken into account, but the direct grain-to-grain interaction is not incorporated in the model. The stress and strain rates in the spherical inclusions are uniform (Eshelby 1957) and related to the stress and strain rates at infinity by fourth order concentration tensors, \mathbf{A}_c , according to

$$\dot{\epsilon}_c = \mathbf{A}_c \dot{\epsilon}, \quad \mathbf{A}_c = (\mathbf{L}^* + \mathbf{L}_c)^{-1}(\mathbf{L}^* + \mathbf{L}) \quad (2.36)$$

where \mathbf{L}^* is Hill's 'constraint' tensor, that relates to the Eshelby tensor, \mathbf{S} , as

$$\mathbf{L}^* \mathbf{S} = \mathbf{L}(\mathbf{I} - \mathbf{S}) \quad (2.37)$$

*The measured macroscopic stress-strain response for aluminium, copper and austenitic stainless steel is shown in section 5.2

†In these well known expressions for the single crystal stiffnesses the normal contracted tensor notation is used, rendering $C_{11} = C_{1111}$, $C_{12} = C_{1122}$ and $C_{44} = C_{2323}$

The relationship between the Eshelby tensor, \mathbf{S} , and the overall stiffness tensor, \mathbf{L} , is given by Kneer's fourth order tensor $\mathbf{\Lambda}$ (Kneer 1965) and using equation 2.37, Hill's 'constraint' tensor can be found as

$$\mathbf{L}^* = \mathbf{\Lambda}^{-1} - \mathbf{L} \quad (2.38)$$

$\mathbf{\Lambda}$ is determined from the double integral

$$\Lambda_{ijmn} = \frac{1}{16\pi} \int_{\theta=0}^{\pi} \int_{\phi=0}^{2\pi} \left(\hat{U}_{im} k_n k_j + \hat{U}_{jm} k_n k_i + \hat{U}_{in} k_m k_j + \hat{U}_{jn} k_m k_i \right) \sin \theta d\theta d\phi \quad (2.39)$$

where \hat{U} is found from

$$L_{ijkl} \hat{U}_{km} k_j k_l = \delta_{im} \quad (2.40)$$

and $k_1 = \sin \theta \cos \phi$, $k_2 = \sin \theta \sin \phi$ and $k_3 = \cos \theta$.

The stress and strain rates at infinity in the matrix are identified with the polycrystal quantities $\dot{\boldsymbol{\sigma}}$ and $\dot{\boldsymbol{\varepsilon}}$. Thus, the constituent stress and strain rates are estimated by the solution to a problem in linear anisotropic elasticity. The elastic-plastic interaction between the inclusions and the matrix is incorporated, as the concentration tensor and the constraint tensor are determined from the instantaneous elastic-plastic stiffness tensor.

The polycrystal stress and strain rates are equal to the weighted stress and strain rate average of all the grains, and denoting the average of all the grains by $\{ \}$, it follows that

$$\{ \dot{\boldsymbol{\sigma}}_c \} = \dot{\boldsymbol{\sigma}} \Rightarrow \mathbf{L} = \{ \mathbf{L}_c \mathbf{A}_c \} \quad (2.41)$$

At a certain stage of deformation the stress, and thereby the potentially active slip systems in the constituents of the polycrystal are known. The polycrystal is prescribed an additional strain rate, $\dot{\boldsymbol{\varepsilon}}$, and using the present model, it is possible to determine the stress and strain rates, $\dot{\boldsymbol{\sigma}}_c$ and $\dot{\boldsymbol{\varepsilon}}_c$, as well as the instantaneous constituent moduli, \mathbf{L}_c , for all the grains, and the polycrystalline quantities, $\dot{\boldsymbol{\sigma}}$ and \mathbf{L} , are determined as the appropriate average of all the grains.

In the present calculations the initial texture is described with a set of 5000 grains representing a random texture. The lattice orientations are described using the Euler angles, φ_1 , Φ and φ_2 (Bunge 1982). The relatively high grain number is necessarily, as the material response of several grain sub-sets are needed in the investigation of intergranular strains in section 3.

The present self-consistent polycrystal deformation model is implemented in an ANSI C program, `sc_model.c`. A thorough description of the implementation is given in (Clausen and Lorentzen 1997a).

2.3.1 Model Predictions

In the following the development of relevant polycrystal deformation parameters are described. It is chosen to concentrate on parameters, that relate closely to the crystallographic slip, as this is the basis of the model. Furthermore, focus is on the elastic anisotropy and its bearing on polycrystal deformation in the elastic-plastic transition range as well as in the fully plastic regime.

2.3.1.1 Elastic Moduli There is great difference in the degree of the elastic anisotropy of the materials considered in the present work (aluminium, copper and hybrid). The stiffness of a grain in the tension direction, in this case calculated as the Kröner stiffnesses (Kröner 1958), shows strong orientation dependence. This is described in figure 2.7 for aluminium and copper, whereas the hypothetical

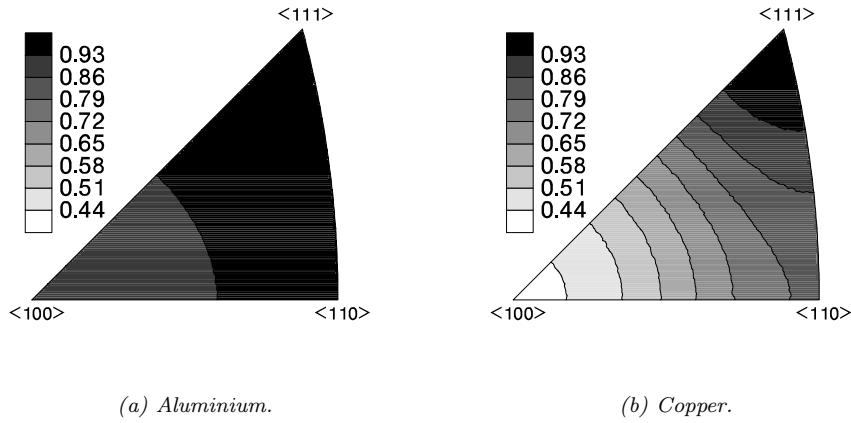


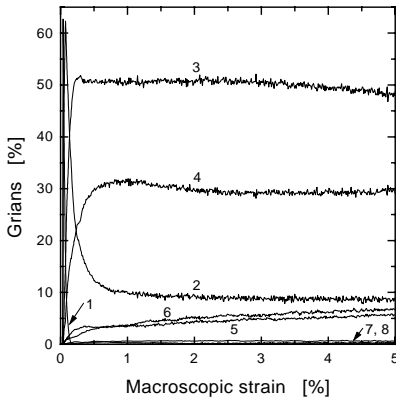
Figure 2.7. The normalised Young's modulus as a function of the orientation.

material, hybrid, is omitted, as its elastic anisotropy is identical to the one in copper. The figure shows the modulus normalised with respect to the maximum value for the $\langle 111 \rangle$ orientation, 75.4 GPa and 184.3 GPa for aluminium and copper respectively. For Kröner stiffness values of specific orientations see table 3.3 in section 3.2.1.

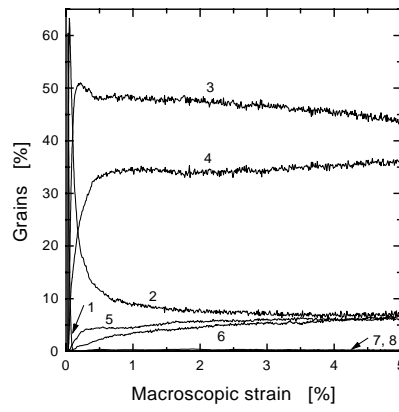
The variation is identical for all *fcc* materials, but the numerical values are dictated by the elastic anisotropy. The variation in copper is much more pronounced than in aluminium, as shown in figure 2.7, where the minimum values are 0.86 and 0.41 for aluminium and copper respectively.

2.3.1.2 Number of Active Slip Systems In the present model the number of active slip systems in the grains (constituents) are determined by the stress state in the grain. In a Taylor model, which is based on the assumption, that all grains experience the same strain, the number of active slip systems will always be five in order to accommodate the five independent strain components. In a Sachs model, which is based on the assumption that the stress state in all the grains are the same, only the grains that are oriented along symmetry lines have more than one active slip system. The number of active slip systems in a grain calculated with the present self-consistent model varies according to the deformation and the grain orientation. In figure 2.8 the percentages of grains with a given number of active slip systems are shown as a function of the macroscopic strain for all three materials.

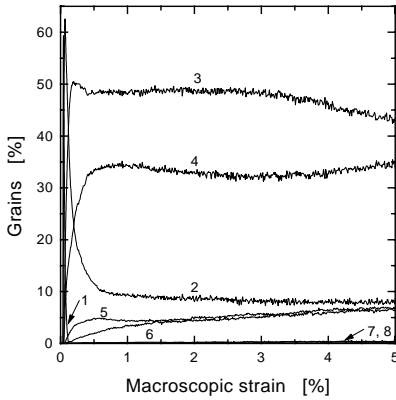
Initially, only one slip system is active, then more systems follow as it appears from the large percentage of grains with one and two active slip systems at onset of yield. After only 0.5% strain approximately 50% of the grains have three active slip systems and only approximately 10% of the grains have five, or more, active slip systems. For the present model, where the grains interact with the matrix/polycrystal, it is interesting to note that 90% of the grains do not need five active slip systems to accommodate the applied strain. In spite of the fact that it is never necessary with more than five active slip systems, some of the grains do, however, have up to eight active slip systems due to the high symmetry in the *fcc* lattice. The average number of active slip systems is almost the same for all the materials as shown in figure 2.8(d) (note the scale). In the early stages of plastic deformation, the average number of active slip systems for the hypothetical material (hybrid) follows the one for aluminium, but at approximately 2.5%



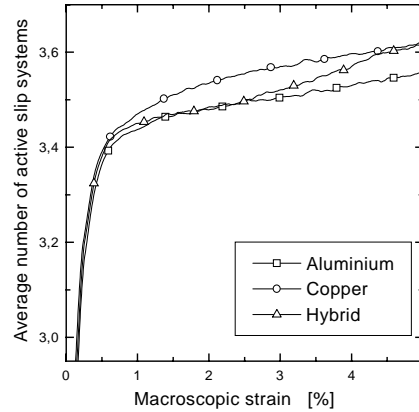
(a) Aluminium.



(b) Copper.



(c) Hybrid.



(d) Average number of active slip systems.

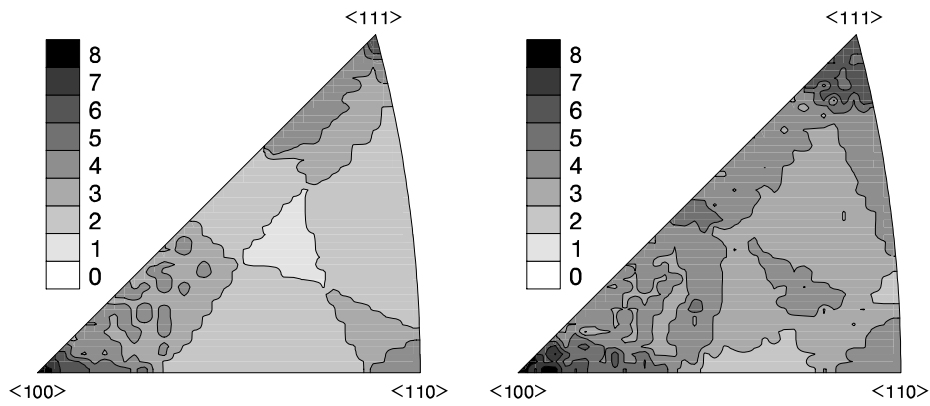
Figure 2.8. The number of active slip systems as a function of the deformation.

deformation it increases to the same level as in copper.

The general trend is the same for all three materials, indicating that the number of active slip systems is determined by the crystallographic structure. The main difference between aluminium and copper is the relatively small deviations in the percentage of grains with five and six active slip systems at zero to one percent deformation and the percentage of grains with three and four active slip systems over two percent deformation. In the hypothetical material the percentages in these areas resemble the ones in copper indicating that the elastic anisotropy has a larger effect on the number of active slip systems than does the work hardening.

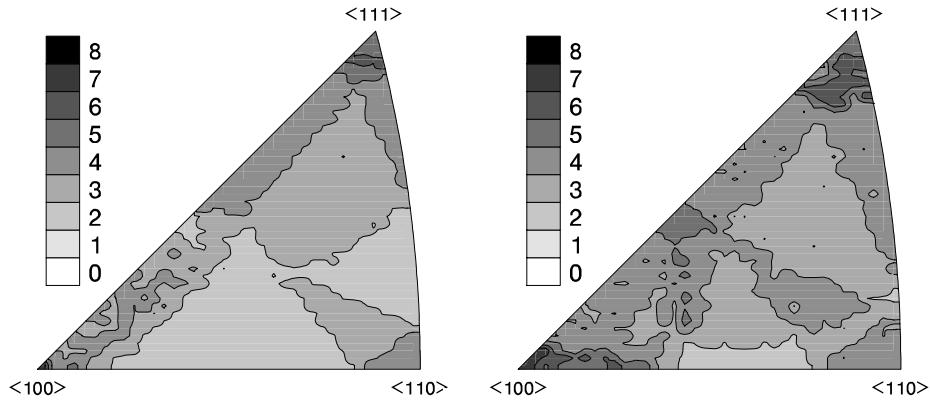
The orientation dependence of the number of active slip systems in the grains is shown as inverse pole figures in figure 2.9 for plastic strain values of 0.1 and 1 in all three materials. As for the average number of active slip systems, the orientation dependence is similar in aluminium and copper indicating that this is mainly dictated by the *fcc*-structure and is only marginally effected by the elastic anisotropy and the work hardening.

At the $\langle 110 \rangle$ orientation the grains have four active slip systems, at the $\langle 111 \rangle$ orientation the grains have up to six active slip systems and at the $\langle 100 \rangle$ orientation the grains have up to eight active slip systems. This is in agreement with the two-,



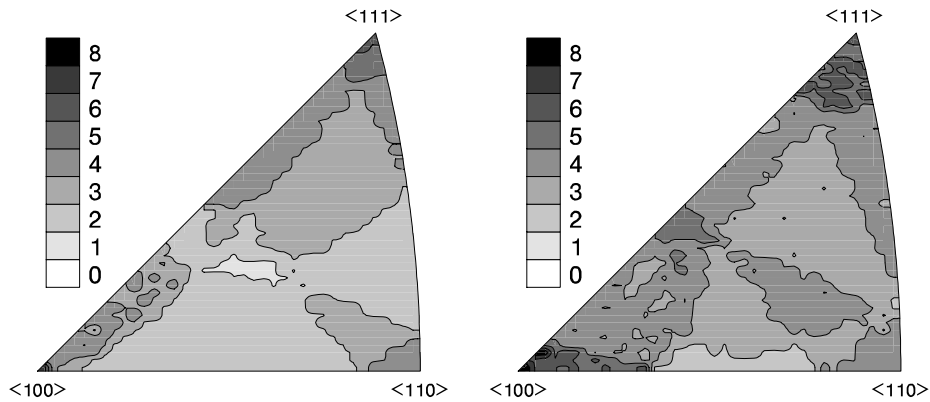
(a) Aluminium at $\varepsilon^P = 0.1\%$.

(b) Aluminium at $\varepsilon^P = 1\%$.



(c) Copper at $\varepsilon^P = 0.1\%$.

(d) Copper at $\varepsilon^P = 1\%$.



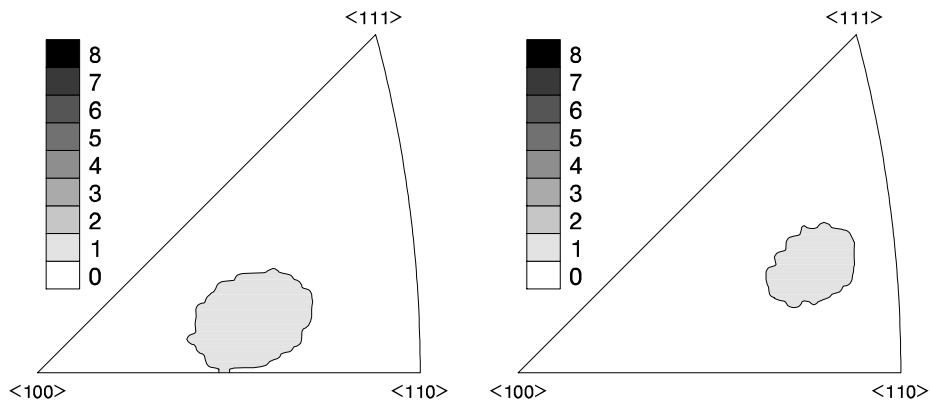
(e) Hybrid at $\varepsilon^P = 0.1\%$.

(f) Hybrid at $\varepsilon^P = 1\%$.

Figure 2.9. The number of active slip systems as a function of the orientation at $\varepsilon^P = 0.1\%$ and at $\varepsilon^P = 1\%$.

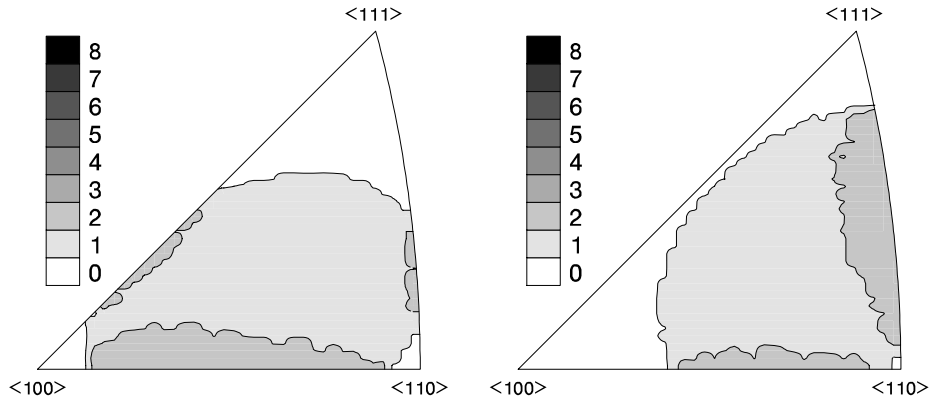
three- and four-fold rotation symmetries in the *fcc* lattice.

The pole figures are very similar in aluminium and copper; at 0.1% plastic deformation there are some differences in the upper third of the unit triangle, where copper has relatively large regions with three active slip systems and aluminium mainly has two active systems. The pole figure for hybrid is closest to the one



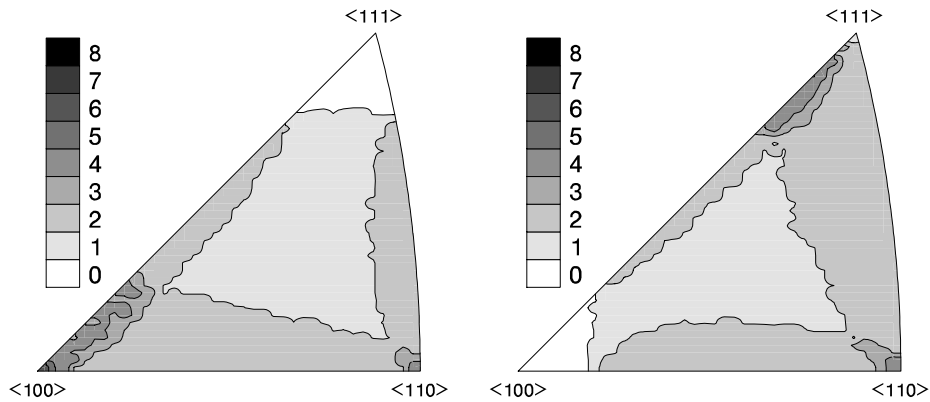
(a) Aluminium at $\epsilon^P = 0.001\%$.

(b) Hybrid at $\epsilon^P = 0.001\%$.



(c) Aluminium at $\epsilon^P = 0.005\%$.

(d) Hybrid at $\epsilon^P = 0.005\%$.



(e) Aluminium at $\epsilon^P = 0.011\%$.

(f) Hybrid at $\epsilon^P = 0.011\%$.

Figure 2.10. The number of active slip systems as a function of the orientation at the early stages of plasticity.

for copper, but there are no major differences between the three materials. At 1% plastic deformation it is not possible to determine which of the two pole figures the one for the hypothetical material resembles the most. In the fully plastic region (above 1% deformation) the orientation distribution is practically the same in all three materials.

The influence of the elastic anisotropy is only observed in the very early stages of plasticity. The orientation dependence of the number of active slip systems is determined at very low plastic strains for aluminium and hybrid (at these levels of plastic deformation hybrid and copper are identical). The inverse pole plots for 0.001%, 0.005% and 0.011% plastic deformation are shown in figure 2.10.

As seen in figure 2.10(a) and 2.10(b), the region where slip starts to occur is different in the two materials. In figure 2.10(c) and 2.10(d) about 75% of the grains have one or two active slip systems, and it is seen that the areas with active slip systems are very different in the two materials. At 0.011% plastic deformation (figure 2.10(e) and 2.10(f)) aluminium, without pronounced elastic anisotropy and hence without pronounced stress repartition in the elastic regime, slip has started in the regions next to $\langle 100 \rangle$ and $\langle 110 \rangle$ which have the same m-factor (and the same Schmid factor, *e.g.* section 2.3.1.3), whereas slip has not started in the region next to $\langle 111 \rangle$ which has a higher m-factor. In the hybrid material, with its rather strong elastic anisotropy, there is stress repartition in the elastic regime: load is transferred from the region next to $\langle 100 \rangle$ to the region next to $\langle 111 \rangle$ (*e.g.* figure 2.7(b)). The result is that slip has started next to $\langle 111 \rangle$ and next to $\langle 110 \rangle$ in spite of the high m-factor, whereas slip has not started next to $\langle 100 \rangle$ - with a m-factor much lower than that for $\langle 111 \rangle$ and equal to that for $\langle 110 \rangle$.

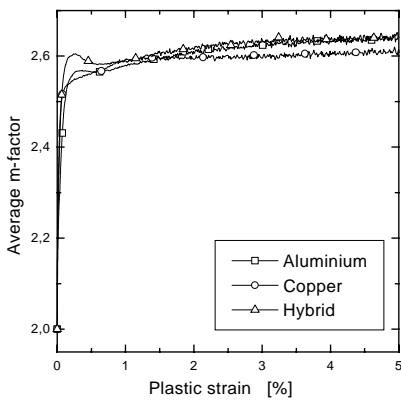
2.3.1.3 The m-factor The m-factor, $m = \sum_i \dot{\gamma}^i / \dot{\epsilon}_{11}^P$, has been determined for a rigid plastic Taylor model and a rigid plastic Sachs model as described in sections 2.1 and 2.2. The average m-factor for these models is found to be 3.063 and 2.230 respectively. In the present model the average m-factor in the elastic-plastic transition range increases from a value of two as more and more grains become plastic. As seen in figure 2.11(a) the average m-factor is approximately 2.6 in the plastic regime for all the materials. The average m-factor is very similar in aluminium and copper (note the scale). After about 1% deformation the average m-factor for the hypothetical material is almost identical to the one for aluminium.

The orientation dependence of the m-factor is shown as inverse pole figures in the figures 2.11(b) to 2.11(d) for the three materials and the corresponding inverse pole figures for the Taylor and Sachs models are shown in the figures 2.11(e) and 2.11(f).

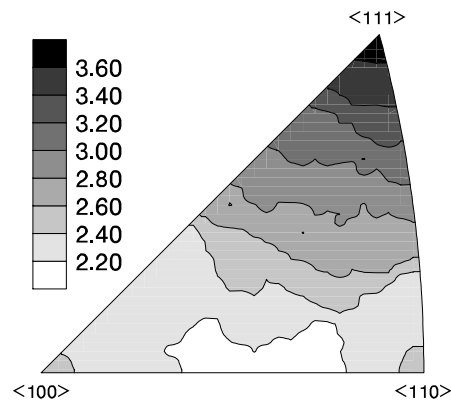
The m-factor orientation distribution calculated according to the present model is quite similar for all three materials, but comparing the average m-factor for the three materials it is seen that after approximately 1% deformation the hypothetical material is very close to aluminium. This indicates that the work hardening has a very small effect on the amount of slip in the grains.

According to figure 2.11, the m-factor orientation dependence in the present model lies somewhere between the ones for the Taylor model and the Sachs model. The m-factor values near the $\langle 100 \rangle$ and $\langle 111 \rangle$ orientations are similar to the ones for the Taylor model but in the rest of the pole figure the contour lines differ greatly from the ones in the Taylor model. The m-factor for the present model at the three corners of the unit triangle ($\langle 100 \rangle$, $\langle 110 \rangle$ and $\langle 111 \rangle$) are identical to the values in the Sachs model, and the area along the $\langle 100 \rangle - \langle 110 \rangle$ symmetry line with a rather low m-factor is also similar to the Sachs model, although the area is much larger in the Sachs model and that it stretches further up toward the $\langle 111 \rangle$ orientation than in the present model.

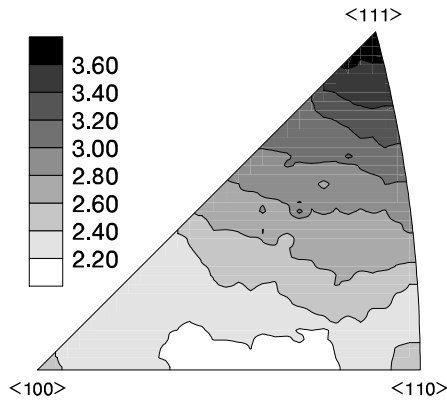
2.3.1.4 Lattice Rotations As the polycrystal is deformed plastically, the lattice orientation in the grains change due to the crystallographic slip. The lattice rotations in the grains can be determined as described in section 2.1.1. The lattice rotation variation in all three materials is shown in figure 2.12 together with the corresponding inverse pole figure for calculations with the Taylor and the Sachs



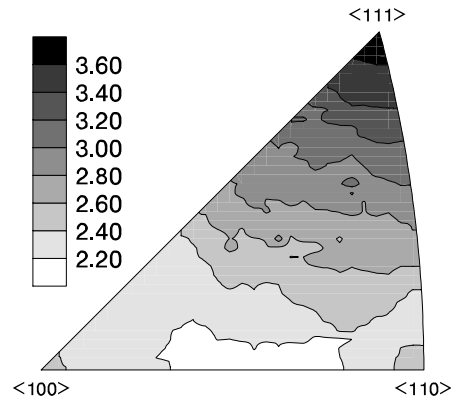
(a) Average m -factors as function of the deformation.



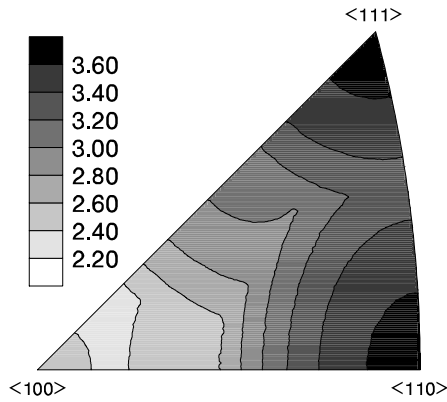
(b) Aluminium at $\epsilon^P = 0.5\%$.



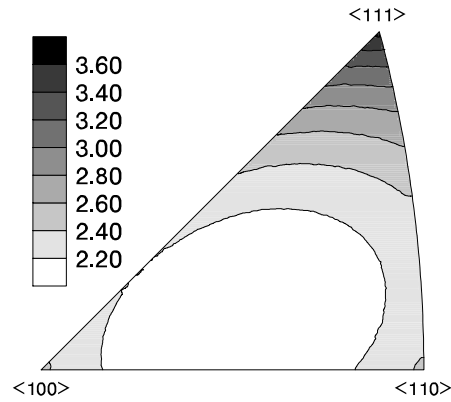
(c) Copper at $\epsilon^P = 0.5\%$.



(d) Hybrid at $\epsilon^P = 0.5\%$.



(e) Taylor model.



(f) Sachs model.

Figure 2.11. The calculated m -factor as a function of the orientation.

models. The arrows indicate the direction of the orientation change but the arrow length is chosen arbitrarily and does *not* indicate the amount of rotation, as the rotations are very small for the deformations considered here.

The general orientation flow-line pattern is quite similar for the three materials, as seen in figure 2.12(a) to 2.12(c). All three materials have two regions: one with

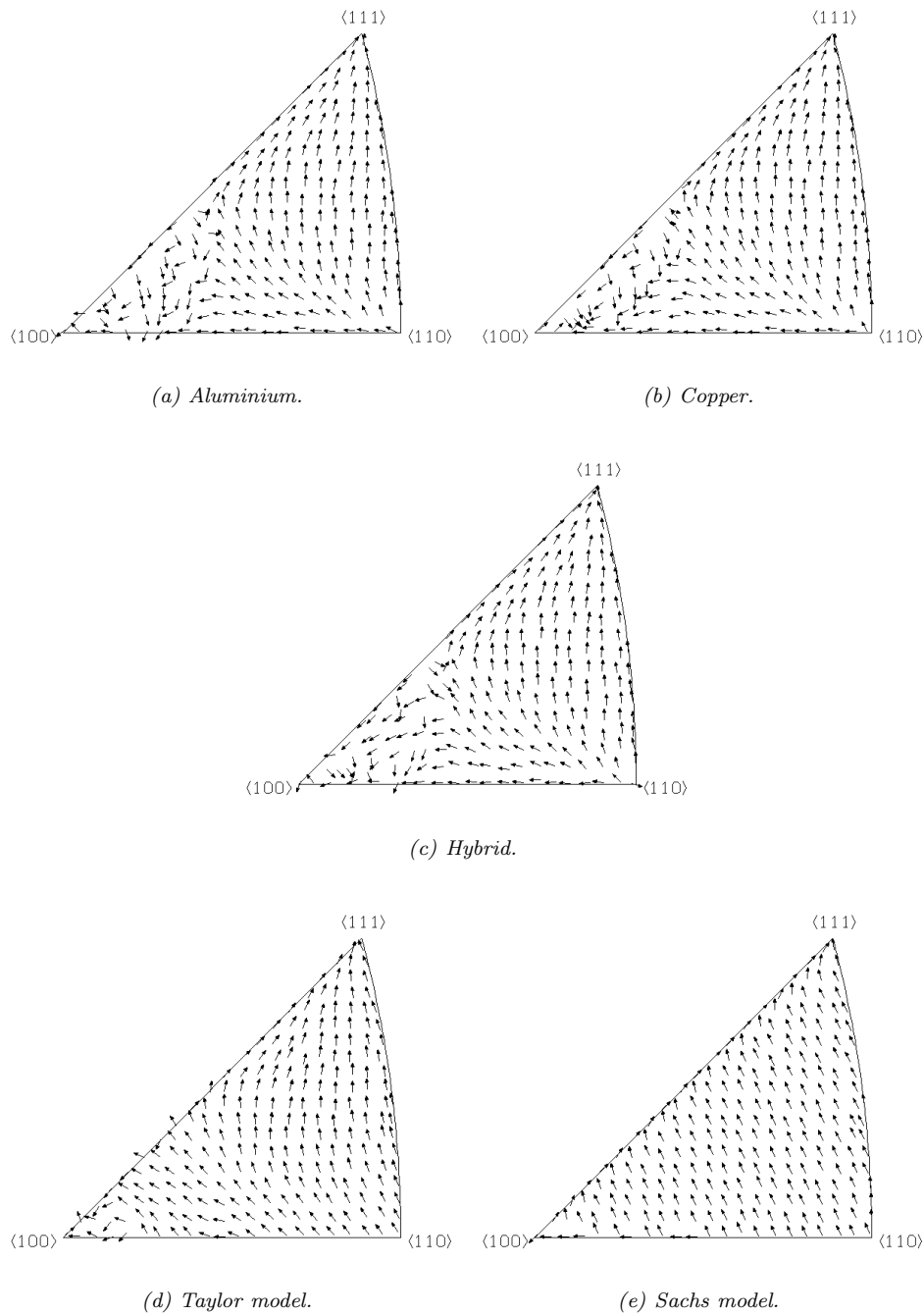


Figure 2.12. The lattice rotations from 3 to 5% deformation as a function of the orientation.

a general trend to rotate towards $\langle 111 \rangle$ and one with a general trend to rotate towards $\langle 100 \rangle$ in agreement with all experimental observations on the texture of uniaxially deformed *fcc* materials (similar rotation patterns are reported for several different models in Leffers 1988). The respective areas of these two regions are quite similar for the three materials. In order to detect a difference between the three materials one has to focus on the 'chaotic' region in the vicinity of $\langle 100 \rangle$. The extent of this region is similar for aluminium and hybrid and somewhat different for copper. The orientation flow-line pattern for the Taylor and the Sachs models, figure 2.12(d) and 2.12(e), deviate from those derived from the present model:

the region with a general trend to rotate towards $\langle 100 \rangle$ is somewhat smaller for the Taylor model and much smaller for the Sachs model, and the chaotic region (only observed for the Taylor model) is quite small. For the Sachs model it is noteworthy that the lattice rotations do follow the general pattern of rotation either towards $\langle 100 \rangle$ or towards $\langle 111 \rangle$ (even though rather few grains rotate towards $\langle 100 \rangle$). Normally a different rotation pattern is quoted for the Sachs model, *viz.* initial rotation towards the $\langle 100 \rangle$ - $\langle 111 \rangle$ side of the triangle and then rotation along the side towards $\langle 211 \rangle$. This difference stems from the use of different rules for the lattice rotation (Hosford 1977, Leffers and Lebensohn 1996). In the present calculations, the 'mathematical analysis' (as expressed in equation 2.11) is used, which is the best choice for equiaxed grains. The rotation towards $\langle 211 \rangle$ (which is the lattice rotation observed in single crystal strained in tension) is derived from 'Schmid tension analysis' (Hosford 1977).

2.4 Summary

The present elastic-plastic self-consistent model includes the elastic and plastic anisotropy of the materials, and it is straight forward to calculate the elastic strain components in grain sub-sets, which facilitates the correlation with the neutron diffraction measurements.

The model predictions for aluminium, copper and a hypothetical material, hybrid, with the anisotropy of copper and the Young's modulus and hardening properties of aluminium have been used to determine the influence of elastic anisotropy and work hardening in the plastic regime.

The numerical predictions by the self-consistent model imply that the dominating deformation mode in the present self-consistent polycrystal model is one, in which grains have three active slip systems. Approximately 50% of the grains accommodate the deformation by three active slip systems, while less than 10% of the grains utilise the general five active slip systems used in the Taylor model. The average number of active slip systems is about 3.55 for the three materials, which is between the numbers for the Taylor and Sachs models (actually closest to the Sachs model). The average m-factor is about 2.6 for the three materials, which again lies between the values for the Taylor and the Sachs models. The general trends in the orientation dependence of the m-factor mostly resembles the one in the Sachs model.

The calculations for the hypothetical material, hybrid, indicates that the elastic anisotropy only has an effect in the very early stages of plasticity. After few tenth of a percent plastic deformation, the number of active slip systems and the m-factor is very similar for the three materials. This indicates that these parameters are mainly dictated by the *fcc* crystal structure, and only marginally effected by the elastic anisotropy and the work hardening.

The lattice rotation pattern for the three materials calculated with the self-consistent model resembles the one for the Taylor model the most, as the lattice rotation pattern calculated with the Sachs model are almost unidirectional. The rotation pattern in all three models are leading to the well known $\langle 111 \rangle$ - $\langle 100 \rangle$ fiber texture for uniaxial tension of *fcc* metals.

Comparing the self-consistent modelling scheme with the Taylor and the Sachs models, the m-factor orientation distribution indicates that the self-consistent model resembles the Sachs model, whereas the lattice rotations show that the self-consistent model predicts a rotation pattern that mainly resembles the one for the Taylor model. These observations logically places the self-consistent model somewhere between the upper- and lower-bound models.

The investigated parameters; slip, active systems and m-factors, do not easily lend themselves to experimental verification, and as the lattice rotations are so small that they do not result in a measurable texture for the used deformation degrees, other quantities must be selected for a rigorous experimental verification of the micro-mechanics behind the modelling schemes. The micro-mechanical quantities that do lend themselves to experimental evaluation are the stress and strains in the grains. A method of directly measuring these quantities is the novel technique of lattice strain characterisation by neutron diffraction that allows probing of the elastic lattice strain evolution in selected grain sub-sets. This type of model evaluation is presented in section 5. Additionally the predictions of the self-consistent modelling scheme can be used to determine the reflections that are suitable for technological applications of neutron diffraction. This aspects of the modelling scheme will be presented in section 3.

3 Implications for Diffraction Measurements

The macroscopic residual stresses/internal stresses measurement, type-1 stresses (Macherauch and Kloos 1986), by diffraction methods is based on the measurement of deviations in lattice spacing for specific crystallographic planes (deviations from the lattice spacings in stress-free material). In an ideal world, there would be one linear relation between the lattice spacing deviation and the macroscopic stress. However, introduction of elastic anisotropy, with the resulting intergranular stresses or type-2 stresses (Macherauch and Kloos 1986), implies that there is not only one but several linear relations, depending on the selected lattice plane. The measurement of interest, macroscopic stresses, are in most cases associated with plastic deformation. Because of the plastic anisotropy this again implies that there are several relations, but it also implies that the relations are not necessarily linear.

In this section the present self-consistent polycrystal deformation model is used to select the best suitable reflections for stress and strain measurements. The ideal reflection, is one, that has a linear relationship between the applied stress and the elastic strain. In this investigation, the reflection with the smallest linearity deviation in the relation between the applied stress and the elastic strain is selected as the best suitable reflection for technological applications of neutron diffraction. Furthermore, the reflection must have a relative small build-up of residual lattice strains due to previous plastic deformation, as these residual strains will influence the measurements and thereby make the overall stress and strain determination more difficult.

The non-linearities of the reflections are compared with the normal strain resolution in a neutron diffraction measurement, discussed in section 4.1.1 and in appendix A. In both the fixed wavelength and the *time-of-flight* measurements, the normal strain resolution is about $\pm 50 \times 10^{-6}$ and linearities less than the strain resolution will be difficult to detect in a diffraction measurement.

In the present calculations the lattice spacing deviations or the lattice strains for a number of lattice planes parallel to and perpendicular to the tensile axis for uniaxially loaded aluminium, copper and austenitic stainless steel, are determined using the present self-consistent polycrystal model. The results are relevant for lattice-strain measurements by diffraction methods in general, but they are viewed with particular reference to neutron diffraction measurements, which monitor bulk stresses as opposed to conventional X-ray measurements of the stresses in thin surface layers.

As outlined above, the basic aim of this work is to provide a rational theoretical background for the macroscopic stress measurements, or type-1 stress measure-

ments. As also outlined above, such measurements are made via measurements of lattice strains in grains with specific lattice orientations. The lattice strains determined by such measurements are influenced by both type-1 and type-2 stresses, and therefore the type-2 stresses must be subtracted from the results.

3.1 Calculations

The information to be presented is obtained through modelling as described in section 2.3 (with 5000 grains of initially random orientation). The input parameters for all three materials (aluminium, copper and austenitic steel) were presented in table 2.3 and the calculated uniaxial stress-strain curves for the three materials were shown in figure 2.6. For steel, the macroscopic tensile data come from an austenitic steel, and the single crystal stiffnesses come from a FeCrNi alloy with a slightly different main composition. The two compositions are given in table 3.1.

	Cr	Ni	Mo	Mn	Si	C
Single crystal (Ledbetter 1984)	19.0	10.0	—	—	—	—
Polycrystal	18.25	13.42	3.66	1.48	0.44	0.02

Table 3.1. Chemical composition of the stainless steel in weight percent.

In normal experimental practice grains within $\pm 0.5^\circ$ from the specified direction contribute to the registered intensity. In order to get acceptable statistics grains up to $\pm 5^\circ$ from the specified main direction are included in the calculations as discussed in section 5.2. It is assumed that this increased tolerance does not have any major effect on the results other than improve the statistics of the numerical results.

	1	2	3	4	5	6
<i>hkl</i>	111	200	220	311	331	531
Multiplicity	8	6	12	24	24	48

Table 3.2. Reflections and their multiplicity.

The lattice strains have been calculated for all crystallographic planes with Miller indices up to $\{531\}$, which is the unsymmetrical *fcc* reflection with the lowest indices (forbidden reflections in the *fcc* lattice, higher-order lattice planes and lattice planes corresponding to two families of lattice planes are ignored). Only results for the lattice planes listed in table 3.2 are quoted (420 and 422 are excluded to reduce the amount of data in the illustrations). The crystallographic multiplicities of the lattice planes, which is a factor of practical importance, is also given in table 3.2. The reflected intensity in polycrystal diffraction experiments depends on the multiplicity as the fraction of grains participating in the measurement is proportional to the multiplicity, see appendix A.1. Other parameters, such as the structure factor and the absorption factor also influences the diffracted intensity (Noyan and Cohen 1987).

3.2 Results

The results of the calculations are presented in the following sub-sections: the elastic Kröner stiffness (diffraction elastic constants) of the reflections are determined in section 3.2.1; the (elastic) lattice strains versus the applied load is discussed

in section 3.2.2; the relative standard deviation and the linearity deviation of the results in section 3.2.2 are determined in sections 3.2.3 and 3.2.4; the general deformation pattern is determined in terms of the normalised stresses within the reflections in section 3.2.5; and the residual lattice strain after unloading from different stress levels are discussed in section 3.2.6. In section 3.2.4, 3.2.5 and 3.2.6 the results are presented in the conventional way with the predetermined parameter (the strain) along the x axis and the results along the y axis. In section 3.2.2, 3.2.3 and 3.2.4 the results are presented differently - with the predetermined parameter (the applied stress) along the y axis and the results (the elastic lattice strains and their relative standard deviations) along the x axis - in order to approach the presentation in a conventional stress-strain curve.

The results should be evaluated in terms of the ideal requirement of finding a reflection with a linear relation between the measured lattice strains and the actual state of macroscopic internal/residual stress. In this connection it is relevant to remember the difference in elastic anisotropy of all three materials dealt with as expressed by $2C_{44}/(C_{11} - C_{12})^{\ddagger}$; for aluminium it is 1.22, for copper it is 3.21, and for austenitic steel it is 3.77. In the presentation of the calculations for the six reflections, symbols are superimposed at various stress levels to aid the eye separating the lines.

3.2.1 Diffraction Elastic Constants

When determining the stresses in a component from the measured elastic lattice strains the so-called diffraction elastic constants are utilised. In the present model calculations these diffraction elastic constants for specific reflections are determined as the Kröner stiffnesses (Kröner 1958) in the elastic region. The diffraction elastic constants for random texture are shown in table 3.3 for aluminium, copper and austenitic stainless steel. In samples with texture the values will change due to the change in the macroscopic properties.

	E_{111}	E_{200}	E_{220}	E_{311}	E_{331}	E_{531}
Aluminium	75.4	64.9	72.6	69.6	73.4	71.4
Copper	184.3	76.8	147.4	116.1	157.1	133.0
Stainless steel	291.5	109.7	227.9	173.8	243.5	202.2

Table 3.3. Diffraction elastic constants of specific reflections.

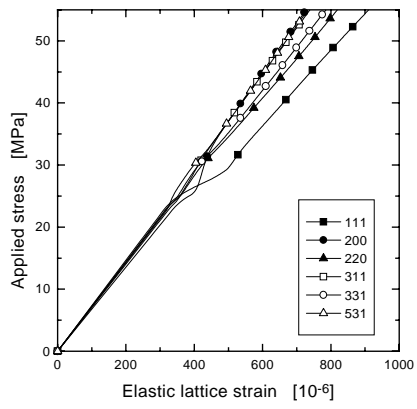
The validity of using the Kröner stiffnesses as the diffraction elastic constants are investigated in section 5.

3.2.2 Elastic Lattice Strains

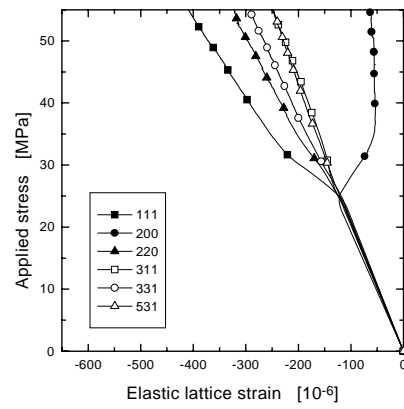
The build-up of intergranular strains during load is shown in figure 3.1 for the three materials. The applied stress is shown as a function of the elastic lattice strains parallel and perpendicular to the tensile axis for the six reflections. The lattice strain for a given reflection is determined by the stress state in the corresponding grains. Load redistribution between the grains therefore leads to changes in the lattice strains.

As seen in figure 3.1, the degree of redistribution of the load between the reflections increases as the elastic anisotropy increases, where aluminium has the weakest elastic anisotropy and stainless steel the strongest. One should note the

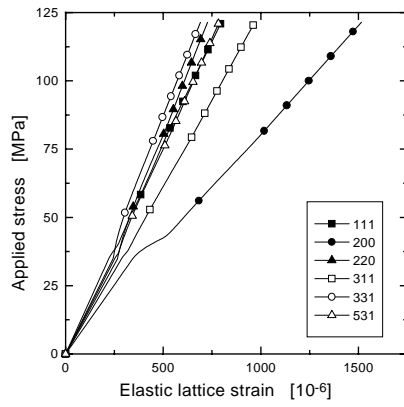
[‡]Using the normal contracted tensor notation as in table 2.3



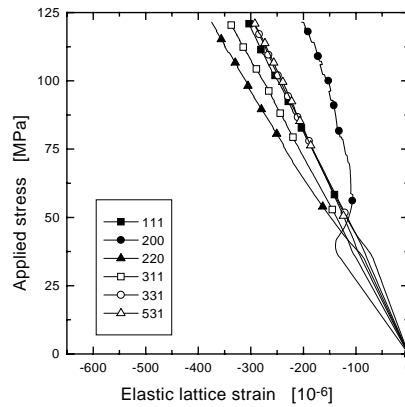
(a) Aluminium, parallel to the tensile axis.



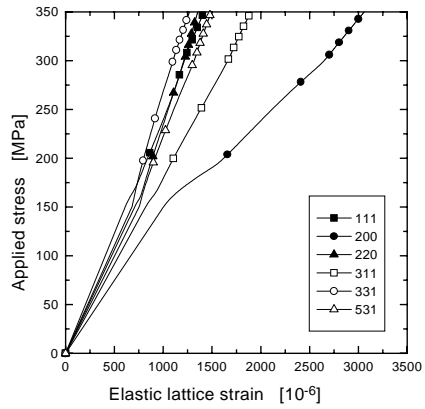
(b) Aluminium, perpendicular to the tensile axis.



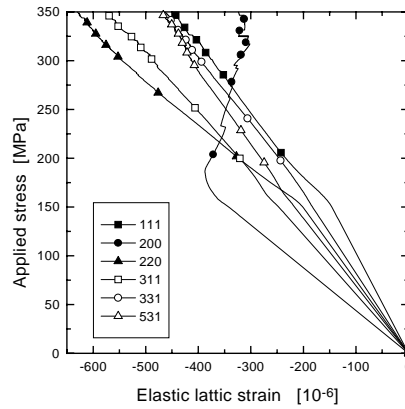
(c) Copper, parallel to the tensile axis.



(d) Copper, perpendicular to the tensile axis.



(e) Stainless steel, parallel to the tensile axis.



(f) Stainless steel, perpendicular to the tensile axis.

Figure 3.1. The applied stress versus the elastic lattice strain.

scale difference in the figures. This redistribution of the load is determined by a combination of the elastic and the plastic anisotropy of the material.

The strain redistribution is quite similar in stainless steel and copper, which both have a relatively high anisotropy and thereby relatively large differences in the stiffnesses of the reflections, see figure 2.7 and table 3.3. Parallel to the tensile axis, the two elastically softest reflections, 200 and 311, remain the softest in the plastic region, and the 331- and 220-reflections become the stiffest. Perpendicular to the tensile axis the 220-reflection becomes the softest reflection.

In aluminium, the strain redistribution is different from the one in the other two materials due to the relatively low anisotropy. Parallel to the tensile axis, the elastically stiffest reflection, 111, experiences the highest strain in the plastic region for a given applied load, as it becomes the softest reflection in the plastic region and the elastically softest reflection, 200, becomes one of the stiffest in the plastic region. Perpendicular to the tensile axis, the redistribution is almost the same, as the 111-reflection become the softest reflection in the plastic regime and the 200-reflection becomes the stiffest. The strain value differences in aluminium are rather small compared with the strain resolution in a neutron diffraction measurement ($\pm 50 \times 10^{-6}$) which makes them difficult to observe in measured data.

In all three materials the 200-reflection perpendicular to the tensile axis is showing a radical change from the onset of plasticity. This behaviour is discussed in section 3.2.3

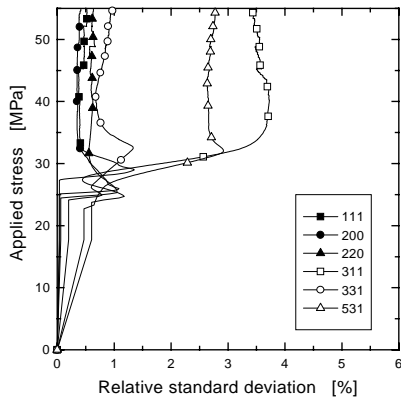
3.2.3 Elastic Lattice Strain Variations

When focusing on specific sub-sets of grains all having the same hkl -lattice plane normal in a direction parallel to the tensile axis, all grains in this family shows nearly the same elastic lattice strain as the deformation is rotationally symmetric. When focusing on specific grain sub-sets all having the same hkl -lattice plane normal in a direction perpendicular to the tensile axis the elastic lattice strain show a much greater variation. A rotation of a grain around a direction perpendicular to the tensile axis drastically changes the stiffness in the tensile direction, and thereby the stress and strain state in the grain.

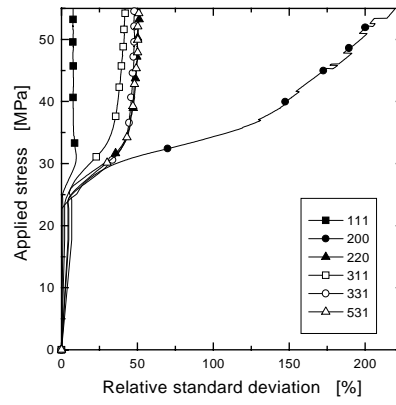
In the elastic region the elastic lattice strain variation is caused by the orientation differences between the grains, but in the plastic region the relationship between the elastic and plastic properties also influences the elastic lattice strain variation. In the plastic region the load carried by the grains are determined by the *plastic* anisotropy, but the elastic lattice strains are determined by the *elastic* anisotropy. In figures 3.2 the strain variation is presented as the relative standard deviation of the elastic lattice strain within the grain sub-sets (the relative standard deviation is the standard deviation divided by the strain).

Parallel to the tensile axis, the relative standard deviation is within 5 – 6%, but perpendicular to the tensile axis the relative standard deviation is much higher, see figure 3.2. The generally high relative standard deviation perpendicular to the tensile axis is caused by the larger difference in stiffness of the grains and by the lower strain level (the Poisson effect).

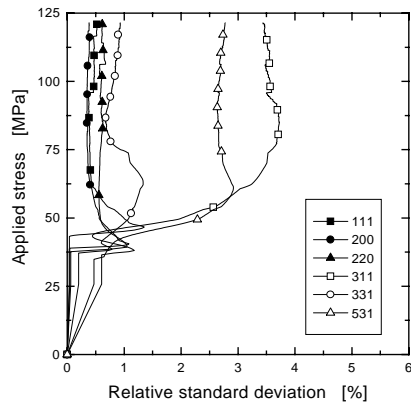
For all three materials the 200-reflection perpendicular to the tensile axis experiences a radical change in the stress-strain curve (figure 3.1) and the determined relative standard deviation is likewise very high. This rather surprising behaviour of the 200-reflection, is due to the combination of grains that constitute the reflection. All the grains that have a $\langle 200 \rangle$ lattice plane normal in a direction perpendicular to the tensile axis, at the same time has a $\langle hk0 \rangle$ (or $\langle h00 \rangle$) lattice plane normal in the tensile direction. In an inverse pole figure of the *fcc* lattice structure all the grains that constitute the 200-reflection is within the region shown by the dotted line in figure 3.3(a).



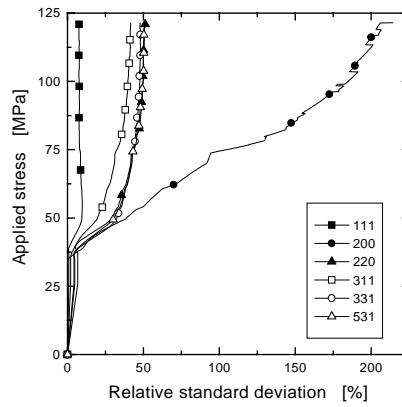
(a) Aluminium, parallel to the tensile axis.



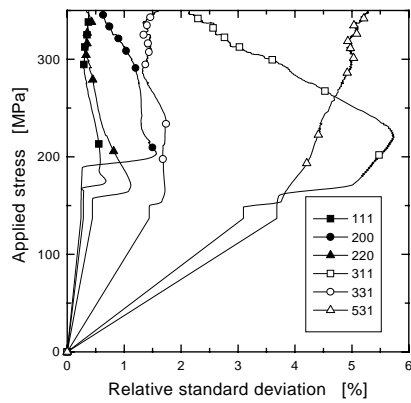
(b) Aluminium, perpendicular to the tensile axis.



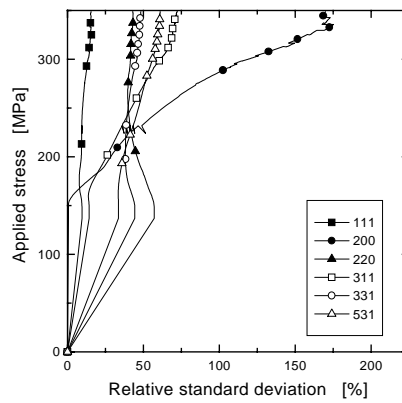
(c) Copper, parallel to the tensile axis.



(d) Copper, perpendicular to the tensile axis.

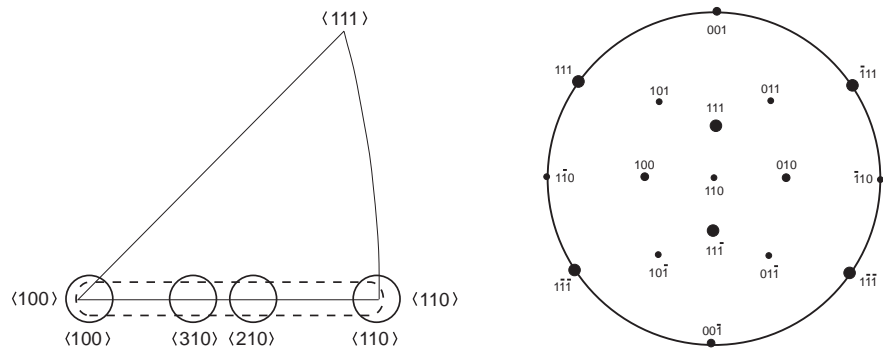


(e) Stainless steel, parallel to the tensile axis.



(f) Stainless steel, perpendicular to the tensile axis.

Figure 3.2. The applied stress versus the relative standard deviation of the elastic lattice strain.



(a) Grain sub-sub-sets within the 200-reflection perpendicular to the tensile axis.

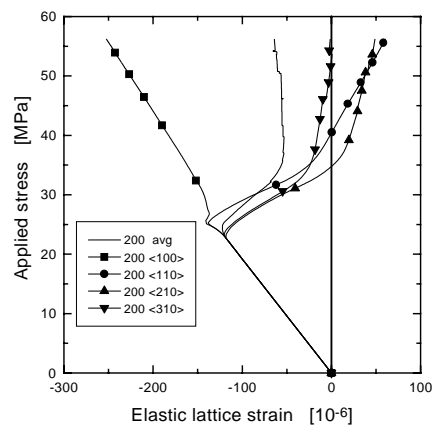
(b) The (110) pole figure for the cubic crystal structure.

Figure 3.3. Grain sub-sub-sets and slip systems for the 200 reflection perpendicular to the tensile axis.

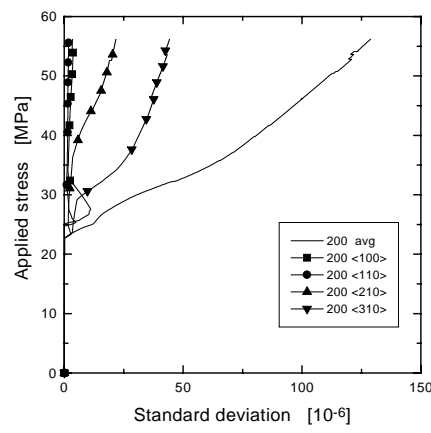
In the area close to the $\langle 110 \rangle$ direction ($200\langle 110 \rangle$ in figure 3.4) the grains have four active slip systems, see figure 2.9, and this combination of four slip systems results in a very asymmetric lateral deformation. For the ideal $\langle 110 \rangle$ the active systems are: $[111](10\bar{1})$, $[111](01\bar{1})$, $[1\bar{1}\bar{1}](101)$ and $[1\bar{1}\bar{1}](101)$, see the $\langle 110 \rangle$ pole figure for the cubic crystal structure in figure 3.3(b). If the grain is subjected to symmetric load and the amount of slip is the same on the four active slip systems, the resulting lateral contraction have a very large component in the $(001) - (00\bar{1})$ direction, the direction perpendicular to the tensile axis, and a very small component in the $(100) - (010)$ direction, see figure 3.3(b). Grains that are oriented close to this specific orientation will have the same asymmetric lateral contraction. This means that the plastic contraction perpendicular to the tensile axis, in the $(001) - (00\bar{1})$ direction, is much larger than the contraction in the continuum matrix, which will introduce a tensile stress in the $(001) - (00\bar{1})$ direction counteracting the Poisson contraction and thereby introduce the dramatic change in the development of the lattice strain for the 200-reflection perpendicular to the tensile axis at the onset of plastic deformation. This behaviour will result in 'curling' which is a well known experimental manifestation of the special behaviour in the direction perpendicular to the tensile (or compression) axis in grains subjected to tension or compression in the $\langle 110 \rangle$ direction, *e.g.* (Hosford 1964).

For the orientations close to the $\langle 210 \rangle$ and $\langle 310 \rangle$ directions ($200\langle 210 \rangle$ and $200\langle 310 \rangle$ in figure 3.4) the grains have mainly two active slip systems, and again these systems results in a deformation mode with a very uneven lateral contraction. Close to the $\langle 100 \rangle$ direction ($200\langle 100 \rangle$ in figure 3.4) the grain have at least six active slip systems, and then the deformation mode is more symmetric.

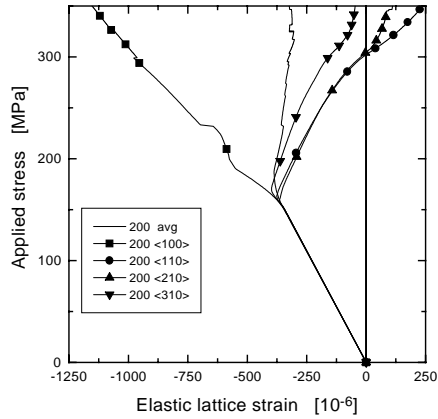
The elastic lattice strain response and the relative standard deviation for the four sub-regions of the 200-reflection, represented by the circles in figure 3.3(a), are shown in figure 3.4 for aluminium and stainless steel. The plots for copper are omitted as they are similar to the ones for stainless steel. As seen in figure 3.4, the stress-strain response of the grain sub-sub-sets are very different in both aluminium and stainless steel. Although the standard deviation for the four grain sub-sub-sets are relatively small, the very different behaviour of the grain within the grain sub-set causes the the standard deviation of the whole 200-reflection to be much larger.



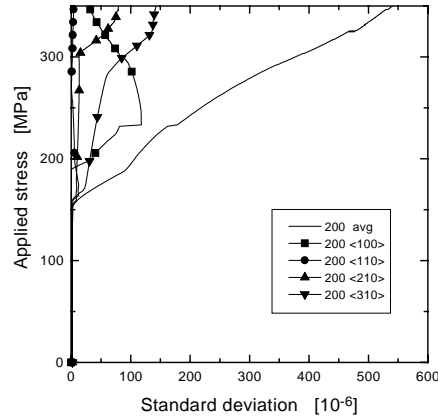
(a) Stress-strain curves for grain sub-sub-sets of the 200-reflection in aluminium.



(b) Standard deviation of the elastic strain for grain sub-sub-sets of the 200-reflection in aluminium.



(c) Stress-strain curves for the grain sub-sub-sets of the 200-reflection in stainless steel.



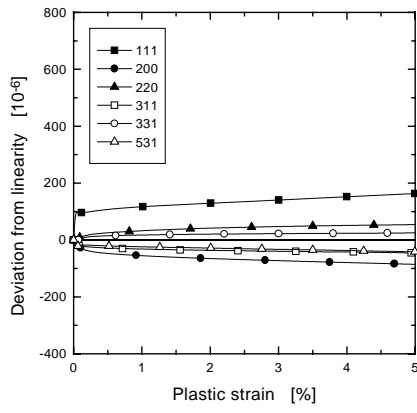
(d) Standard deviation of the elastic strain for grain sub-sub-sets of the 200-reflection in stainless steel.

Figure 3.4. Stress-strain curves and relative standard deviation for the grain sub-sub-sets of the 200-reflection in aluminium and stainless steel.

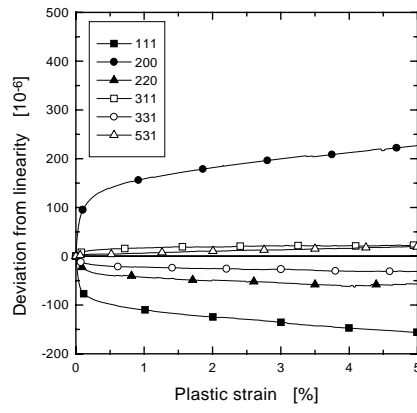
3.2.4 Deviation from Linearity

In section 3.2.2 the elastic lattice strain response of the three materials is investigated, and great differences between the longitudinal and transverse lattice response are observed. The perfect hkl -reflection for technological strain determination would be one that is rather in-sensitive to the deformation history and one that retains a linear response even when exceeding yield. In evaluating this aspect it is chosen to present the results of figure 3.1 in terms of the amount the elastic lattice strain response deviates from the initial elastic behavior, following the Kröner stiffnesses. This deviation is shown in figure 3.5.

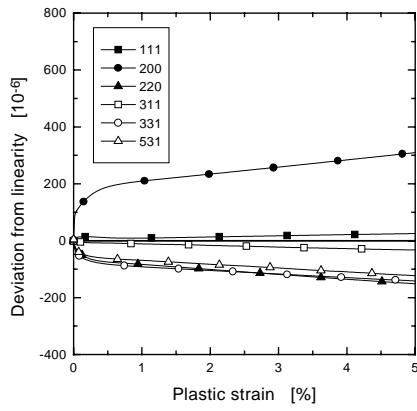
Again, it is observed that the linearity deviation is largest for austenitic stainless steel and smallest for aluminium; note the scale difference in the figures. The linearity deviation for all six reflections are quite similar in copper and austenitic stainless steel. In these two materials, the 200-reflection shows the largest linearity deviation in the plastic region, both parallel and perpendicular to the tensile axis. The 311-reflection shows the smallest linearity deviation, except in stainless steel parallel to the tensile axis, where the 111-reflection is a bit closer to zero. In



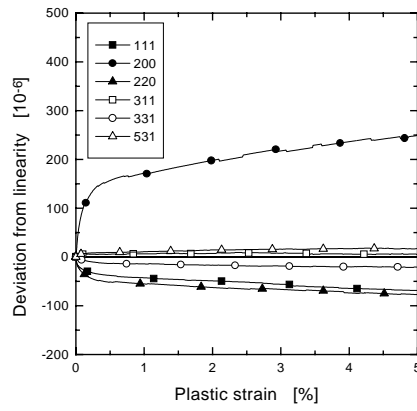
(a) Aluminium, parallel to the tensile axis.



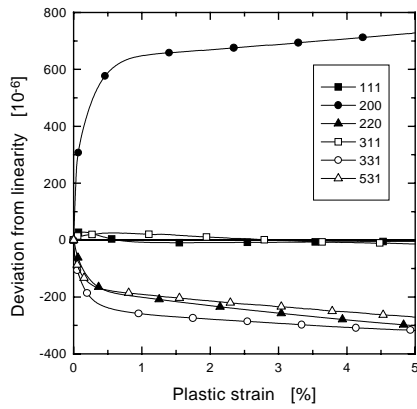
(b) Aluminium, perpendicular to the tensile axis.



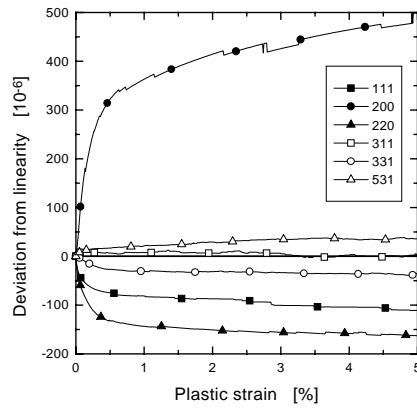
(c) Copper, parallel to the tensile axis.



(d) Copper, perpendicular to the tensile axis.



(e) Stainless steel, parallel to the tensile axis.



(f) Stainless steel, perpendicular to the tensile axis.

Figure 3.5. Elastic strain deviation from linearity as a function of the plastic strain.

aluminium none of the reflections show as large linearity deviation as the 200-reflection in copper and austenitic stainless steel, but still all the reflections show non-linearity in the plastic region. The 111- and 200-reflections show the largest deviation and the 311- and 531-reflections the smallest deviation.

The normal standard deviation in a neutron diffraction measurement is about $\pm 50 \times 10^{-6}$. A suitable reflection for stress and strain measurement would be one that does not deviate more than $\pm 50 \times 10^{-6}$ from linearity. In all three materials, the 311-reflection always has a linearity deviation less than $\pm 50 \times 10^{-6}$ up to 5% equivalent plastic strain for the two directions, and thus the 311-reflection is a quite suitable *hkl*-reflection for neutron diffraction strain measurements in *fcc* materials.

3.2.5 Normalised Stresses

The results reported in section 3.2.2 show the difference in elastic anisotropy, strength and hardening in the three materials. The underlying deformation pattern is illustrated in the figures 3.6(a) to 3.6(c), where the average stress within the reflections, normalised by the overall average stress, is shown as a function of the strain for the three materials. The corresponding plots for the Taylor and the Sachs models are shown in the figures 3.6(d) and 3.6(e), calculated as the average m-factor for the reflections divided by the overall average m-factor.

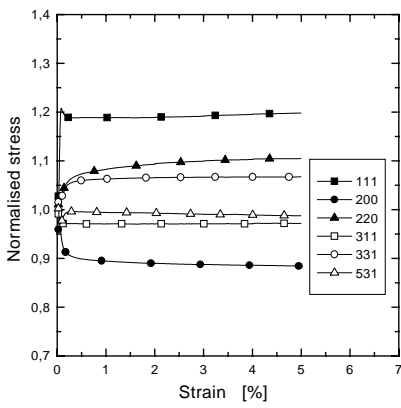
As seen in the figures 3.6(a) to 3.6(c) the normalised stresses for the selected reflections are almost identical in the three materials after only $\sim 0.5\%$ strain. In aluminium, with relatively low elastic anisotropy, there is relatively small differences between the reflections at the on-set of plasticity, and then the normalised stresses spread out in the plastic region. In copper and stainless steel the larger elastic anisotropy causes relatively large differences in the elastic region, but in the plastic region the range of the normalised stresses decreases, and they become very close to the values in aluminium. This behaviour agrees well with the findings in section 2.3 that the deformation pattern is basically the same in aluminium and copper. By comparing with the figures 3.6(d) and 3.6(e) it is seen that the results of the present self-consistent model is about half-way between the Taylor and the Sachs model, as also concluded in section 2.3.

3.2.6 Residual Strain

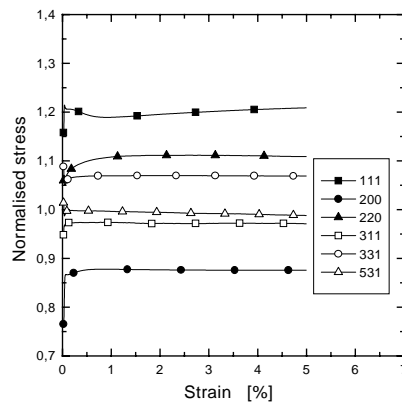
In the sections 3.2.2 to 3.2.4 the non-linear lattice strain response of different *hkl*-reflections under uniaxial loading is presented. Most technological applications of neutron diffraction involve residual lattice strain measurements in unloaded components. A rather perfect internal strain gauge would in this case be an *hkl*-reflection with negligible intergranular lattice strains, where the measured residual lattice strains are dominated by the macroscopic residual stress state, which is the aim of the investigation. Hence, it is of interest to focus on the residual lattice strain development as a function of the plastic deformation. The numerical simulation of these intergranular residual lattice strains upon unloading from different degrees of plastic deformation is presented in figure 3.7 for the range of *hkl*-reflections in question.

As the unloading to zero stress in the model calculations does not activate any slip systems, the unloading is fully elastic, and the calculated residual strains are practically identical to the deviation from linearity. This is shown for aluminium in figure 3.7 for eight unloads (0.25%, 0.5%, 0.75%, 1%, 2%, 3%, 4% and 5% plastic strain).

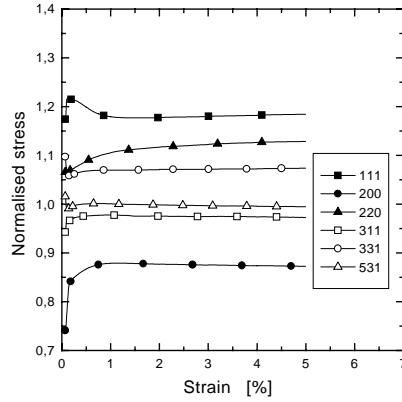
As seen in figure 3.7, the deviation from linearity is practically identical to the residual lattice strain for all the reflections. When no slip systems are active



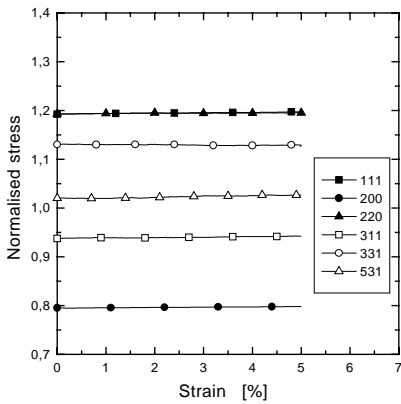
(a) Aluminium.



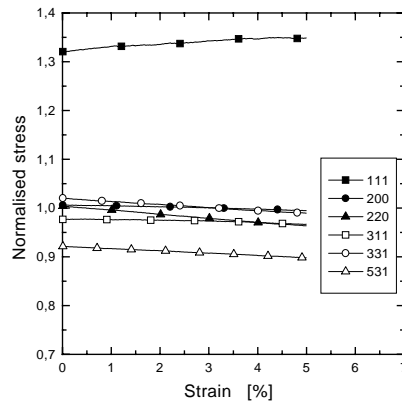
(b) Copper.



(c) Stainless steel.



(d) Taylor model.



(e) Sachs model.

Figure 3.6. The normalised stress as a function of the strain.

during unloading, only the texture development between the unloads can change the residual strains, as a change in the texture will change the Kröner stiffness for the reflections. But at the low degrees of deformation used in the present calculations there is only very little texture development between the unloads. The calculated residual strains in the direction parallel to the tensile axis for the

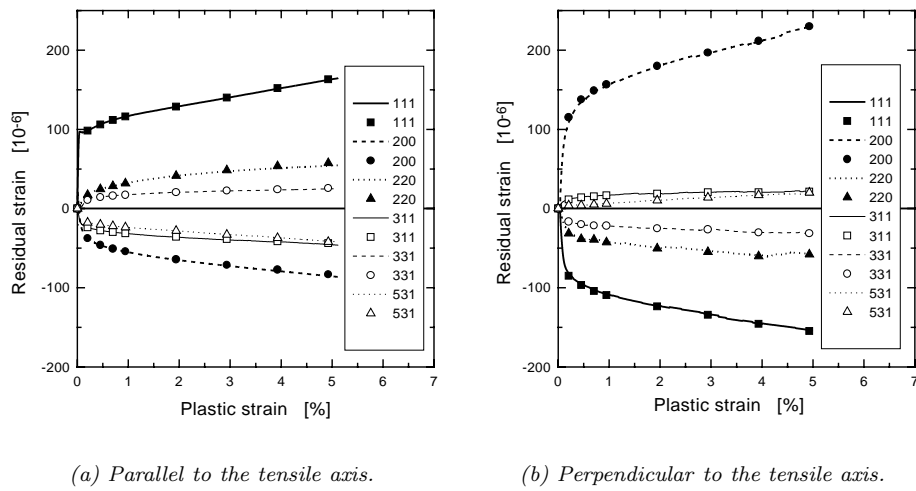


Figure 3.7. Residual strain in aluminium calculated directly (symbols) and derived from the deviation from linearity (lines).

eight unloads are shown in appendix B for the three materials.

3.3 Discussion

To find the best suitable reflections for stress and strain measurements with neutron diffraction, the relation between the applied stress and the elastic lattice strain in the reflections has been investigated. The calculations show that the degree of plastic anisotropy follows the degree of elastic anisotropy for the reflections parallel to the tensile axis, but that the plastic anisotropy for the reflections perpendicular to the tensile axis is of the same size in the three materials.

The elastic strain variation within the reflections is relatively small in the elastic region in both directions in the three materials. In the plastic region the variation increases rapidly, especially in the direction perpendicular to the tensile axis, and the relative standard deviation of the elastic lattice strain are in some cases about 50% (200% for the 200-reflection). The large variations of the elastic strain within the grain sub-sets perpendicular to the tensile axis in the plastic region can be caused by the differences in the elastic and plastic anisotropy as described in section 3.2.3.

The redistribution of the lattice strains perpendicular to the tensile axis at the onset of plastic deformation is particularly dramatic for the 200-reflection. The lattice strain may even decrease with increasing applied stress. As described in section 3.2.3 the sub-set of grains with $\langle 200 \rangle$ perpendicular to the tensile axis is composed of sub-sub-sets of grains with the tensile axis distributed along the $\langle 100 \rangle$ - $\langle 110 \rangle$ side of the unit triangle. A close investigation of the grains in these sub-sub-sets (with the exception of those close to $\langle 100 \rangle$) in terms of the numbers of active slip systems and the m-factors shows that their plastic contraction (perpendicular to the tensile axis) is very uneven. This will, for some of the grains that constitute the 200-reflection perpendicular to the tensile axis, introduce high tensile stresses in the direction perpendicular to the tensile axis counteracting the Poisson contraction. Hence, the development of the lattice strain for the sub-sets of the 200-reflection perpendicular to the tensile axis are very different at the onset of plastic deformation.

As discussed above the special deformation modes are activated as the conditions for each grain is rather symmetric, including the chosen hardening law

which is practically isotropic. Recently, another type of hardening has been proposed by (Bassani 1994), where a diagonal hardening matrix (h_{ii}) is used. This ensures that the hardening matrix is positive definite and that the slip rates are unique (Hill 1966). The components of the proposed hardening matrix are individual functions of the accumulated slip on all the systems. The components are defined as

$$h_{ii} = F(\gamma^i) G(\gamma^j; j = 1, N, j \neq i) \quad (3.1)$$

$F(\gamma^i)$ is a function of the accumulated slip on the slip system under consideration, and $G(\gamma^j; j = 1, N, j \neq i)$ is a function of the ratio of the primary slip and the secondary slip, and the type of dislocation junction the primary slip system and the secondary slip system produces. In this formulation strong latent hardening is replaced by strong increase of hardening *moduli* in latent systems, see (Bassani 1994) for further description.

The 311-reflection shows the smallest linearity deviation, and thereby residual strain, both parallel and perpendicular to the tensile axis in all the materials, as described in section 3.2.4, and thus it is a suitable reflection to use for stress/strain characterisation. The calculations show that the 111, 200 and 220 reflections are deviating from linearity with more than the normal strain resolution in a neutron diffraction measurement, and that the residual lattice strain build-up thereby is relatively high for these reflections. This indicates that if these reflections are used in stress and strain measurements, the non-linearities must be taken into account and the intergranular residual stresses must be separated from those originating from the macroscopical plastic deformation.

4 Neutron Diffraction

Neutron diffraction is widely used in materials science, where a main advantage is to be found in the penetration power of neutrons, allowing bulk measurements to penetrate centimeters into common elements like aluminum, copper or iron. Neutron diffraction applications of primary interest in the present work is determination of lattice strains and the determination of the initial sample texture. The actual texture in the samples are used in the model evaluation in section 5. In this work two different types of neutron diffraction is utilised; fixed wavelength measurements and *time-of-flight* (TOF) measurements. The fixed wavelength method is used at the steady state reactor DR3 at Risø National Laboratory (Denmark), and the TOF method are used at the Manuel Lujan Neutron Scattering Center (MLNSC) at Los Alamos National Laboratory (USA).

In normal overall stress and strain characterisation by neutron diffraction only one reflection is required. The intensity of the monochromated neutron beam at reactor sources used for fixed wavelength measurements is relatively high, and the measurement of a single reflection is relatively fast. The integrated neutron intensity at a pulsed source is much lower than on a reactor and the time scale for a measurement of a single reflection by the TOF method is much larger than for a fixed wavelength measurement. However, the TOF measurement provides information for multiple reflections at the same time as all the neutrons with the appropriate energies contribute to the measured spectrum. If information for many reflections are required at the same time, the time scale for TOF measurements is comparable with fixed wavelength measurements.

4.1 Lattice Strain Determination

The neutron diffraction technique for lattice strain characterisation in crystalline materials is based on Bragg's law given by:

$$\lambda = 2d_{hkl} \sin \theta \quad (4.1)$$

where λ is the neutron wavelength, d_{hkl} is the lattice plane spacing of a selected hkl reflection and θ is half the diffraction angle. A variety of experimental configurations can be used; see for instance (Allen *et al.* 1985, Lorentzen 1990, Bourke *et al.* 1992).

4.1.1 Fixed Wavelength Method

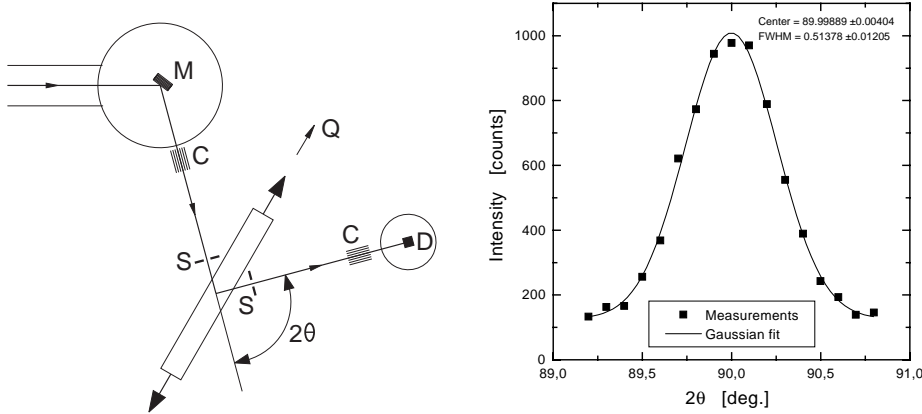
Neutrons with a wide energy spectrum are produced continuously by the fission processes in a thermal nuclear reactor. In a fixed wavelength measurement, the

incident beam is monochromated by inserting a monochromator in the 'white' beam from the reactor. The incident beam is diffracted in the sample and by scanning a single detector over an appropriate angle range the Bragg angle of the specific crystallites sub-set, fulfilling the Bragg relation is determined. This merely involves those crystallites having a specific lattice plane spacing, and their lattice plane normal aligned along the scattering vector, see figure 4.1(a).

The lattice plane spacing, d_{hkl} , is determined from Bragg's law, equation 4.1, and then the elastic lattice strain is determined by relating the measured lattice plane spacing to a stress-free reference value, d_{hkl}^0 , following the relation:

$$\varepsilon_{hkl} = \frac{\Delta d_{hkl}}{d_{hkl}} = \frac{d_{hkl} - d_{hkl}^0}{d_{hkl}^0} = \frac{\sin \theta^0}{\sin \theta} - 1 \quad (4.2)$$

4.1.1.1 Measurements The present experimental work is based on a single detector set-up at the steady state research reactor, DR-3, at Risø National Laboratory (Denmark). The experimental set-up is shown in figure 4.1(a), which indi-



(a) Experimental setup at TAS-8. C: Collimator, D: Detector, M: Monochromator, Q: Scattering vector and S: Slits.

(b) Typical intensity versus 2θ plot from the TAS-8 spectrometer.

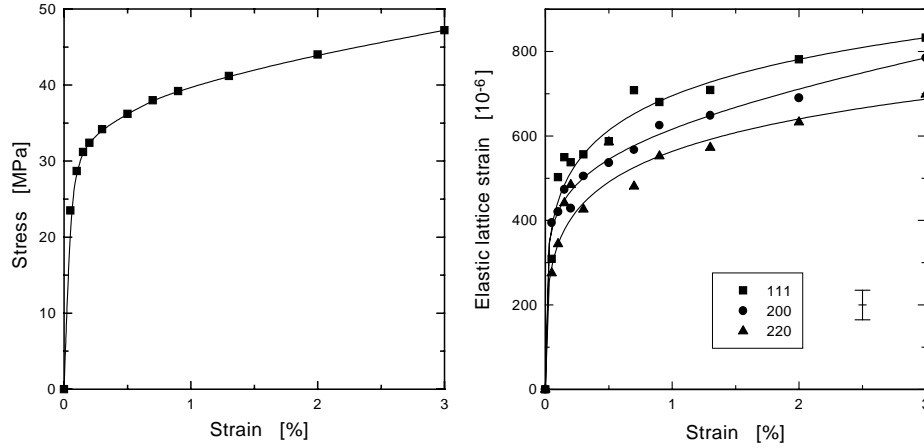
Figure 4.1. The experimental set-up and a typical intensity peak for the TAS-8 spectrometer at Risø National Laboratory (Denmark).

cates that a specific neutron wavelength is selected from the 'white' beam of the reactor using a monochromator (M); in this case a large single crystal of Germanium. Both incident and diffracted beams, that define the scattering vector (Q), are collimated (C), and the gauge volume is defined by slit systems (S) made from a neutron absorbing material; in this case Cadmium. A typical intensity curve is shown in figure 4.1(b).

As an example of a measurement with this technique commercially pure aluminium samples (Al2S) are loaded in uniaxial tension using a stress-rig developed for the spectrometer (Lorentzen and Sørensen 1991). By aligning the tensile axis parallel to the scattering vector, only the lattice strain along this axis is determined. The reference value, d_{hkl}^0 , is here selected as the lattice plane spacing at zero load rather than a true stress-free value.

The neutron diffraction measurements were made at fixed macroscopic strain levels and in the plastic region some room temperature relaxation was noted. For each reflection, measurements on two identical samples were completed, and the results are presented as an average of these two. The average macroscopic stress-strain curve for the tests is shown in figure 4.2(a) and the measured elastic

lattice strains are shown in figure 4.2(b) as a function of the macroscopic strain component in the tension direction. The error bar in figure 4.2(b) represent the sample-to-sample variation as described in appendix A.2.



(a) The macroscopic stress-strain response. The symbols indicate the diffraction measurements.

(b) The measured elastic lattice strain as a function of the applied strain.

Figure 4.2. The measured macroscopic stress-strain response and the elastic lattice strain response for aluminium. The lines are meant as a 'guide to the eye'.

It is evident that the reflections display differences in the measured lattice strains, with the 111-reflection displaying the highest lattice strains, while the 220-reflection is displaying the smallest lattice strains. Furthermore it is observed that the general trend in all three curves resemble the macroscopic stress-strain curve as shown in figure 4.2(a).

The results of the experiments will be compared with the predictions of the present self-consistent polycrystal deformation model in section 5.2.1.

4.1.2 Time-of-flight Method

In a *time-of-flight* (TOF) measurement, a target of a heavy element is bombarded by proton pulses accelerated to large energies and thereby nuclei in the target emits pulses of neutrons produced by a process called spallation which occurs when the energetic protons interact with the target. As the neutrons are created when the proton pulse interacts with the target the wavelength of the neutrons can be determined from the time difference between the creation and the detection, and the distance to the detector. Contrary to the fixed wavelength method, the incident beam is the 'white' beam directly from the target, and each neutron pulse contains a continuous spectrum of energies with a spectrum determined by the moderator. The diffracted intensity from the samples are measured and the wavelengths are determined from the *time-of-flight*. The geometry of the setup then determines the scattering vector and the TOF, t is determining the wavelength of the neutrons.

$$t = \frac{L}{v} = \frac{\lambda m}{h} L \quad (4.3)$$

where L is the path length, v and m are the velocity and the mass of the neutron, λ is the wavelength and h is Planck's constant. Multiple detectors can be used to determine elastic lattice strains in different directions at the same time. The

elastic lattice strain is determined from the TOF as

$$\varepsilon_{hkl} = \frac{\Delta d}{d} = \frac{\Delta \lambda}{\lambda} = \frac{\Delta t}{t} \quad (4.4)$$

4.1.2.1 Measurements The present experimental work is based on the NPD instrument at MLNSC (USA), using the stress-rig developed for the instrument (Bourke *et al.* 1993). A schematic set-up of the NPD instrument is shown in

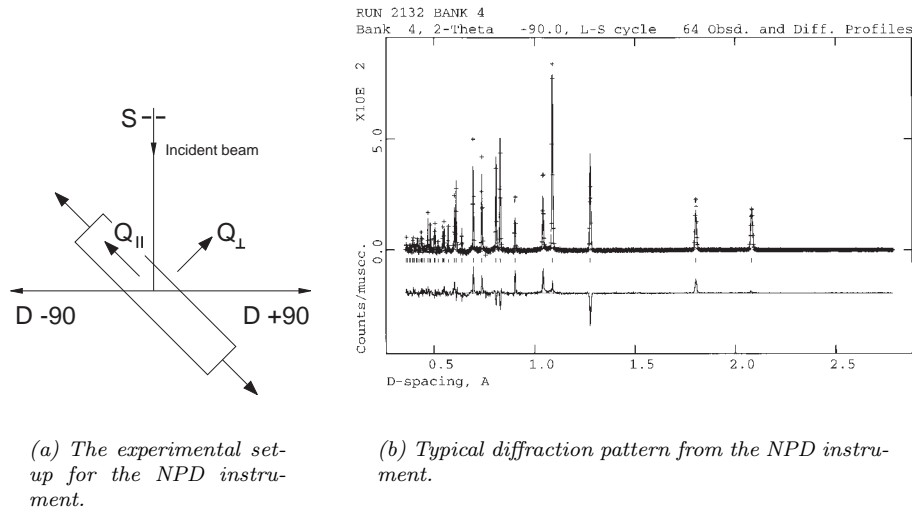
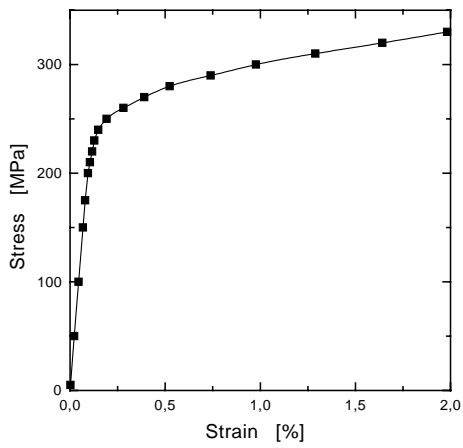


Figure 4.3. The experimental set-up and a typical diffraction pattern for the NPD instrument at MLNSC.

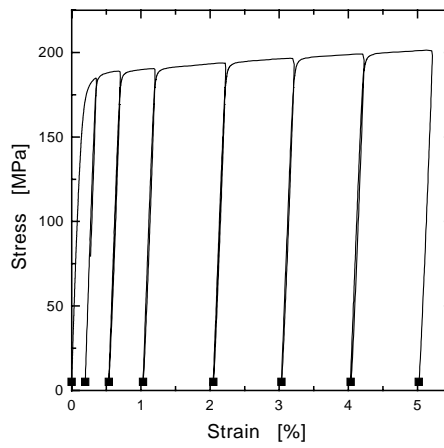
figure 4.3(a) and a typical measured diffraction pattern is shown in figure 4.3(b). The incident beam (defined by slits, S) is 10 mm wide. No collimation is used on either incident or diffracted beam, and there is not used slits to define the diffracted beam. The NPD sample chamber is located 32 meters from the target and the moderator is chilled water (10° C). The elastic lattice strain components parallel and perpendicular to the tensile axis are determined for 15 *hkl*-reflections at the same time by the detector banks at plus and minus 90°. Due to the size of the detector banks the angular resolution is about $\pm 5.5^\circ$. Only the results for the six reflections used in section 2.3 is quoted to reduce the amount of data in the illustrations.

Samples of austenitic stainless steel and copper were used in the experiments, and both *in-situ* strains and residual strains were measured at various load levels. The macroscopical stress-strain response for stainless steel is shown in figure 4.4(a) where the *in-situ* diffraction measurements are represented by the symbols. The macroscopical stress-strain response for copper is shown in figure 4.4(b) where the residual strain measurements are represented by the symbols. The strain resolution of the TOF measurements is approximately 50×10^{-6} (Bourke *et al.* 1992) depending on the reflection.

The samples were cut from rolled sheets and unfortunately the copper samples were not fully recrystallised after manufacture, and as a result the overall stress strain response show a very sharp corner at yield and a very low and almost linear hardening in the plastic region, see figure 4.4(b). The residual strains were measured for the unloads shown in figure 4.4(b), but the *in-situ* measurements are limited to the elastic region and the transition zone as the sample started to creep during the neutron diffraction measurement at loads in the plastic region.



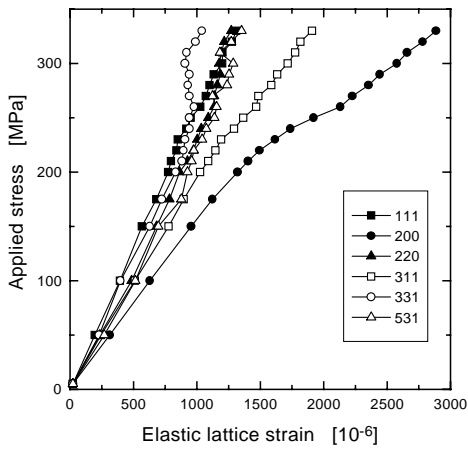
(a) Stainless steel. The line is meant as a 'guide to the eye'.



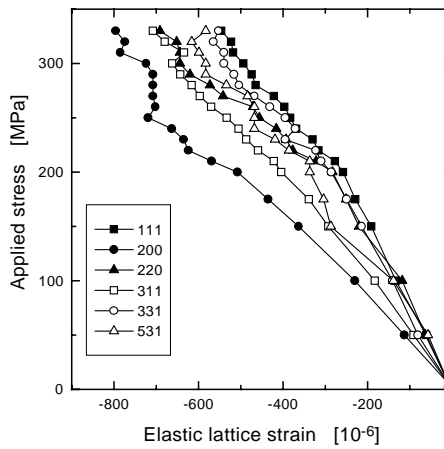
(b) Copper.

Figure 4.4. The macroscopic stress-strain response for stainless steel and copper. The symbols indicate a diffraction measurement.

Austenitic stainless steel The elastic lattice strains in *in-situ* uniaxial tension tests of austenitic stainless steel have been measured for reflections parallel and perpendicular to the tensile axis. The diffraction measurements were made at selected stress levels and the applied stress component in the tensile direction is shown versus the measured elastic lattice strains in figure 4.5.



(a) Parallel to the tensile axis.



(b) Perpendicular to the tensile axis.

Figure 4.5. The applied stress versus the measured elastic lattice strain for stainless steel.

The results of the measurements on stainless steel and copper, that both have a high anisotropy, is plotted as applied stress versus measured elastic lattice strain to approach the presentation in a conventional stress-strain curve. This way of plotting the data was not used for the measurements on aluminium as the anisotropy is relatively small and the difference between the reflections are difficult to observe in this type of plots.

As seen in figure 4.5(a) the reflections parallel to the tensile axis are subjected to different elastic strain in the elastic regime due to the elastic anisotropy. The 331-

reflection reaches yield first and starts to bend upwards as it can not be strained further elastically. As a result of this, the other grains must carry a larger part of the load, which is best seen for the 200-reflection as it is the weakest reflection. The 200-reflection starts to bend downwards as it is subjected to higher load. When the 200-reflection itself becomes plastic, it starts to bend upwards again as it can not be strained further elastically, and when all the reflection, and the polycrystal itself, has become fully plastic, the elastic strain response becomes almost linear again, but with different moduli than in the elastic region. Then the strains are dictated by the plastic anisotropy of the material. The 'double bend' behavior is not so obvious for the other reflection as they are relative stiff.

Perpendicular to the tensile axis, figure 4.5(b), the rearranging of load in the transition zone is not so pronounced, but it is obvious that the modulus of the reflections change in the plastic region.

In addition to the *in-situ* diffraction measurements, the residual lattice strains were measured at selected plastic strain levels (0.2%, 0.7%, 1.2% and 2.0%) and the results are shown in figure 4.6. As seen in figure 4.6, the residual strains

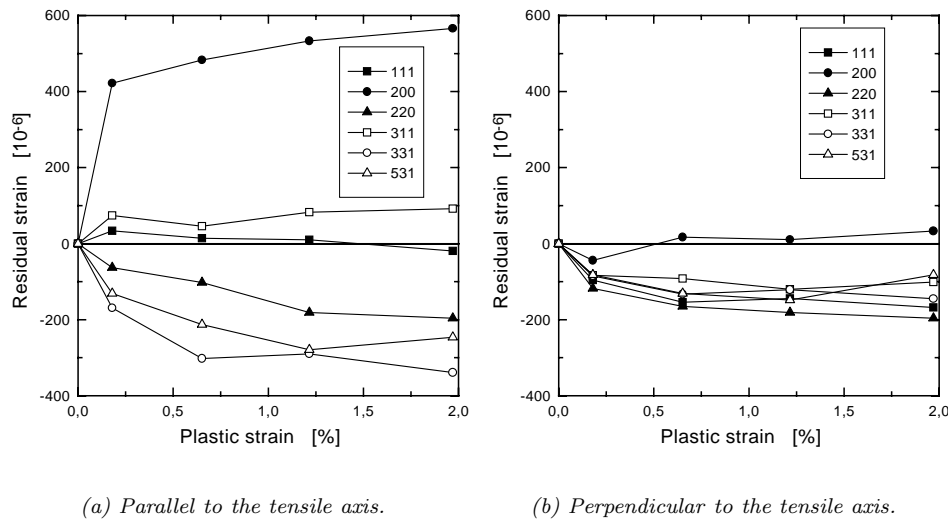


Figure 4.6. The residual lattice strain of the reflections as a function of the equivalent plastic strain for stainless steel.

build up in the transition zone and becomes almost constant in the fully plastic region. This also indicates that the rearranging of the load is restricted to the transition zone, which is in agreement with the 'double bend' elastic strain curves found in the *in-situ* measurements. Parallel to the tensile axis, figure 4.6(a), the 200-reflection shows the highest positive residual strain and the 331-reflection the highest negative residual strain. Perpendicular to the tensile axis, figure 4.6(b), most of the reflections are in compression and only the 200-reflection is slightly in tension. Due to equilibrium conditions the overall average stress in the sample must be zero, but this do not mean that the average of a single *strain* component in one direction must be averaged to zero. The level of the residual strains are not much larger than the normal strain resolution of a neutron diffraction measurement ($\pm 50 \times 10^{-6}$).

Copper The elastic lattice strains in *in-situ* uniaxial tension tests have also been measured for pure copper (99.999%) using reflections parallel and perpendicular to the tensile axis, see figure 4.7.

In figure 4.7 the relatively strong elastic anisotropy of copper are shown by

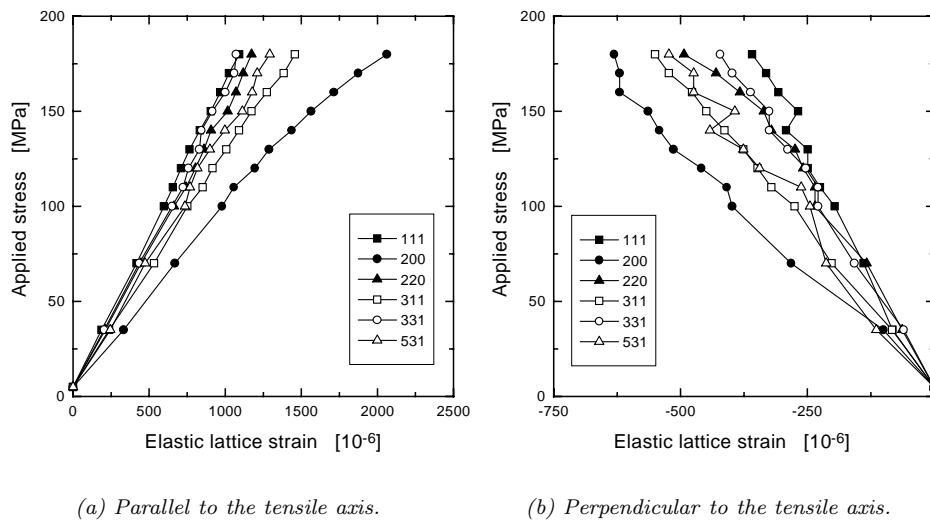


Figure 4.7. The applied stress versus the measured elastic lattice strain for copper.

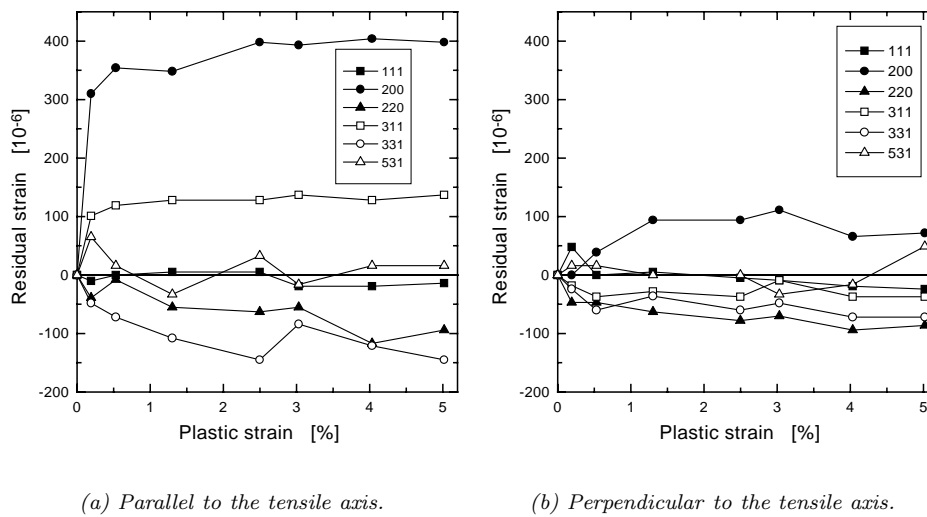


Figure 4.8. The residual lattice strain of the reflections as a function of the plastic strain for copper.

the difference in modulus for the different reflections. The 200-reflection is the weakest and the 111-reflection is the strongest. In the transition zone the 200-reflection starts to bend downwards as for the stainless steel, but the 'double bend' behavior is not observed as the measurements are restricted to the elastic regime and the transition zone.

Perpendicular to the tension axis, figure 4.7, the 200-reflection is again the softer and the 111-reflection is the strongest. The relative scatter in the measurements is larger than for the measurements parallel to the tensile axis due to the Poisson ratio and due to the differences in the grains that constitutes the reflections, as discussed in section 3.2.3.

The residual lattice strains in copper were measured at selected plastic strain levels (0.2%, 0.5%, 1.0%, 2.0%, 3.0%, 4.0% and 5.0%). The results are shown in figure 4.8. The residual strains in copper resembles the ones measured in stainless steel. Parallel to the tension axis, figure 4.8(a), the 200-reflection show the highest positive residual strain and the 331 the highest negative residual strain. Note the

scale difference in figure 4.6 and figure 4.8. Perpendicular to the tensile axis, the 200-reflection is in tension and most of the other reflections are in compression as also observed in stainless steel.

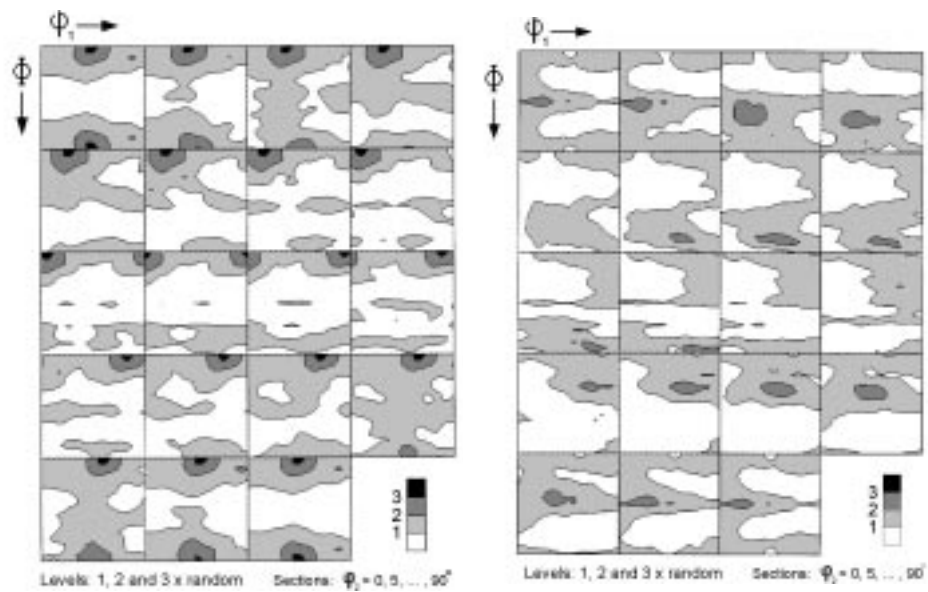
The results of the experiments with copper and stainless steel samples will be compared to the predictions of the present self-consistent polycrystal deformation model in section 5.2.

4.2 Texture Measurement

The numerical calculations presented in the model evaluation, section 5.2, are made with a set of ~ 5700 grains representing the experimentally determined texture of the materials. The initial grain orientations are determined from the measured orientation distribution function (ODF) for the actual samples using the procedure described in (Leffers and Juul Jensen 1986).

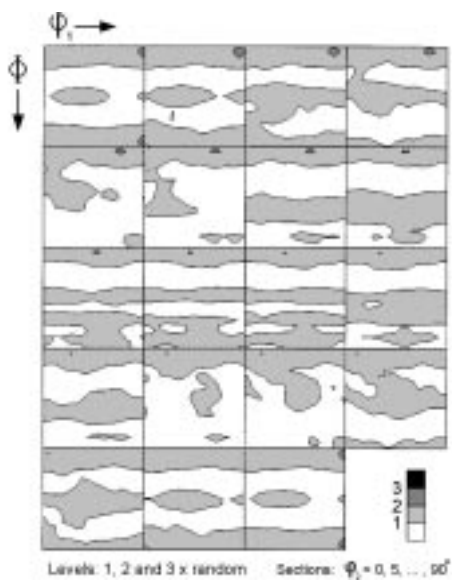
Texture characterisation is also based on Bragg scattering, although the spectrometer set-up differs from the ones used in lattice strain determination, see (Juul Jensen and Leffers 1989, Von Dreele 1997). Using the fixed wavelength technique the ODF is determined by recording the intensity distribution of three hkl -reflections over an appropriate part of Euler space. If the TOF technique is used, all the reflections in the spectra are used in the calculation of the ODF. The orientation distribution function determined for the materials considered here are shown in figure 4.9.

All the uniaxial tension test samples are cut from rolled sheets with the tension axis in the rolling direction. The ODF for the aluminium samples shows that the material has a weak shear texture from the cold rolling during the sample preparation, see figure 4.9(a). The highest level in the ODF plot is three times random. To get an acceptably small grain size for the neutron diffraction measurements, the aluminium was cold rolled and heat treated to obtain a grain size of $\sim 100\mu\text{m}$. The ODF for copper show that the samples have a very weak cube texture, figure 4.9(b), where the highest level in the plot is two times random. The grain size in the copper samples is $\sim 81\mu\text{m}$, but the size distribution is very broad due to the fact that the samples were not fully recrystallised. The stainless steel sheet is almost texture free as seen in figure 4.9(c). The highest level in the plot is two times random. The grain size in the stainless steel samples is $\sim 28\mu\text{m}$.



(a) ODF for the aluminium samples.

(b) ODF for the copper samples.



(c) ODF for the stainless steel samples.

Figure 4.9. Orientation distribution functions for the aluminium, copper and stainless steel samples.

5 Model Evaluation

The uniaxial behavior of aluminium, copper and stainless steel polycrystals is simulated using the three models described in section 2 and the results are evaluated by neutron diffraction.

Polycrystal models are typically evaluated by their capability to simulate texture development. For large deformations and strong textures, model predictions are readily compared to textures determined experimentally *i.e.* by neutron diffraction, as shown in (Juul Jensen and Leffers 1989). In the case of small deformations, however, the texture development is minimal and cannot serve as a means of evaluating the model predictions. However, the model can be evaluated on a much more specific micro-mechanical level using the novel technique of lattice strain characterisation by neutron diffraction. Neutron diffraction provides a possibility of *in-situ* determining the elastic lattice strain in selected grain sub-sets within the polycrystal, as a function of the applied load. For the Taylor and Sachs models the calculated stress components must be converted to 'elastic' strain components as the models are rigid plastic. For the self-consistent model, the measured elastic lattice strain components can be directly compared to model predictions of volume average of elastic lattice strain in selected grain sub-sets resembling the family of grains participating in the particular diffraction experiments.

In all three models, the exponentially decreasing hardening law, described in section 2.3, is used:

$$h_\gamma = h_{final} \left(1 + (h_{ratio} - 1) e^{(-h_{exp} \gamma^{acc})} \right) \quad (5.1)$$

where h_{final} is the final hardening coefficient, h_{ratio} is the ratio between the initial and the final hardening coefficient and h_{exp} is a parameter that determines the strength of the exponential part. This definition of the hardening law also includes the simple linear hardening that is obtained by choosing $h_{ratio} = 1$. Selecting τ_0 and the hardening law, and thus the hardening coefficients, is not trivial. In the present calculations these parameters have been used to fit the macroscopic response of the models to the measured macroscopic stress-strain curves. Thereby it is possible to compare the measured and calculated polycrystal behaviour on a micro-structural scale.

5.1 Taylor and Sachs Models

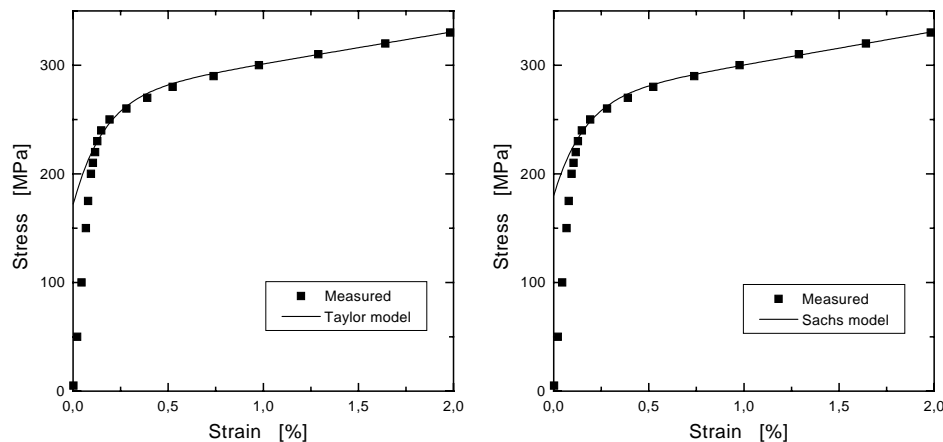
The experimental results for the stainless steel sample, discussed in section 4.1.2, are used to evaluate the Taylor and Sachs models. To be able to compare the results of the models with the measured elastic lattice strains, the calculated

stresses for the grain sub-sets are divided by the Kröner stiffnesses (diffraction elastic constants) for the stainless steel reflections, determined in section 3.2.1. The exponentially decreasing hardening law is used for both models, and the used

	τ_0 MPa	q —	h_{final} MPa	h_{ratio} —	h_{exp} —
Taylor	87.0	1.0	470.0	19.0	275.0
Sachs	87.0	1.0	600.0	19.0	200.0

Table 5.1. Fitting parameters used in the Taylor and Sachs models.

parameters are shown in table 5.1. The macroscopic stress-strain curves are shown in figure 5.1.



(a) Taylor model.

(b) Sachs model.

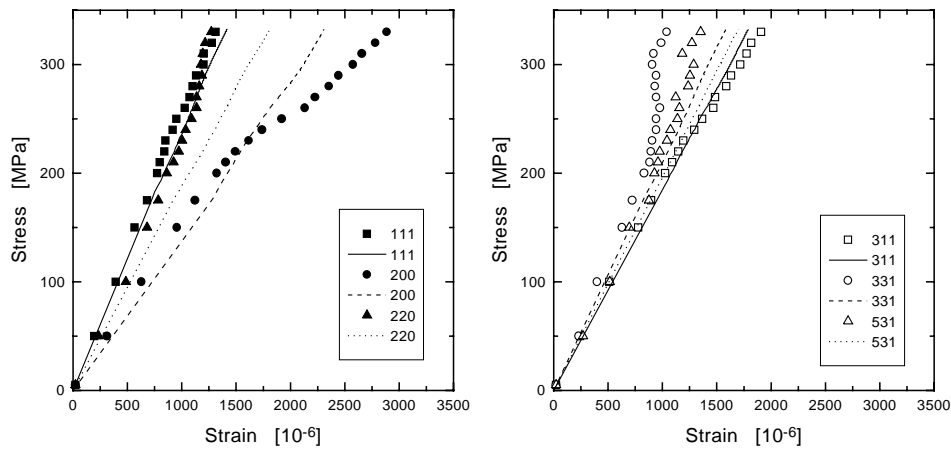
Figure 5.1. Macroscopic stress-strain curves for the Taylor and Sachs models.

As seen in figure 5.1, the two models do not have an elastic region, and in both models the initial critical resolved shear stress value have been selected as half of the apparent yield strength of the material, found from the measured stress-strain curve.

The results of the Taylor model calculations are compared with the measured elastic lattice strain in the reflections parallel to the tensile axis in figure 5.2. The initial 'elastic' part of the model calculations are determined by the Kröner stiffnesses. The model calculation are almost linear for all reflections, which is not the case for the measured data. The observed load redistribution in the measured data in the elastic-plastic transition zone is not incorporated in the rigid plastic Taylor model.

The results of the Sachs model calculations are compared with the measured data in figure 5.3. As for the Taylor model, the initial 'elastic' part of the model calculations are determined by the Kröner stiffnesses. As seen in figure 5.3(b), at least the 111-reflection show significant non-linearity, but most of the reflections are almost linear, as for the Taylor model.

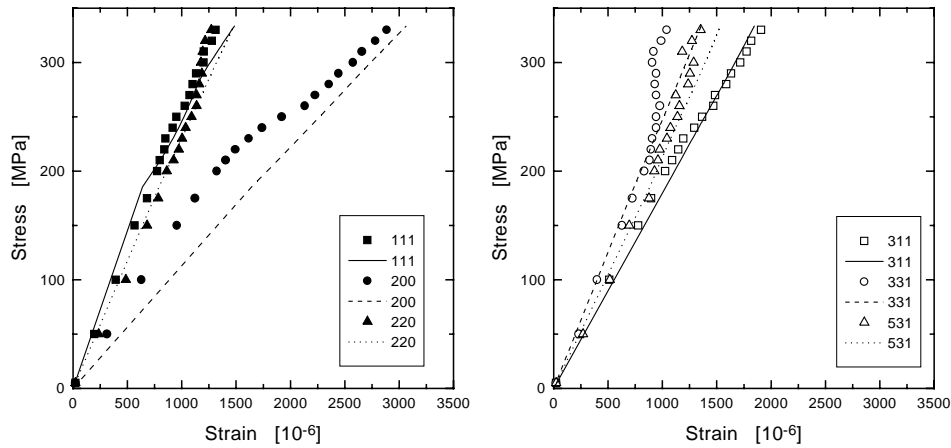
The predictions of the two rigid plastic models are mostly used for large deformations. As seen in figure 5.1, the overall stress strain response of both models are



(a) Symbols are measured data and lines are model calculations.

(b) Symbols are measured data and lines are model calculations.

Figure 5.2. Comparison of the Taylor model results and the measured elastic lattice strain parallel to the tensile axis.



(a) Symbols are measured data and lines are model calculations.

(b) Symbols are measured data and lines are model calculations.

Figure 5.3. Comparison of the Sachs model results and the measured elastic lattice strain parallel to the tensile axis.

relatively close to the measured data above ~ 250 MPa, corresponding to $\sim 0.25\%$ deformation. Comparing the model calculations for loads larger than ~ 250 MPa, it is clear that the Sachs model predictions are closest to the measured data, as the Taylor predictions for the 200- and 220-reflections are rather different than the experimental results.

5.2 Self-consistent Model

In the present section the results of the elastic-plastic self-consistent polycrystal deformation model described in section 2.3 are compared with neutron diffraction measurements in three different materials, aluminium, copper and austenitic stainless steel. The hardening parameters used in the calculations are shown in table 5.2 and the macroscopic stress-strain response for all three materials are

shown in figure 5.4.

	τ_0 MPa	q —	h_{final} MPa	h_{ratio} —	h_{exp} —
Aluminium	10.9	1.01	40.0	5.0	61.0
Aluminium	12.7	1.01	50.0	1.0	1.0
Copper	50.0	1.01	20.0	900	1250
Steel	87.0	1.01	300	5.0	120

Table 5.2. Fitting parameters for the present calculations.

As seen in table 5.2 and in figure 5.4, both the linear hardening law and the exponentially decreasing hardening law have been used in the aluminium calculations to pinpoint the differences in the two assumptions. In the stainless steel and copper calculations only the exponentially decreasing hardening law have been used. The copper samples were unintentionally not fully recrystallised, and therefore show a very sharp transition from elasticity to plasticity. Hence, both h_{ratio} and h_{exp} are relatively high. This behavior also limited the *in-situ* diffraction measurements to the initial elastic regime and transition zone as the sample crept during the diffraction measurements in the plastic regime. As discussed in section 4.2 the initial texture in the samples has been measured. In the calculations the measured texture is represented by grain sets of approximately 5700 grains.

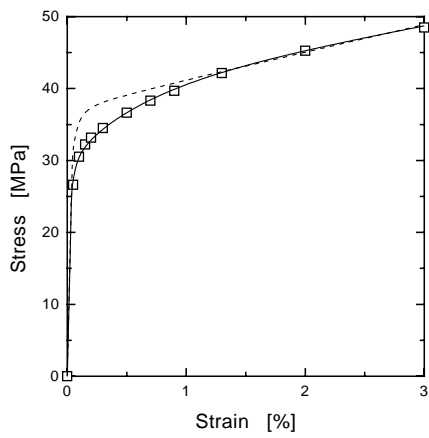
Even though the macroscopic model predictions can predict the experiments macroscopically, this does not provide verification of the model at a microstructural level, *i.e.* whether stresses and strains in the grains are handled appropriately. As described in section 2.1.2, the average elastic strain of selected grain sub-sets representing the reflections in a neutron diffraction measurement are determined in the model calculations. The elastic strain rate components are calculated as $\dot{\epsilon}_c^E = \mathcal{M}_c \dot{\sigma}_c$ and these results form the basis of the model evaluation by comparison with the experimentally determined elastic lattice strain response.

For this comparison only the grain sub-sets fulfilling the Bragg condition should be considered. In the fixed wavelength measurements the experimental resolution of the spectrometer is about 0.5° . However, in a set of ~ 5700 grains, as used in the present calculations, this would correspond to very few grains, and the deduced elastic strains would be prone to poor statistics. In practice, an average is taken over the grains with the specific lattice plane normal within $\pm 5^\circ$ of the main direction. This angular resolution is very much like the $\pm 5.5^\circ$ for the NPD instrument used in the TOF measurements.

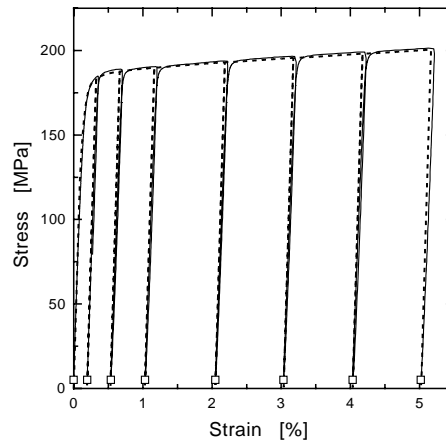
5.2.1 Aluminium

The *in-situ* neutron diffraction measurements on aluminium were made with the TAS-8 spectrometer at Risø National Laboratory (Denmark). Samples were loaded to specific strain levels while focusing on the 111-, 200- and the 220-reflections. For each reflection, measurements were made on two identical samples, and the results are presented as an average of these two. The model prediction of the macroscopic stress-strain response for aluminium calculated with the linear hardening law deviates from the experimental observed stress-strain curve by showing a too sharp curvature at the on-set of yield, as seen in figure 5.4(a). The exponential decreasing hardening law, however, can fit the macroscopic stress-strain curve with an acceptable accuracy.

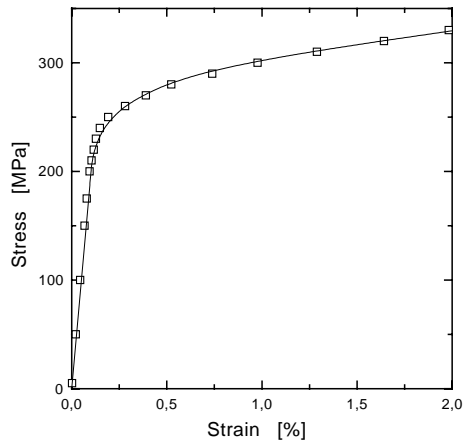
The experimental results of figure 4.2 are compared with the model predictions



(a) Aluminium. Symbols are measured data, (—) are calculated with exponential hardening law and (---) are calculated with linear hardening law.



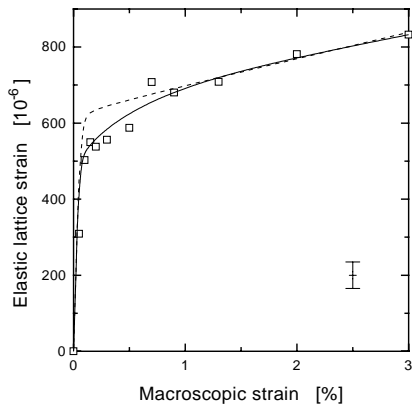
(b) Copper. Symbols represent a diffraction measurements, (—) are the measured stress-strain response and (---) are calculated with exponential hardening law.



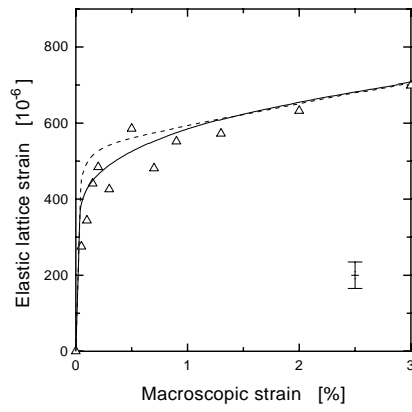
(c) Stainless steel. Symbols are measured data and (—) are calculated with exponential hardening law.

Figure 5.4. Macroscopic stress-strain curves for all the materials.

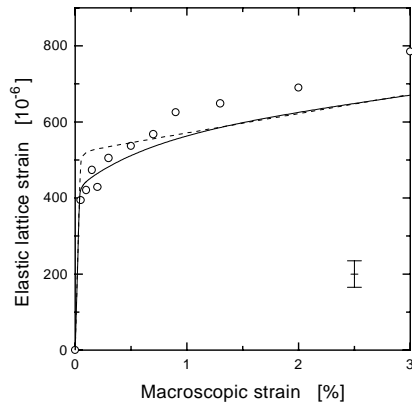
using either of the two selected hardening laws in figure 5.5. It is evident from these results, that the exponential hardening law, which provides a good agreement with the macroscopic stress-strain curve, also provides the closest agreement with experimental observations on a grain size scale. For all three reflections the experimental data show a smooth transition from the elastic region to the essentially linear plastic region. None of the measurements follow the relatively sharp transition predicted when using the linear hardening law, and hence it is concluded from the present data that the linear hardening law is a rather poor choice. Comparing the model predictions and the individual lattice strain responses observations, it is evident that the model predicts the elastic strains evolution for the 111- and the 220-reflection fairly accurately. For the 200-reflection, however, the discrepancy is noticeable. For this reflection, all experimental results past the onset of yielding show higher elastic strains than predicted by the model, and at 1% total deforma-



(a) Elastic lattice strain curve for the 111-reflection.



(b) Elastic lattice strain curve for the 220-reflection.



(c) Elastic lattice strain curve for the 200-reflection.

Figure 5.5. Comparison of neutron diffraction measurements and model calculations for aluminium. Symbols are measured data, (—) are calculated with exponential hardening and (---) are calculated with linear hardening.

tion the model is underestimating the elastic strain level by approximately 20%. In comparing the results from all three grain sub-sets it is furthermore noticed, that the model predicts the 200-reflection to experience numerically lower elastic strains than the 220-reflection. This is in contradiction to the experimental observations, see the figures 4.2(b) and 5.5. On the other hand, the model successfully predicts the numerical level of elastic strains in the 111- and 220-reflections.

5.2.2 Stainless Steel

The neutron diffraction measurements on stainless steel were made with the NPD instrument at MLNSC (USA), and using the TOF technique all the reflections were measured for one sample at the same time. The steel sample were loaded to specific stress levels as the *in-situ* diffraction measurements were made, see figure 4.4(a). The measured *in-situ* data from figure 4.5 is compared with the predictions of the present self-consistent model in figure 5.6.

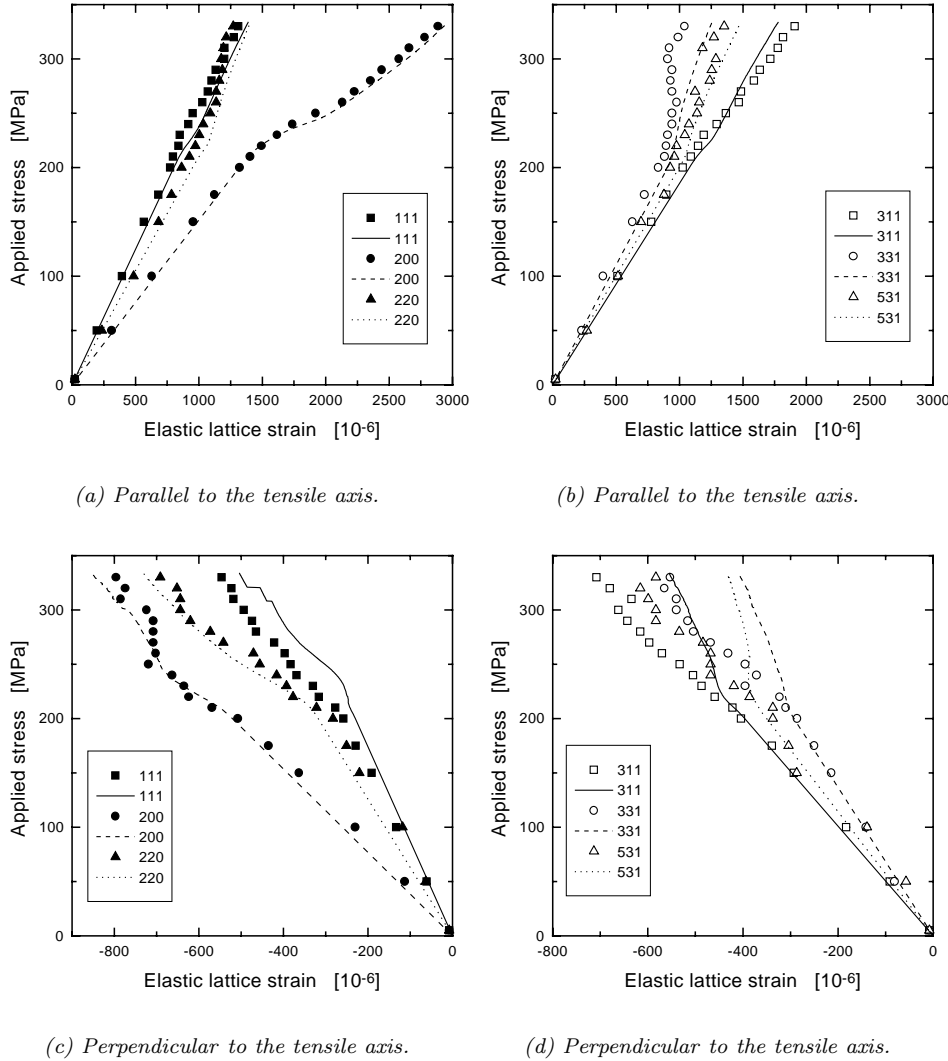
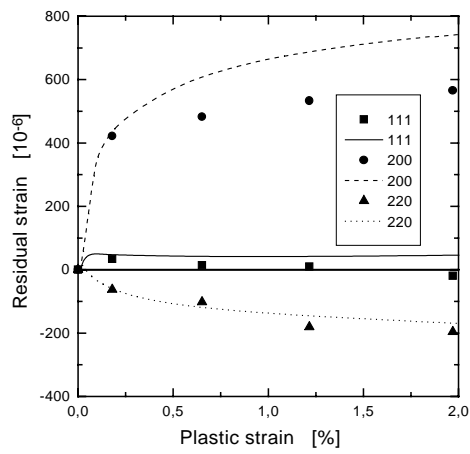


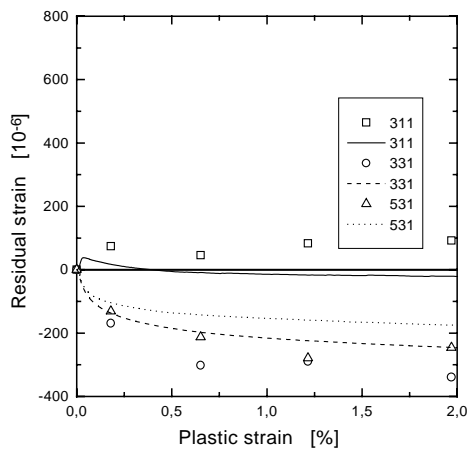
Figure 5.6. The applied stress versus the measured elastic lattice strain for stainless steel.

As seen in figure 5.6, the model accurately predicts the 'double bend' of the 200-reflection described in section 4.1.2, and the predictions for the other reflections parallel to the tensile axis are also very accurate, except for the 331-reflection that show some discrepancies for stress levels above 250 MPa.

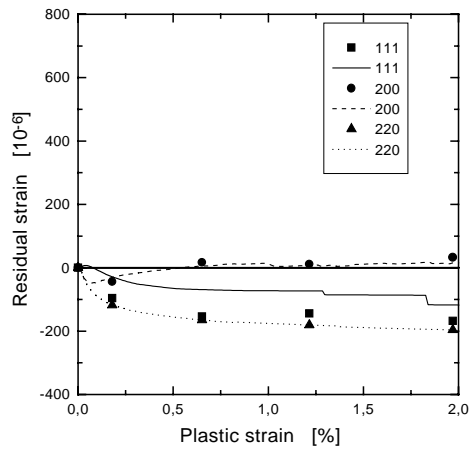
Perpendicular to the tensile axis the model predictions of the 111-, 200- and 220-reflections are also very accurate, figure 5.6(c), but the predictions for 311-, 331- and 531-reflections deviates from the measured data in the plastic region, where the calculations generally show a smaller elastic lattice strain than the measurements, at a given stress level.



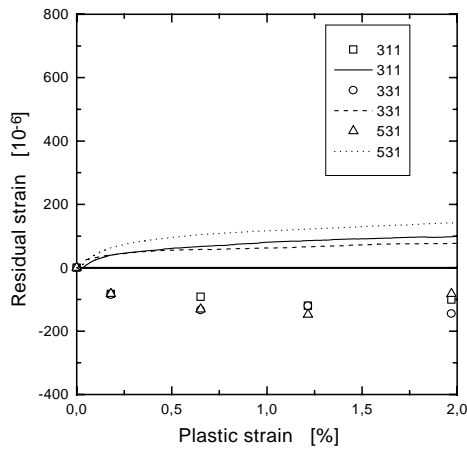
(a) Parallel to the tensile axis.



(b) Parallel to the tensile axis.



(c) Perpendicular to the tensile axis.



(d) Perpendicular to the tensile axis.

Figure 5.7. The residual lattice strain of the reflections as a function of the plastic strain for stainless steel.

It is interesting to note, that the surprising behaviour of the 200-reflection perpendicular to the tension axis described in section 3 does not occur when a non-random texture is used in the calculations. In this case the overall stiffness tensor, and thereby the continuum matrix in the calculations, is no longer transverse isotropic, which supports the earlier explanation of the behaviour in the transversely isotropic case (see section 3.2.3). The changed symmetry has changed the sets of active slip systems in the grains, and the unrealistic deformation modes are not utilised.

Generally, the elastic modulus of the reflections are very accurately predicted by the model, which indicates that the Kröner stiffnesses are good approximations for the diffraction elastic constants.

The residual lattice strains have been measured in the stainless steel sample at four unloads, 0.2%, 0.7%, 1.2% and 2% plastic deformation, and the results are compared with model calculations in figure 5.7 for the reflections parallel and perpendicular to the tensile axis. The predicted residual strains are determined from the deviations from linearity as discussed in section 3.

As seen in figure 5.7 the model predictions of the residual strains parallel to the

tensile axis is fairly accurate, with the 200-reflection showing the poorest fit to the measured data. Perpendicular to the tensile axis, the predictions for the 111-, 200- and 220-reflections are again fairly accurate, but the other three reflections (311, 331 and 531) are all predicted to be slightly in tension, but the measurements show that they are all slightly in compression. As seen in figure 5.6(d) the predictions of *in-situ* strains for these three reflections also show very poor comparison with the measured data in the plastic regime.

5.2.3 Copper

The neutron diffraction measurements in copper were likewise made with the NPD instrument at MLNSC (USA). The copper sample was loaded to specific stress levels in the elastic regime as the *in-situ* diffraction measurements were made, and the residual strain were measured at the seven unloads shown in figure 5.4(b). The measured *in-situ* data from figure 4.7 is compared with the predictions of the present self-consistent model in figure 5.8.

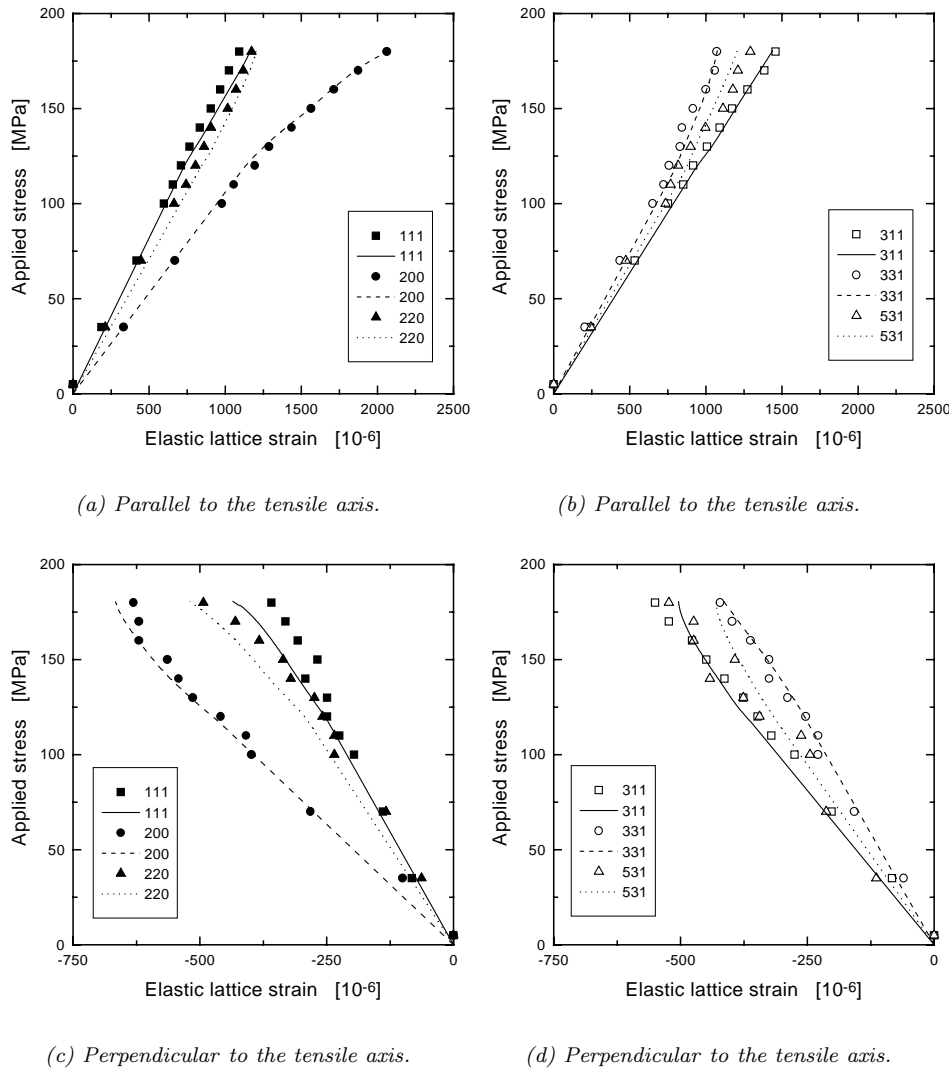


Figure 5.8. The applied stress as a function of the measured elastic lattice strain for copper.

As seen in the figures 5.8(a) and 5.8(b) the model predictions are very accurate

for all the reflections parallel to the tensile axis. This again shows that the Kröner elastic moduli of the reflections are a very good approximation of the diffraction elastic constants. As the measurements are limited to the elastic regime and the elastic-plastic transition zone only a small load redistribution is seen, but it is correctly predicted by the self-consistent modelling scheme. Perpendicular to the tensile axis, the figures 5.8(c) and 5.8(d), the model predictions are almost as accurate. Taking the relative larger experimental scatter in this direction into account the predictions of the diffraction elastic constants in this direction is also accurately predicted by the model. In the transition zone some discrepancies are noted, especially for the 111-, 311- and 531-reflections.

The residual lattice strains have been measured in the copper sample at seven unloads, 0.2%, 0.5%, 1%, 2%, 3%, 4% and 5% plastic deformation, and the results are compared with model calculations in figure 5.9 for the reflections parallel and perpendicular to the tensile axis.

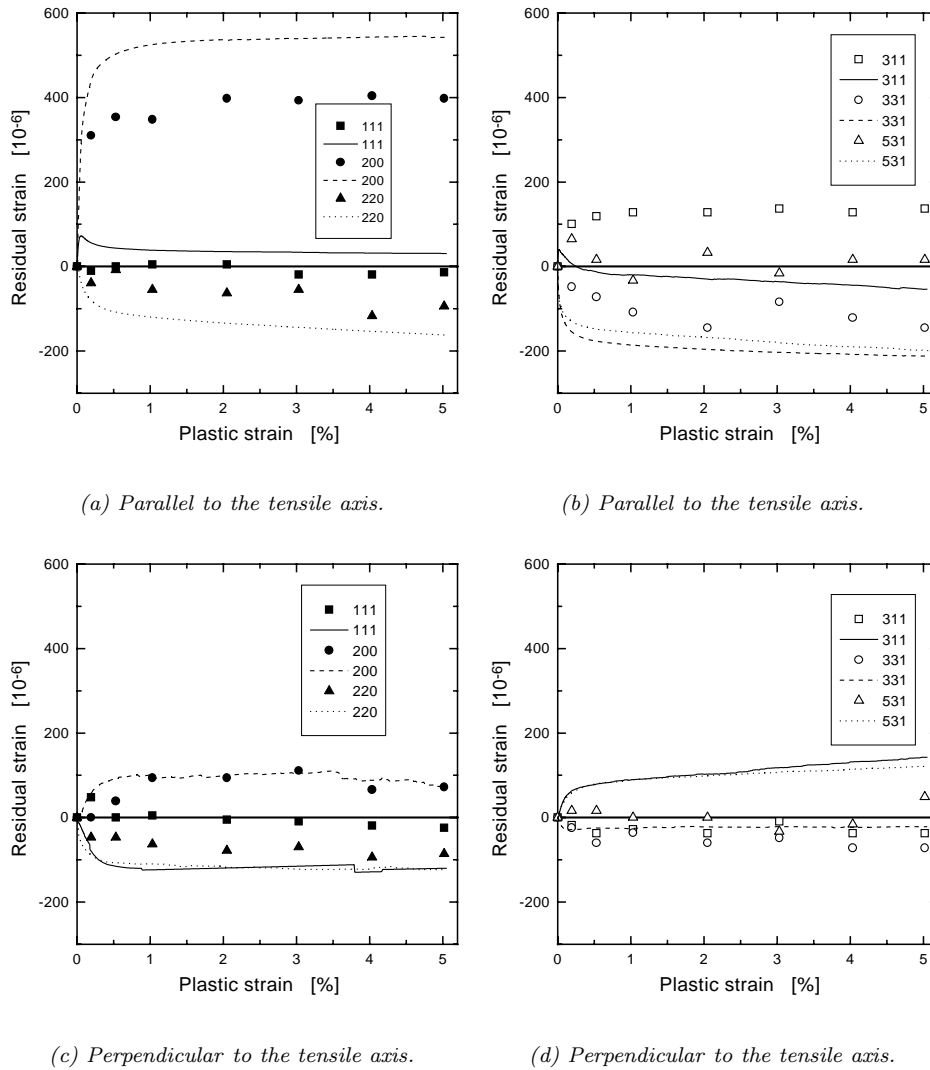


Figure 5.9. The residual lattice strain of the reflections as a function of the plastic strain for copper.

As seen in figure 5.9, the model predictions of the residual strains in copper are not as accurate as the predictions for stainless steel. Parallel to the tension

axis, only the 111-reflection is within $\pm 100 \times 10^{-6}$ of the measured data, and perpendicular to the tension axis the 111-, 311- and 531-reflections all deviate by $\sim 100 \times 10^{-6}$. It is interesting to note that the 200-reflection both parallel to and perpendicular to the tensile axis show good agreement with the measured *in-situ* data, but only in the direction perpendicular to the tensile axis the predictions of the residual strains are accurate.

Generally the *in-situ* model predictions for the copper sample are as accurate as for the stainless steel sample, but the residual strain measurements are not as accurate as for the stainless steel sample. This could be explained by the fact that the copper sample was not fully recrystallised before it was used for the measurements. Residual strain from the cold rolling may have influenced the measurements.

5.3 Summary

The comparison of the predictions of the Taylor and Sachs models with the neutron diffraction measurements show that these models are not suitable for this type of correlation. The lack of material parameters in the models are compensated by the use of the Kröner stiffnesses, but still the rigid plastic models cannot predict the elastic lattice strains with acceptable accuracy. However, these models have successfully been used to predict deformation textures for large strains, where the elastic deformation is negligible.

The neutron diffraction measurements are suitable for evaluation of the self-consistent modelling scheme. The degree of detail in the model is practically the same as observed in a neutron diffraction measurement. The stresses and strains are assumed constant within the grains and the predicted average elastic strain values for a specific grain sub-set is comparable to the measured average lattice strains for a corresponding set of grains. In the self-consistent scheme the grains are regarded as inclusions in a homogeneous continuum matrix and in the neutron diffraction measurements the average of many grains with different surroundings is measured at the same time, making the 'average surroundings' similar to the continuum matrix used in the model calculations.

6 Conclusion

In the following a summation of the previous discussions will be made, and the most important conclusions will be highlighted.

6.1 Modelling

In the present work, three polycrystal deformation models have been investigated (Taylor 1938, Sachs 1928 and Hutchinson 1970). The models have been implemented, and the results of calculations of all the models have successfully been correlated with results reported in the literature and with the results of neutron diffraction measurements.

6.1.1 Taylor and Sachs Models

These basic upper- and lower-bound models have been used as a reference of what is possible to estimate using the simplest assumptions for the polycrystal (*i.e.* uniform strain or stress). Both the models are rigid plastic and they do not include material properties such as elastic anisotropy. The calculated average m -factors are 3.06 and 2.23 for the Taylor model and the Sachs model, respectively, which is in agreement with reported values (Chin and Mammel 1967, Leffers 1995).

The calculated lattice rotations for both models leads to the well known $\langle 111 \rangle$ - $\langle 100 \rangle$ fiber texture for uniaxial deformation of *fcc* metals. The number of active slip systems in the grains are five in the Taylor model, to accommodate the five independent strain components, and one in the Sachs model (for symmetric orientations the present Sachs model is a multi slip model), making the rotation pattern for the two models, shown in figure 2.12(d) and 2.12(e), quite different.

Neither of the models is practical with respect to the correlation with neutron diffraction measurement of elastic lattice strains. For a possible comparison, the calculated stress components for the reflections must be converted to 'elastic' strains by the diffraction elastic constants (here the Kröner stiffness for the reflections) before comparison with the measured elastic lattice strains are possible. This conversion is inherently an estimate as only a single component of the strain tensor is used. The correlation with the neutron diffraction measurements show a rather poor agreement but the models have in many cases been successfully used to predict deformation textures for large strains. The texture development is an overall parameter that does not directly reflect the underlying micro-mechanics, and at large strains the influence of the elastic anisotropy is negligible.

6.1.2 Self-consistent Model

The numerical predictions imply that the dominating deformation mode in the present self-consistent polycrystal model is one, in which grains have three active slip systems. Approximately 50% of the grains accommodate the deformation by three active slip systems, while less than 10% of the grains utilise the general five active slip systems used in the Taylor model.

The hybrid material, with the elastic anisotropy of copper and the strength properties of aluminium, is included to pinpoint the effect of elastic anisotropy on polycrystal deformation as modelled by the present self-consistent model. As expected elastic anisotropy has a very significant effect at the earliest stage of the elastic-plastic transition, but already at 0.1% plastic strain the deformation pattern is practically identical in aluminium, copper and hybrid. The difference in yield point and work hardening between aluminium and copper has practically no effect on the deformation pattern either.

Thus, for tensile deformation of texture-free *fcc* materials with (practically) no difference between the hardening rates for different slip systems (as determined by the hardening law in equation 2.31) the model predicts one single deformation pattern, practically independent of the mechanical parameters of the materials. Of course this 'universal' deformation pattern will be translated into different mechanical responses via the different mechanical properties of different materials.

By introducing an initial non-random texture the predicted deformation pattern will change. The average number of slip systems and the average *m*-factor will change as the average is taken for a different population of grains. The deformation pattern for a specific grain with a given orientation will also change because it is now interacting with a different continuum matrix. Thus, the universal deformation pattern is only universal for initially texture-free materials. For materials with a significant initial texture new calculations should be made, starting with a population of grains representative of the actual initial texture, as shown in section 5.

It is obvious that a self-consistent model like the present model with plastic interaction with the continuum matrix is a better model than the Taylor and the Sachs models. There are no physical reasons why the individual grains should interact with a matrix which is stronger than the average grain. In the Taylor model, which is equivalent to an infinitely stiff matrix, the stress continuity is neglected and in the Kröner self-consistent model (Kröner 1961) the continuum matrix has the 'elastic stiffness' of the polycrystal even in the plastic regime. The Sachs model is equally unrealistic as it almost completely neglects intergranular strain continuity. The weakest point in the self-consistent scheme is the lack of direct grain-to-grain interaction. By using an *N*-site model (Molinari *et al.* 1987) the direct interaction between *N* grains with their different crystallographic orientations can be included. The limit of the degree of detail is the representation of a polycrystal with a finite element model (Dawson *et al.* 1994). However, for a 1-site model, it is difficult to imagine anything better than the self-consistent concept.

6.2 Implications for Diffraction Measurements

The present self-consistent polycrystal deformation model has been used to find the best suitable reflections for stress and strain measurements with neutron diffraction. Such a reflection must have linear relation between the applied stress and the elastic lattice strain.

The degree of plastic anisotropy follows the degree of elastic anisotropy for the reflections parallel to the tensile axis, but perpendicular to the tensile axis

the plastic anisotropy is of the same size in the three materials. The elastic strain variation (the relative standard deviation) within the reflections is relatively small in the elastic region in both directions in all the materials. In the plastic region the variation increases rapidly, especially in the direction perpendicular to the tensile axis, and the relative standard deviation of the elastic lattice strain are in most of the reflections about 50%. As discussed in section 5.2 the very large variations for the 200-reflection perpendicular to the tensile axis is caused by the selection of the active slip systems, which for some orientations within this reflection only allow deformation modes with unrealistic lateral contractions.

One explanation of this property in the model can be the imposed constraint on the grains. In the model, all grains are embedded in the same homogeneous matrix, and as such, the extreme lateral contractions observed for some grains will not encounter more resistance in the pseudo matrix as a more normal contraction mode. An additional indication of that this might be the reason, is the calculation with an initial non-random texture in section 5.2. In this case the properties of the pseudo matrix is no longer symmetric and the unrealistic behaviour of the 200-reflection perpendicular to the tensile axis is not observed.

The problem might be avoided by using a more specific interaction between the grains as in an N -site model (Molinari *et al.* 1987). In an N -site model the direct interaction between N grains is included in the calculations, and thereby the loads applied to a specific grain would not be as highly symmetric as in the 1-site model with random texture. The extent of the calculations increase rapidly with increasing N , and within the present work, this model approach is not utilised.

The 311-reflection shows the smallest linearity deviation both parallel and perpendicular to the tensile axis in all the materials (aluminium, copper and stainless steel), and it also shows the smallest residual strain build-up when loaded plastically. Thus, it is a suitable reflection to use for stress/strain characterisation.

The calculations show that the 111, 200 and 220 reflections are deviating from linearity with more than the normal strain resolution in a neutron diffraction measurement, and that the residual lattice strain build-up is also high in these reflections. This indicates that if these reflections are used in stress and strain measurements, the non-linearities must be taken into account and the intergranular residual stresses must be separated from those originating from the macroscopic plastic deformation.

When studying lattice strains in structural components the precise deformation history is seldom known and it may furthermore differ greatly from simple uniaxial tension as simulated in the present calculations. The present simulations indicate that the orientation dependency will result in some variation in measured elastic lattice strains even within regions of a structure which has experienced a nearly homogeneous plastic deformation. The best way to obtain qualified information of the intergranular strains in a sample that has been subjected to a given deformation history, is to make calculations similar to the ones in section 3, that simulates the given deformation history.

6.3 Model Evaluation

In the present work a well known self-consistent scheme for describing polycrystal deformation has been used to simulate uniaxial deformation of aluminium, copper and austenitic stainless steel. It is selectively chosen to calculate the evolution of elastic strains in various grain sub-sets as these numerical results are directly comparable to actual experimental observations when using neutron diffraction. As such, the aim has been to evaluate the model predictions at a grain size scale, rather than the usual evaluations based on texture developments. The elastic lat-

tice strain evolution has been followed by diffraction measurements while straining the samples to 2 – 5% total strain.

Aluminium The lattice strains for the 111-, 200- and 220-reflections were measured using the fixed wavelength technique on the TAS-8 spectrometer at the DR-3 reactor at Risø National Laboratory (Denmark). For each reflection, measurements on two identical samples were completed, and the results are presented as an average of these two.

Comparing the model predictions and the measurements, it was found that calculations based on a linear hardening law did not successfully predict the onset of yielding. All the experimental results show a gradual transition from elasticity to plasticity that is more accurately predicted by the numerical results based on an exponential hardening law.

The calculations with the exponential decreasing hardening law accurately predicts the elastic strain evolution in the 111- and 220-reflections. For the 200-reflection, however, great discrepancy is observed, and from 1 to 3% total strain the model under estimates the elastic strain level by approximately 20%.

It is clear that the model is lacking some micro-mechanical mechanism explaining this discrepancy in the elastic strains of the 200-reflection. This could be explained by different dislocation pile-up properties on the crystallographic planes which may point towards an inappropriate hardening law, as these properties are in fact set to be identical for all orientations in the calculations.

Stainless steel The complete diffraction pattern for 15 reflections were measured using the TOF technique on the NPD instrument at Manuel Lujan Neutron Scattering Center (USA).

The numerical prediction of the macroscopic stress-strain response using the exponential decreasing hardening law can be fitted very closely to the measured macroscopic stress-strain response of stainless steel. The comparison between the *in-situ* diffraction measurements and the model predictions show good agreement for the reflections parallel to the tensile axis, but perpendicular to the tensile axis discrepancies are noted for some of the reflections.

The calculations for the 200-reflection perpendicular to the tensile axis are predicting the measured data very accurately, in contradiction to the calculations with initially random texture discussed in section 6.3. As explained in section 5, the introduction of a non-random initial texture causes the overall stiffness tensor and thereby the continuum matrix in the Eshelby calculations not to be transverse isotropic. The changed symmetry will change the set of active slip systems, and thereby the unrealistic deformation modes might be avoided.

The predicted residual strains are fairly accurate for most of the reflections parallel to the tensile axis, but perpendicular to the tensile axis only the 200- and 220-reflections are predicted with acceptable accuracy and some of the other reflections are wrong in sign.

Copper The measurements on copper were, likewise made with the TOF technique on the NPD instrument at Manuel Lujan Neutron Scattering Center (USA).

The measured macroscopic stress-strain response of copper show a rather small transition zone and an almost linear hardening, and the hardening parameters, h_{ratio} and h_{exp} , used in the numerical calculations are relatively high. The comparison between the *in-situ* diffraction measurements in the elastic region and the model predictions show good agreement for all the reflections both parallel and perpendicular to the tensile axis.

The predicted residual strains for copper are not as accurate as for stainless steel. Only the residual strain for one or two of the reflections in each direction

are predicted with acceptable accuracy. This might be caused by the fact that the copper sample was not fully recrystallised after manufacture, and thereby residual strains from the cold rolling could have influenced the measurements.

6.4 General Conclusions

In the present work the self-consistent polycrystal deformation model of Hutchinson has been investigated. The predictions of the model have been evaluated on a grain size scale by comparison with elastic lattice strains measured in grain subsets by neutron diffraction. The correlation shows that the model predictions for the reflections parallel to the tensile axis in a uniaxial tension test are generally very accurate. Perpendicular to the tensile axis (and for a few reflection parallel to the tensile axis) some discrepancies are noted. One way to investigate the observed discrepancies would be to introduce specific hardening laws for particular orientations, although not without increasing the amount of empiric assumptions in the model. As a numerical exercise, the hypothesis of a range of hardening laws for various orientations may be tested, however, it is envisaged that the diffraction study may lead to a more qualified selection of hardening laws based on experimental observations.

In combination with the neutron diffraction measurements the model predictions of the relation between the lattice stains in specific grain sub-sets and the overall stress can facilitate the interpretation of technological applications of neutron diffraction, where the volume average stress state is of interest. The model calculations have pinpointed that the reflections used in the characterisation of volume average stresses must be chosen carefully. The nonlinear behaviour of some reflections would have a devastating effect on the calculated stresses. One way of selecting the most suitable reflection (the one with a linear response even above yield and a minimum build-up of residual strains) is shown in section 3. For a given texture and deformation history the stress-elastic strain responses of the reflections can be determined using the present model.

References

- Allen, A.J., Hutchings, M.T. and Windsor, C.G. (1985). Neutron diffraction methods for the study of residual stress fields. *Adv. in Phys.* **34**, 445.
- Arora, J.S. (1989). *Introduction to Optimum Design*, McGraw-Hill, New York.
- Asaro, R.J. (1983). Micromechanics of Crystals and Polycrystals, *Adv. Appl. Mech.* **23**, 1.
- Bassani, J.L. (1994). Plastic Flow of Crystals. *Adv. in Appl. Mech.* **30**, 191.
- Barrett, C.S. and Massalski, T.B. (1980). *Structure of Metals* Pergamon Press, Oxford.
- Berveiller, B. and Zaoui, A. (1979). An extension of the self-consistent scheme to plastically-flowing polycrystals. *J. Mech. Phys. Solids* **26**, 325.
- Bishop, J.F.W. (1953). A Theoretical Examination of the Plastic Deformation of Crystals by Glide. *Phil. Mag.* **44**, 51.
- Bishop, J.F.W. and Hill, R. (1951a). A Theory of the Plastic Distortion of a Polycrystalline Aggregate under Combined Stresses. *Phil. Mag.* **42**, 414.
- Bishop, J.F.W. and Hill, R. (1951b). A Theoretical Derivation of the Plastic Properties of a Polycrystalline Face-Centered Metal. *Phil. Mag.* **42**, 1298.
- Bunge, H.-J. (1982). *Texture Analysis in Materials Science*. Butterworths & Co.
- Bourke, M.A.M., Goldstone, J.A. and Holden, T.M. (1992). Residual Stress Measurement using the Pulsed Neutron Source at LANSCE. *Measurements of Residual and Applied Stress Using Neutron Diffraction, NATO ASI series*, M.T. Hutchings and A.D. Krawiz, eds. Kluwer Academic.
- Bourke, M.A.M., Goldstone, J.A., Shi, N., Allison, J.E., Stout, M.G. and Lawson, A.C. (1993). Measurement and prediction of strain in individual phases of a 2219AL/TiC/15P-T6 composite during loading. *Scripta Metallurgica et Materialia* **29**, 711.
- Budiansky, B. and Wu, T.T. (1962). Theoretical Prediction of Plastic Strains of Polycrystals. *Proc. 4th Congr. Appl. Mech.*, 1175.
- Chin, G.Y. and Mammel, W.L. (1967). Computer Solutions of the Taylor Analysis for Axisymmetric Flow. *Trans. of the Met. Soc. of AIME* **239** 1400-1405.
- Clausen, B. and Lorentzen, T. (1997a). A Self-consistent Model for Polycrystal Deformation, Description and Implementation. *Risø-R-970(EN)*, Risø National Laboratory, 4000 Roskilde, Denmark.
- Clausen, B. and Lorentzen, T. (1997b). Experimental Evaluation of a Polycrystal Deformation Modelling Scheme using Neutron Diffraction Measurements. Submitted to *Metall. Trans.* April 1997.
- Dawson, P.R., Beaudoin, A.J. and Mathur, K.K. (1994). Finite Element Modelling of Polycrystalline Solids. *Proceedings of the 15th Risø Int. Symp. on Mat. Sci.* (editors S.I. Andersen *et al.*), 33.
- Daymond, M.R., Bourke, M.A.M., Von Dreele, R., Clausen, B. and Lorentzen, T. (1997) Use of Rietveld Refinement for Elastic Macro Strain Determination and for Evaluation of Plastic Strain History from Diffraction Spectra. Submitted to *Jour. Appl. Phys.* March 1997.

- Dieter, G.E. (1988). *Mechanical Metallurgy*. McGraw-Hill.
- Eshelby, J.D. (1957). The Determination of the Elastic Field of an Ellipsoidal Inclusion, and Related Problems. *Proc. Roy. Soc. Lond.* **A241**, 376.
- Harren, S.V. (1991a). The Finite Deformation of Rate-dependent Polycrystals - I: A Self-consistent Framework. *J. Mech. Phys. Solids* **39**, 345.
- Harren, S.V. (1991b). The Finite Deformation of Rate-dependent Polycrystals - II: A Comparison of the self-consistent and Taylor Methods. *J. Mech. Phys. Solids* **39**, 361.
- Hill, R. (1965a). Continuum Micro-mechanics of Elastoplastic Polycrystals. *J. Mech. Phys. Solids* **13**, 89.
- Hill, R. (1965b). A Self-consistent Mechanics of Composite Materials. *J. Mech. Phys. Solids* **13**, 231.
- Hill, R. (1966). Generalized Constitutive Relations for Incremental Deformation of Metal Crystals by Multislip. *J. Mech. Phys. Solids* **14**, 95.
- Hull, D. and Bacon, D.J. (1984). *Introductions to Dislocations*. Pergamon Press, Oxford.
- Hosford, W.F. (1964). Microstructural Changes During Deformation of [011] Fiber-Textured Metals. *Trans. Met. Soc. AIME* **230**, 12.
- Hosford, W.F. (1977). On Orientation changes Accompanying Slip and Twinning. *Texture of crystalline solids* **2**, 175.
- Hutchinson, J. W. (1970). Elastic-plastic Behaviour of Polycrystalline metals and Composites. *Proc. Roy. Soc. Lond.* **A319**, 247.
- Juul Jensen, D. and Leffers, T. (1989). Fast Texture Measurements Using a Position Sensitive Detector. *Textures and Microstructures* **10** 361.
- Kneer, G. (1965). Über die Berechnung der Elastizitätsmoduln vielkristalliner Aggregate mit Textur. *Phys. Stat. Sol.* **9**, 825.
- Kröner, E. (1958). Berechnung der Elastischen Konstanten des Vielkristalls aus den Konstanten des Einkristalls. *Z. für Physik* **151**, 504.
- Kröner, E. (1961). Zur Plastischen Verformung des Vielkristalls. *Acta metall.* **9**, 155.
- Ledbetter, H.M. (1984). Monocrystal-Polycrystal Elastic Constants of a Stainless Steel. *Phys. Stat. Sol. A* **85**, 89.
- Leffers, T. (1988). Panelist's Contribution. ICOTOM 8, The Metallurgical Society, 273-284.
- Leffers, T. (1995). Long-Range Stresses Associated with Boundaries in Deformed Materials. *Phys. Stat. Sol.* **149**, 69.
- Leffers, T., Asaro, R.J., Driver, J.H., Kocks, U.F., Mecking, H., Tomé, C. and Van Houtte, P. (1988). Panel Report. ICOTOM 8, The Metallurgical Society, 265-272.
- Leffers, T and Juul Jensen, D. (1986). *Textures and Microstructures* **6**, 231.
- Leffers, T and Lebensohn, R.A. (1996). *Proceedings ICOTOM 11* Eds. Z. Liang *et al.*. International Academic Publishers, Beijing. 307.

- Leffers, T. and Pedersen, O.B. (1985). Computer Simulation of the Elastic-Plastic Transition in a Taylor Polycrystal. ISCMA 7, eds. H.J. McQueen et al. Pergamon Press, Oxford 275-280.
- Lorentzen, T. (1990). *Bulk Residual Stress Studies by Neutron Diffraction*. Thesis, Institute of Mechanical Engineering, Aalborg University, 9000 Aalborg, Denmark.
- Lorentzen, T. and Sørensen, N.J. (1991). A New Device for *In-situ* Loading of Samples During Neutron Diffraction Strain Measurements. *Proceedings of the 12th. Risø International Symposium on Materials Science*, Risø National Laboratory, 4000 Roskilde, Denmark.
- Lorentzen, T., Fauerholdt, T., Clausen, B. and Danckert, J. (1996). Characterisation of Residual Stresses Generated During Inhomogeneous Plastic Deformation. Submitted to *Mat. Sci. & Eng.* March 1996, under revision.
- Macherauch, E. and Kloos, K.H. (1986). Origin, Measurement and evaluation of Residual Stresses. *Residual Stresses in Science and Technology* **1**, 3.
- Molinari, A., Canova, G.R. and Ahzi, S. (1987). A Self Consistent Approach of the Large Deformation Polycrystal Viscoplasticity. *Acta Metall.* **35**, 2983.
- Noyan, I.C. and Cohen, J.B. (1987). *Residual Stress – Measurement by Diffraction and Interpretation*. Springer-Verlag, New York.
- Pedersen, P. (1995). Simple transformations by proper contracted forms: Can we change the usual practice? *Numerical Methods in Engineering* **11**, 821.
- Press, W.H., Teukolsky, S.A., Vetterling, W.T. and Flannery, B.P. (1992). *Numerical Recipes in C*, Cambridge University Press 430-444.
- Reuss, A. (1929). Berechnung der Fließgrenze von Mischkristallen auf Grund der Plasticitätsbedingung für Einkristalle. *Z. angew. Math. Mech.* **9**, 49.
- Sachs, G. (1928). Zur Ableitung einer Fließbedingung. *Z. Ver. Deu. Ing.* **72-22**, 734.
- Taylor, G.I. (1938). Plastic Strain in Metals. *J. Inst. Metals* **62** 307.
- Voigt, W. (1928). *Lehrbuch der Krystalphysik* Teubner, Berlin.
- Von Dreele, R.B. (1997). Quantitative Texture Analysis by Rietveld Refinement. Submitted to *Jour. Appl. Cryst.*
- Von Mises, R. (1928). Mechanik der plastischen Formänderung von Kristallen. *Z. Angew. Math. Mech.* **8** 161.
- Zienkiewicz, O.C. and Taylor, R.L. (1988). *The Finite Element Method*. McGraw-Hill, London.

Appendix A

Appropriate Gauge Volume

The following is an investigation of the influence of the gauge volume on the reproducibility and sample-to-sample variations of a typically fixed wavelength neutron diffraction measurement. The grain size in the sample must also be considered as it determines the grain number within a specific gauge volume. The reproducibility of a measurement is simulated by measuring the lattice spacing five consecutive times without changing the set-up. The sample-to-sample variation is simulated by measuring the elastic lattice spacing at five different locations in the sample. The samples are commercially pure aluminium (Al-2S, 99.5%) with two different grain sizes, $80\mu\text{m}$ and $400\mu\text{m}$.

The theoretical number of diffracting grains in a specified gauge volume is depending on the grain size, the multiplicity of the given reflection and the resolution of the spectrometer. The multiplicity of all possible reflections are shown in table A.1.

hkl	a00	aaa	aa0	ab0	abb	abc
Multiplicity	6	8	12	24	24	48

Table A.1. Possible reflections and their multiplicity.

Assuming random texture in the samples, the grain number that actually participates in the measurements can be estimated as the total grain number in the gauge volume multiplied by the multiplicity of the reflection and divided by the fraction of orientation space the detector covers. For the present neutron diffraction set-up using the $\langle 111 \rangle$ reflection, this means that only approximately 1 out of 4700 grains in the gauge volume participates in the measurements, see section A.1.

The gauge volume, V , is determined by the slit width of the incident beam, w_I , the slit width of the diffracted beam, w_D , the slit height, h , and by the diffraction angle 2θ , see figure A.1

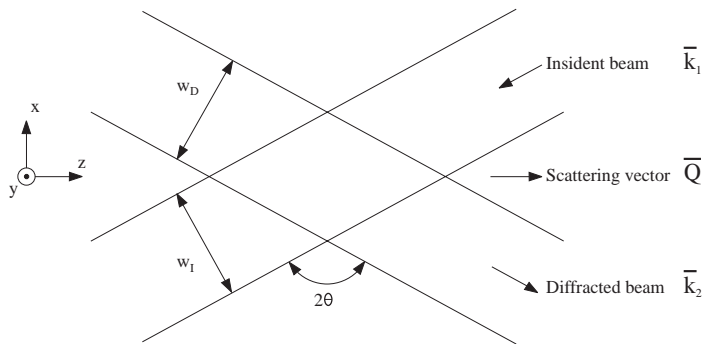


Figure A.1. Horizontal section of the gauge volume.

From figure A.1 the gauge volume can be determined as

$$V = \frac{w_I w_D h}{2 \sin \theta \cos \theta} = \frac{w_I w_D h}{\sin 2\theta} \quad (\text{A.1})$$

and it is seen that the gauge volume is proportional to the two slit widths and the slit height, and inverse proportional to the sine of the scattering angle (2θ).

In the present measurements we are using the 111-reflection in the aluminium samples and a wavelength of 3.307\AA making the scattering angle (2θ) approximately 90° . This means that the denominator in equation A.1 is approximately 1 and the expression reduces to $V = w_I w_D h$.

To obtain the highest possible intensity in the incident beam a pyrolytic graphite (PG) monochromator is used. The advantage of using a PG monochromator is that it can be focused perpendicular to the scattering plane but it has a relative high lattice spacing in the used $\langle 200 \rangle$ reflection compared to the aluminium $\langle 111 \rangle$ reflection. This makes the monochromator diffraction angle relatively small ($20 - 30^\circ$) for the used wavelength of 3.307\AA which has a negative influence on the set-up resolution. The spectrometer is aligned and optimized for the selected wavelength.

80 μm grain size

The diffraction angle has been determined in an aluminium sample with a grain size of $80\mu\text{m}$ for four different gauge volume sizes. The following four combinations of the available fixed slits were used; 5×10 and 5×10 defining a gauge volume of $5 \times 5 \times 10 = 250\text{mm}^3$, 5×5 and 5×5 defining a gauge volume of $5 \times 5 \times 5 = 125\text{mm}^3$, 5×2 and 5×2 defining a gauge volume of $5 \times 5 \times 2 = 50\text{mm}^3$, and 2×10 and 1×10 defining a gauge volume of $2 \times 1 \times 10 = 20\text{mm}^3$. Using the grain size, the gauge volume and the percentage of grains participating in the diffraction measurement described earlier, the corresponding theoretical number of grains that participates in the measurements are approximately; 200, 100, 40 and 15, respectively.

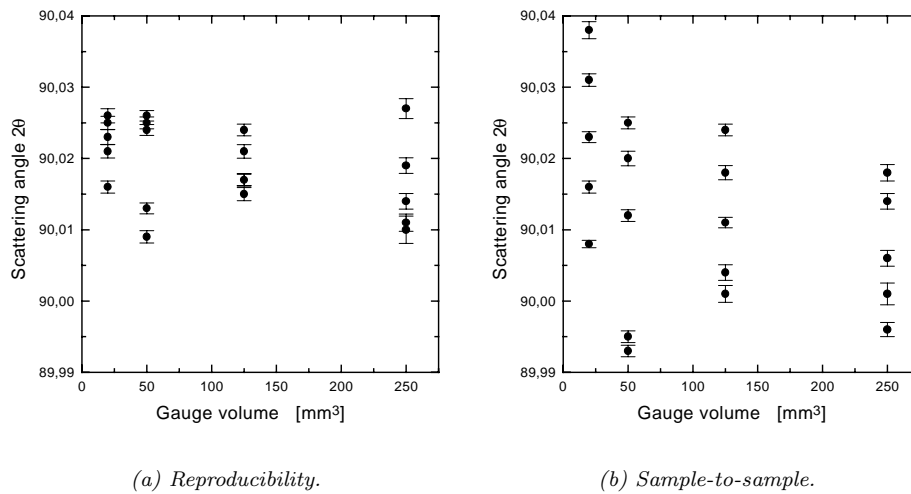


Figure A.2. The measured scattering angle for the eight sets of measurements in the aluminium with $80\mu\text{m}$ grain size.

The results of the eight sets of measurements are shown in figure A.2. The average diffraction angle and the standard deviation for all the gauge volume sizes are shown in table A.2. The standard deviations for the sample-to-sample measurements are almost as low as the reproducibility measurements indicating that the used gauge volume size is adequate for neutron diffraction measurements in materials with $80\mu\text{m}$ grain size.

400 μm grain size

In the investigations of the aluminium with a grain size of $400\mu\text{m}$ the following two combinations of the available fixed slits are used; 20×5 and 20×5 defining a

Gauge volume mm^3	Reproducibility		Sample-to-sample	
	Average 2θ	Standard deviation	Average 2θ	Standard deviation
20	90.024	0.002	90.023	0.012
50	90.019	0.008	90.009	0.014
100	90.019	0.004	90.012	0.010
250	90.016	0.007	90.007	0.009

Table A.2. Test results from the sample with $80\mu m$ grain size.

gauge volume of $20 \times 20 \times 5 = 2000mm^3$, and 20×2 and 20×2 defining a gauge volume of $20 \times 20 \times 2 = 800mm^3$. This means that the corresponding theoretical number of grains that participates in the measurements are approximately 13 and 5, which is lower than all the in all the measurements on the sample with $80\mu m$ grain size.

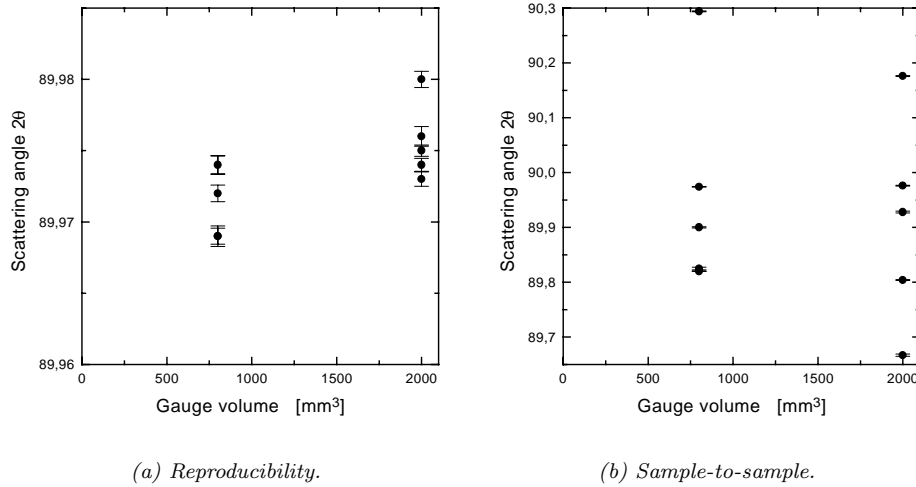


Figure A.3. The measured scattering angle for the two sets of measurements in the aluminium with $400\mu m$ grain size. Note the scale difference.

Gauge volume mm^3	Reproducibility		Sample-to-sample	
	Average 2θ	Standard deviation	Average 2θ	Standard deviation
800	89.976	0.003	89.910	0.191
2000	89.972	0.003	89.963	0.196

Table A.3. Test results from the sample with $400\mu m$ grain size.

The results of the two sets of measurements are shown in figure A.3. The standard deviation of the scattering angle is very small for the five consecutive measurements at the same location with both the gauge volume sizes. The average diffraction angle and the standard deviation for the two gauge volume sizes are shown in table A.3. The very large differences in the scattering angle in the measurements at different locations are caused by the large grain size and the low number of grains within the gauge volume. As the number of grains in the gauge volume decreases the measured diffraction angle are an average of fewer and fewer

grains, and changing the position even a very small amount change the position of the diffracting grains within the gauge volume and thereby change the measured diffraction intensities. In addition to the fewer grains, the relative large gauge volume size introduces other effects, such as different path lengths and thereby different absorption. In opposition to the measurements on the material with $80\mu\text{m}$ grain size, the present measurements show that the sample-to-sample variation is unacceptably large for the larger grain sizes ($400\mu\text{m}$).

These measurements indicates that the grain size must be about $100\mu\text{m}$ to obtain an acceptable accuracy using the neutron diffraction technique.

Strain Variations

The described measurements indicates that the reproducibility of a 2θ measurement is very good and almost independent of the grain size, but the sample-to-sample variations depend strongly on the grain size.

The highest value of the standard deviation of 2θ in the measurements of the reproducibility for both grain sizes is 0.008° . Including the sample-to-sample scatter measurements the highest standard deviation for the $80\mu\text{m}$ grain size is 0.014° . The neutron diffraction measurements in the present work are all with scattering angles that are very close to 90° and using equation A.8, described in appendix A.2, the maximum relative standard deviation in the elastic lattice strain measurements are approximately 0.01. The highest level of measured lattice strain in the present work is about 3000×10^{-6} (200-reflection in stainless steel) rendering a maximum standard deviation of a strain measurement of 30×10^{-6} .

A.1

Diffracting Grains Within the Gauge Volume

In a neutron diffraction measurement the fraction of grains that participates in a measurement is determined by the grain size, the gauge volume and the fraction of the entire orientation space that the detector covers. The following calculations determine the latter parameter for the used single detector set-up at the TAS-8 spectrometer at the DR3 reactor at Risø National Laboratory.

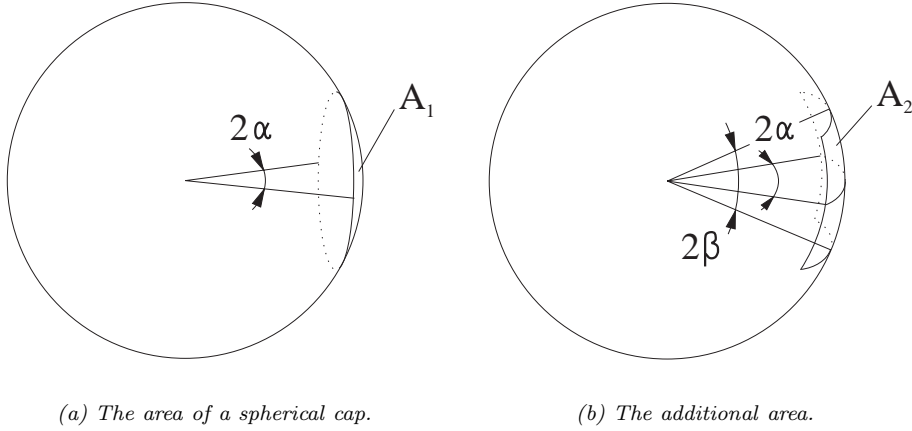


Figure A.4. The area covered by the detector.

If the detector was circular the covered area would be a spherical cap as seen in figure A.4(a). But the detector is a line detector and the additional area covered by the detector is shown in figure A.4(b). The lateral span of the detector, 2α , is approximately 1° and the vertical span, 2β , of the detector is approximately 8° . The total area of the sphere is $4\pi r^2$ and the fraction of the orientation space that is covered by the detector is found as

$$F_{det} = \frac{A_1 + A_2}{A_{tot}} = \frac{2\pi r^2 (1 - \cos \alpha) + 4\pi r^2 \cos(90 - \alpha) \frac{2\beta}{360}}{4\pi r^2} \approx \frac{1}{4700} \quad (\text{A.2})$$

A.2

Standard Deviation of a Strain Measurement

In a fixed wavelength neutron diffraction measurements the scattering angle is determined by measuring the diffracted intensity as a function of the angle and the elastic lattice strain can be determined from the measured scattering angle as described in section 4.1.1

$$\varepsilon_{hkl} = \frac{d - d_0}{d_0} = \frac{\sin \theta_0}{\sin \theta} - 1 \quad (\text{A.3})$$

The relative standard deviation of the strain can then be determined as

$$\frac{\sigma(\varepsilon)}{\varepsilon} = \sqrt{\left(\frac{\sigma(\sin \theta_0)}{\sin \theta_0}\right)^2 + \left(\frac{\sigma(\sin \theta)}{\sin \theta}\right)^2} \quad (\text{A.4})$$

The standard deviation of the sine to an angle can be expressed in terms of the standard deviation of the angle as

$$\sigma(\sin \theta) = \sin(\theta + \sigma(\theta)) - \sin \theta = \sin \theta \cos(\sigma(\theta)) + \cos \theta \sin(\sigma(\theta)) - \sin \theta \quad (\text{A.5})$$

Since $\sigma(\theta)$ is small $\cos(\sigma(\theta)) \approx 1$ and $\sin(\sigma(\theta)) \approx \sigma(\theta)$ and thereby

$$\sigma(\sin \theta) \approx \cos \theta \sigma(\theta) \quad (\text{A.6})$$

Then the relative standard deviation of the strain becomes

$$\frac{\sigma(\varepsilon)}{\varepsilon} = \sqrt{\left(\frac{\sigma(\theta_0)}{\tan \theta_0}\right)^2 + \left(\frac{\sigma(\theta)}{\tan \theta}\right)^2} \quad (\text{A.7})$$

As the difference between θ_0 and θ is generally very small in a neutron diffraction strain measurement $\tan \theta_0$ and $\tan \theta$ are assumed to be the same, and the standard deviation for θ_0 and θ are assumed to be the same. Then the relative standard deviation of the strain is found as

$$\frac{\sigma(\varepsilon)}{\varepsilon} = \frac{\sqrt{2} \sigma(\theta)}{\tan \theta} \quad (\text{A.8})$$

Appendix B

Calculated Residual Strains

The residual strains for the reflections parallel to the tensile axis calculated at the eight unloads described in section 3.2.6 for the six reflections in the three materials are shown in the tables B.1 to B.3.

ε_{11}^P	111	200	220	311	331	531
0.25%	98.3	-37.4	17.2	-23.7	10.6	-17.9
0.50%	106.1	-46.1	24.5	-27.5	14.5	-20.4
0.75%	111.8	-50.8	28.4	-29.6	16.2	-22.2
1.0%	116.1	-54.2	31.6	-31.3	17.2	-23.8
2.0%	128.8	-64.3	41.4	-35.6	20.5	-28.2
3.0%	140.1	-71.3	48.4	-38.6	22.6	-33.1
4.0%	152.0	-77.1	53.4	-41.4	24.3	-37.3
5.0%	163.2	-83.0	57.5	-43.7	25.7	-42.1

Table B.1. Calculated residual strains in aluminium ($\times 10^{-6}$).

ε_{11}^P	111	200	220	311	331	531
0.25%	15.9	165.1	-61.9	-3.8	-77.9	-62.9
0.50%	13.3	195.3	-71.4	-4.1	-88.9	-70.7
0.75%	12.2	208.5	-74.9	-4.3	-94.0	-74.3
1.0%	12.7	217.1	-77.9	-4.7	-97.6	-77.1
2.0%	17.2	246.7	-90.5	-5.5	-109.7	-86.5
3.0%	21.9	276.6	-102.7	-5.7	-121.3	-95.4
4.0%	26.5	306.5	-114.1	-5.6	-132.8	-104.0
5.0%	31.0	336.9	-125.4	-5.4	-144.3	-112.6

Table B.2. Calculated residual strains in copper ($\times 10^{-6}$).

ε_{11}^P	111	200	220	311	331	531
0.25%	28.2	386.9	-102.0	15.9	-159.5	-127.3
0.50%	16.7	541.9	-165.4	23.4	-224.0	-168.6
0.75%	2.1	613.1	-186.8	26.1	-243.9	-180.9
1.0%	-4.8	642.9	-196.4	25.8	-253.4	-187.7
2.0%	-6.8	671.8	-224.3	16.9	-271.1	-209.1
3.0%	-3.5	696.3	-248.2	12.4	-281.4	-226.4
4.0%	0.6	720.4	-269.9	10.1	-290.0	-243.3
5.0%	5.0	745.3	-288.9	9.0	-298.1	-260.2

Table B.3. Calculated residual strains in stainless steel ($\times 10^{-6}$).

Title and author(s)Characterisation of Polycrystal Deformation
by Numerical Modelling and Neutron Diffraction Measurements

Bjørn Clausen

ISBN ISSN
87-550-2304-5 0106-2840

Dept. or group Date
Materials Research Department September 1997

Groups own reg. number(s) Project/contract No.

Pages Tables Illustrations References
85 14 41 55

Abstract (Max. 2000 char.)

The deformation of polycrystals are modelled using three micromechanic models; the Taylor model, the Sachs model and Hutchinson's self-consistent (SC) model. The predictions of the rigid plastic Taylor and Sachs models are compared with the predictions of the SC model. As expected, the results of the SC model is about half-way between the upper- and lower-bound models. The influence of the elastic anisotropy is investigated by comparing the SC predictions for aluminium, copper and a hypothetical material (Hybrid) with the elastic anisotropy of copper and the Young's modulus and hardening behaviour of aluminium. It is concluded that the effect of the elastic anisotropy is limited to the very early stages of plasticity, as the deformation pattern is almost identical for the three materials at higher strains. The predictions of the three models are evaluated by neutron diffraction measurements of elastic lattice strains in grain sub-sets within the polycrystal. The two rigid plastic models do not include any material parameters and therefore the predictions of the SC model is more accurate and more detailed than the predictions of the Taylor and Sachs models. The SC model is used to determine the most suitable reflection for technological applications of neutron diffraction, where focus is on the volume average stress state in engineering components. To be able to successfully to convert the measured elastic lattice strains for a specific reflection into overall volume average stresses, there must be a linear relation between the lattice strain of the reflection and the overall stress. According to the model predictions the 311-reflection is the most suitable reflection as it shows the smallest deviations from linearity and thereby also the smallest build-up of residual strains. The model predictions have pin pointed that the selection of the reflection is crucial for the validity of stresses calculated from the measured elastic lattice strains.

Descriptors INIS/EDBALUMINIUM; AUSTENITIC STEELS; COPPER; CRYSTAL MODELS;
DEFORMATION; ELASTICITY; NEUTRON DIFFRACTION; PLASTICITY;
POLYCRYSTALS; STAINLESS STEELS; STRAINS; STRESSES

Available on request from:Information Service Department, Risø National Laboratory
(Afdelingen for Informationsservice, Forskningscenter Risø)
P.O. Box 49, DK-4000 Roskilde, Denmark
Phone (+45) 46 77 46 77, ext. 4004/4005 · Fax (+45) 46 77 40 13